ABSTRACT

Name: Mikhail Arov Department: Physics

Title: Measurement of $\sigma(p\bar{p} \to t\bar{t})$ in the $\tau + jets$ channel by the DØ experiment at Run II of the Tevatron Collider

Major: Physics Degree: Doctor of Philosophy

Approved by: Date:

Dissertation Director

NORTHERN ILLINOIS UNIVERSITY

ABSTRACT

The top quark is the heaviest and most mysterious of the known elementary particles. Therefore, careful study of its production rate and other properties is of utmost importance for modern particle physics. The Tevatron is the only facility currently capable of studying top quark properties by on-shell production. Measurement of the top quark pair production cross section is one of the major goals of the Tevatron Run II physics program. It provides an excellent test of QCD at energies exceeding 100 GeV. We report on a new measurement of $p\bar{p} \to t\bar{t}$ production at $\sqrt{s} = 1.96$ TeV using 350 pb^{-1} of data collected with the DØ detector between 2002 and 2005. We focus on the final state where a W boson from one of the top quarks decays into a τ lepton and its associated neutrino, while the other decays into a quark-antiquark pair. We aim to select those events in which the τ lepton subsequently decays to one or three charged hadrons, zero or more neutral hadrons and a tau neutrino (the charge conjugate processes are implied in all of the above). The observable signature thus consists of a narrow calorimeter shower with associated track(s) characteristic of a hadronic tau decay, four or more jets, of which two are initiated by b quarks accompanying the W's in the top quark decays, and a large net missing momentum in the transverse plane due to the energetic neutrino-antineutrino pair that leave no trace in the detector media. The preliminary result for the measured cross section is:

$$\sigma(t\bar{t}) = 5.1\ ^{+4.3}_{-3.5}\ \text{(stat)}\ ^{+0.7}_{-0.7}\ \text{(syst)}\ \pm 0.3\ \text{(lumi.)}\ \text{pb}$$

NORTHERN ILLINOIS UNIVERSITY

MEASUREMENT OF $\sigma(p\bar{p} \to t\bar{t})$ IN THE $\tau + jets$ CHANNEL BY THE DØ EXPERIMENT AT RUN II OF THE TEVATRON COLLIDER

A DISSERTATION SUBMITTED TO THE GRADUATE SCHOOL
IN PARTIAL FULFILLMENT OF THE REQUIREMENTS
FOR THE DEGREE
DOCTOR OF PHILOSOPHY

DEPARTMENT OF PHYSICS

BY
MIKHAIL AROV

DEKALB ILLINOIS
JULY 2008

Certification: In accordance with departmental and Graduate School policies, this dissertation is accepted in partial fulfillment of degree requirements

Dissertation Director

Date

DEDICATION

To my mother

ACKNOWLEDGEMENTS

I want to express my gratitude to the NIU physicists who shared my success and failure alike during my study and work at DØ . In particular, Professor Dave Hedin was always available and immensely helpful both as graduate program advisor and a very active member of my dissertation committee.

A very special thank you goes to Dr Dmitri Denisov. Despite the mountain of responsibilities as DØ spokesperson he still always found time to direct and help me.

I thank all members of DØ and the Tevatron staff; they made this work possible. I am especially grateful to members and convenors of the DØ Top group for their friendly and useful comments and suggestions.

I thank my colleagues and friends Andriy Zatserklyaniy, Sergey Uzunyan, Peter Svoisky, Peter Renkel, and many others. You've made my stay at Fermilab not only productive but fun as well.

Last but by no means least I would like to thank my advisor, Dhiman Chakraborty. Your patience and wisdom guided me through these years.

I would like to acknowledge the financial support of the National Science Foundation.

TABLE OF CONTENTS

LIST OF TABLES

LIST OF FIGURES

CHAPTER 1
INTRODUCTION

1.1 The Standard Model of Particle Physics

The ultimate goal of the field of elementary particle physics is to provide a single (and hopefully simple and elegant) set of laws and dependences that would accurately describe all the wealth of observable phenomena in the subatomic world. While this goal might never be fully attained, the so-called Standard Model (SM) [1] of particle physics represents a giant step in the right direction.

In this model there are two types of particles: leptons and quarks. These particles are classified in 3 "generations." Leptons and quarks of the second and third generation have properties very similar to those of the first generation, but are much more massive. Therefore they normally promptly (within 10^{-8} seconds) decay to the light particles of the first generation. For that reason only the matter composed of electrons and up and down quarks (the first generation elementary particles) exists under normal circumstances. However, from the point of view of the Standard Model, all three generations are equally important. The SM view of nature is summarized in Table 1.1, which also shows the masses and electric charges of quarks and leptons as well as the fundamental forces that govern interactions between them.

The main defining feature of the Standard Model is that these forces are all described by Lagrangian density functions, which are invariant under local gauge symmetries. For this reason such theories are called gauge field theories. In fact, the requirement of gauge invariance alone largely constrains the possible dynamic terms in the Lagrangian. There-

fore a gauge field theory can be specified by the Lie group that its invariance symmetry transformations form. For the SM, the defining group is $SU(3)_c \otimes SU(2)_L \otimes U(1)_Y$ where $SU(3)_c$ is the strong color group, $SU(2)_L$ corresponds to rotations in the weak isospin space, and $U(1)_Y$ to phase transformations.

Table 1.1: The known quarks and leptons.

Quarks				Leptons			
Charge 2/3		Charge $-1/3$		Charge -1		Charge 0	
	Mass, GeV		Mass, GeV		Mass, GeV		Mass
u	0.001–0.005	d	0.003–0.009	e	0.000511	ν_e	< 3 eV
c	1.15–1.35	s	0.075–0.175	μ	0.106	ν_μ	< 190 keV
t	172.5 ± 2.7	b	4.0–4.4	τ	1.777	ν_τ	< 18.2 MeV

These two subgroups correspond to two parts of the Standard Model: Quantum Chromodynamics (QCD) and Electroweak Theory. Because of this the Lagrangian of the SM has to contain two parts, for QCD and one for electroweak theory: $\mathcal{L}_{SM} = \mathcal{L}_{QCD} + \mathcal{L}_{electroweak}$

QCD is the theory of the strong nuclear force, which is transmitted by eight kinds of gauge bosons, named gluons G^a_μ, $a = 1, .., 8$. They mediate interactions between any particles that carry a net charge comprised of the three strong colors, including the gluons themselves. Surprisingly, the Lagrangian of such a complex theory can be written very concisely [2]:

$$\mathcal{L}_{strong} = \sum_j i\bar{q}_j \gamma^\mu D_\mu q_j - \frac{1}{2}\mathbf{tr} G_{\mu\nu} G^{\mu\nu} \tag{1.1}$$

where q_j are the quark fields, where j runs over all flavors, $D_\mu = \partial_\mu - ig_s G_\mu$. $G_{\mu\nu} = \partial_\mu G_\nu - \partial_\nu G_\mu - ig[G_\mu, G_\nu]$ and $G_\mu = \sum_{a=1}^{8} G^a_\mu \lambda^a/2$, where λ^a are the Gell-Mann matrices that satisfy the relations $[\lambda^a/2, \lambda^b/2] = if^{abc}\lambda^c/2$ and $\mathbf{tr}(\lambda^a\lambda^b) = 2\delta^{ab}$, and G^a_μ are the gluon field operators.

The Electroweak Model part can be written just as easily:

$$\mathcal{L}_{Electroweak} = \sum_k i\bar{\psi}_k \gamma_\mu D^\mu \psi_k - \frac{1}{4} F^{j\mu\nu} F^j_{\mu\nu} - \frac{1}{4} B^{\mu\nu} B_{\mu\nu}, \tag{1.2}$$

where $D_\mu = \partial_\mu - ig\vec{\sigma}/2\vec{A} - ig'\frac{Y}{2}B_\mu$, $F^j_{\mu\nu} = \partial_\mu A^j_\nu - \partial_\nu A^j_\mu + g\epsilon^{jkl}A^k_\mu A^l_\nu$, $j = 1, 2, 3$, and $B_{\mu\nu} = \partial_\mu B_\nu - \partial_\nu B_\mu$. A and B are the gauge fields, ψ_k - the interacting fermions, Y is the multiplet hypercharge given by $Y = 2(Q - T_3)$, where T_3 is the third isospin component and everything looks simple enough.

There are, however, two very important, even defining, features of the Electroweak theory that are not reflected in equation 1.2. The first one is an experimental observation that the weak nuclear force couples differently with fermions of different polarizations. Left-handed fermions form doublets of leptons:

$$\begin{pmatrix} \nu_e \\ e_L \end{pmatrix} \begin{pmatrix} \nu_\mu \\ \mu_L \end{pmatrix} \begin{pmatrix} \nu_\tau \\ \tau_L \end{pmatrix}$$

and quarks

$$\begin{pmatrix} u_L \\ d_L \end{pmatrix} \begin{pmatrix} c_L \\ s_L \end{pmatrix} \begin{pmatrix} t_L \\ b_L \end{pmatrix}$$

The $SU(2)_L$ group transforms the components of doublets into each other. Right-handed fermions

$$e_R, \mu_R, \tau_R, u_R, c_R, t_R, d_R, s_R, b_R$$

are singlets and are invariant under $SU(2)_L$ transformations.

The other (and most significant!) element of electroweak symmetry is that it is spontaneously broken.

1.2 Spontaneous symmetry breaking

While both electromagnetic and strong nuclear forces have been described by gauge field models with astounding success and unparalleled agreement with experimental findings, similar treatment of the the weak nuclear force runs into apparently serious difficulties. It turns out that any inertial mass terms in the Lagrangian explicitly beak the gauge invariance. This means that any gauge field must be massless and therefore long range. But it was very well established that the weak nuclear force has to be extremely short ranged, since no long-range parity-violating interactions were ever observed.

An ingenious idea of the authors of the modern theory of weak interaction turned this problem into an amazing success. $SU(2)_L \otimes U(1)_Y$ is not an exact explicit symmetry like $SU(3)_c$, neither is it an approximate symmetry like isospin. Instead it is a spontaneously broken theory. This means that at extremely high energies (over 100 GeV) the electroweak symmetry is explicit and exact, while under ordinary conditions it is broken by mass terms. Such a mechanism of breaking a symmetry and generating mass is named the Higgs mechanism. The scalar field involved in this mechanism is the Higgs boson. Search for this particle is one of the primary goals of the Tevatron's Run II physics program.

1.3 Hierarchy problem

Yet, with all its resounding success and mathematical elegance, the Standard Model cannot be the complete description of fundamental physics. First of all it does not describe gravity, the weakest, yet perhaps the most important of the fundamental forces. In addition there is a mathematical paradox within the SM - the hierarchy problem. Just like the gauge mass problem, which led to the discovery of vector bosons and establishment of modern particle physics, we hope that hierarchy problem is an important hint of physics beyond SM [3]. The difficulty arises from the fact that the Higgs boson (and in fact any

non-gauge renormalizable scalar field) has quadratically divergent loop corrections. That is, if the Higgs potential has the form

$$V = \lambda \left(\phi\phi^* - \frac{v^2}{2} \right) \tag{1.3}$$

then the 1-loop correction to the Higgs mass (which is $\sqrt{2\lambda v^2}$) due to the Higgs-Higgs coupling vertex is the quadratically divergent integral:

$$\sigma(\lambda v^2) = \frac{9\lambda^2}{2} \int \frac{d^4 l}{(2\pi)^4} \frac{1}{l^2 + \lambda v^2} \tag{1.4}$$

Now, the renormalized mass looks like this:

$$(m_H)^2 = (m_{H,bare})^2 + \frac{C\lambda}{\pi^2}\Lambda^2 \tag{1.5}$$

where Λ is the renormalization cut-off scale. The trouble is that Λ can be of the order of 10^{19} GeV (Planck scale). Since gravity has to be incorporated into the picture of the microworld, such large scales are naturally necessary and the Λ^2 factor makes an absurdly large Higgs mass. One solution to the hierarchy problem would be to eliminate all scalar fields from the theory. This is because for fermionic fields the divergence is logarithmic:

$$(m_H)^2 = (m_{H,bare})^2 + \frac{C\lambda}{\pi^2}(m_{H,bare})^2 \ln(\frac{\Lambda}{m_{H,bare}}) \tag{1.6}$$

1.4 Supersymmetry as the solution to the hierarchy problem

But the most natural solution to the hierarchy problem would be to cancel the anomalously divergent terms explicitly. That means that for every Lagrangian term of the form Eq. 1.4 there has to be one which is the negative of it. It turns out that this implies the existence of a new kind of symmetry - symmetry between bosons and fermions. The

Table 1.2: The undiscovered particles in the Minimal Supersymmetric Standard Model (with sfermion mixing for the first two families assumed to be negligible)

Names	Spin	P_R	Gauge Eigenstates	Mass Eigenstates
Higgs bosons	0	+1	$H_u^0\ H_d^0\ H_u^+\ H_d^-$	$h^0\ H^0\ A^0\ H^\pm$
squarks	0	−1	$\widetilde{u}_L\ \widetilde{u}_R\ \widetilde{d}_L\ \widetilde{d}_R$	(same)
			$\widetilde{s}_L\ \widetilde{s}_R\ \widetilde{c}_L\ \widetilde{c}_R$	(same)
			$\widetilde{t}_L\ \widetilde{t}_R\ \widetilde{b}_L\ \widetilde{b}_R$	$\widetilde{t}_1\ \widetilde{t}_2\ \widetilde{b}_1\ \widetilde{b}_2$
sleptons	0	−1	$\widetilde{e}_L\ \widetilde{e}_R\ \widetilde{\nu}_e$	(same)
			$\widetilde{\mu}_L\ \widetilde{\mu}_R\ \widetilde{\nu}_\mu$	(same)
			$\widetilde{\tau}_L\ \widetilde{\tau}_R\ \widetilde{\nu}_\tau$	$\widetilde{\tau}_1\ \widetilde{\tau}_2\ \widetilde{\nu}_\tau$
neutralinos	1/2	−1	$\widetilde{B}^0\ \widetilde{W}^0\ \widetilde{H}_u^0\ \widetilde{H}_d^0$	$\widetilde{N}_1\ \widetilde{N}_2\ \widetilde{N}_3\ \widetilde{N}_4$
charginos	1/2	−1	$\widetilde{W}^\pm\ \widetilde{H}_u^+\ \widetilde{H}_d^-$	$\widetilde{C}_1^\pm\ \widetilde{C}_2^\pm$
gluino	1/2	−1	$\widetilde{g}$	(same)
goldstino (gravitino)	1/2 (3/2)	−1	$\widetilde{G}$	(same)

canceling term for the Higgs loop is produced by the Higgs's fermionic counterpart - the Higgsino. All elementary particles have such "superpartners" which leads to many new particles predicted by Supersymmetry(SUSY), as illustrated in Table 1.2 [4].

1.5 Higgs sector in SUSY

Another notable feature of supersymetric models is that one Higgs field doublet is not sufficient to describe the electroweak symmetry breakdown. Two doublets (H_u and H_d) are necessary, producing six real scalar fields in unitary gauge [4]. Among these real and observable (providing supersymmetry does exist) fields the most interesting are the so-called charged Higgs bosons (H^+ and H^-). This charged scalar particle would compete against the vector boson $W^{+/-}$ in the top quark decays. Therefore the cross section of the $t\bar{t} \rightarrow \tau + jets$ process would be significantly changed compared to the Standard Model predictions. This dissertation describes the study of this important process as the first

step in searching for the charged Higgs at Run II of the Tevatron.

CHAPTER 2

TOP QUARK PAIR PRODUCTION AND DECAY

2.1 Experimental signatures of the top quark

There are two main ways to test the validity and consistency of top quark physics : virtual top contributions in precise electroweak measurements ([5]) and direct $t\bar{t}$ production. The virtual top constraint is based on an idea that W and Z boons propagators receive contributions from the virtual $t\bar{b}$ and $t\bar{t}$ loops (Figure 2.1).

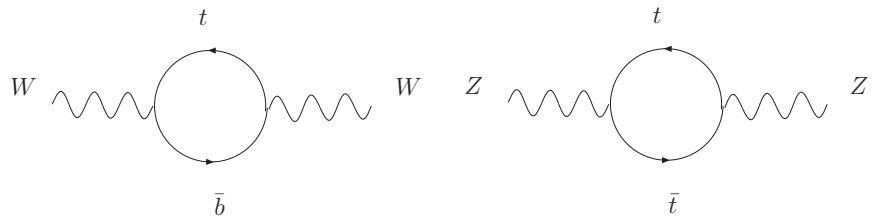

Figure 2.1: Virtual top loop contribution to W and Z masses.

Because of this the vector boson's mass gets shifted by

$$\Delta r = -\frac{3G_F}{8\sqrt{2}\pi^2 \tan\theta_W{}^2 m_t{}^2} \tag{2.1}$$

where G_F is the Fermi constant, m_t is the top mass and $\theta_W = \sqrt{\arcsin(1 - \frac{m_W{}^2}{m_t{}^2})}$ is the Weinberg angle.

The effect, however, is too small to yield a tight constraint on the top quark mass. This, however, was the only experimental way to determine the top mass before $t\bar{t}$ discovery in

1995 at the Tevatron [6]. Since then, using direct top pair production, top mass and other properties have been measured much more precisely, as can be seen in Figure 2.2.

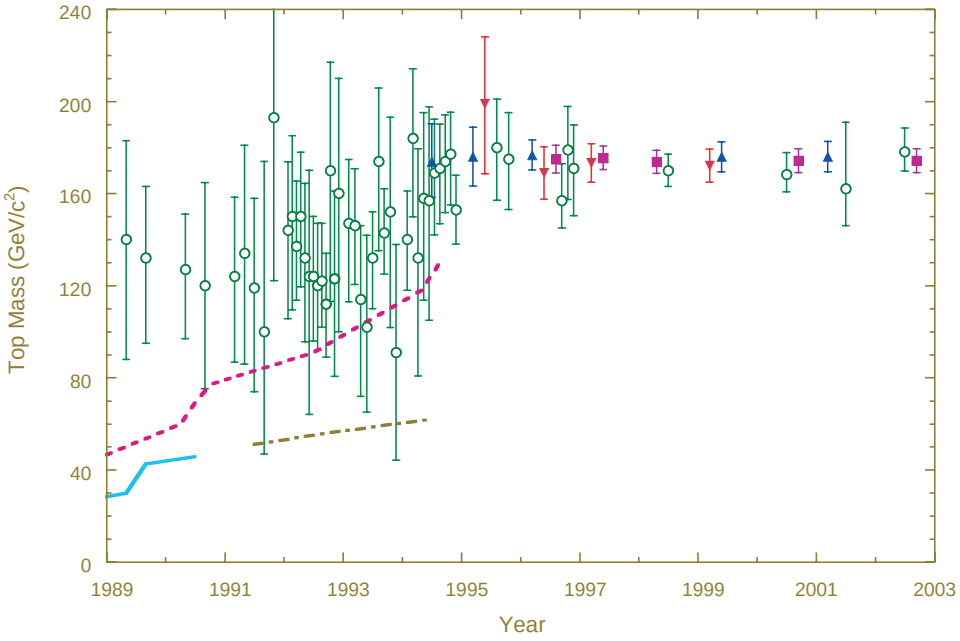

Figure 2.2: Evolution of the top quark mass prediction and measurement over the years. The circles represent indirect bounds. [8].

So, the direct pair production is indeed the best way to study the top quark.

2.2 Production cross section

The main mode of $t\bar{t}$ production in hadron collisions is through the strong interaction. The main contributing Feyman diagrams are illustrated in Figure 2.3.

The $t\bar{t}$ production mechanism at hadron colliers is complicated by the fact that protons and antiprotons aren't fundamental particles and are composed instead of partons (quarks and gluons). Each pair of partons i and j can contribute to the total cross section, so we need to take into account $\hat{\sigma}^{ij}$ and their relative weight in the $p\bar{p}$ collision, quantified by the so-called Parton Distribution Function (PDF) $f_i(x, {\mu_F}^2)$. PDFs are the functions of the parton's momentum fraction within the proton (x) and the factorization scale of the

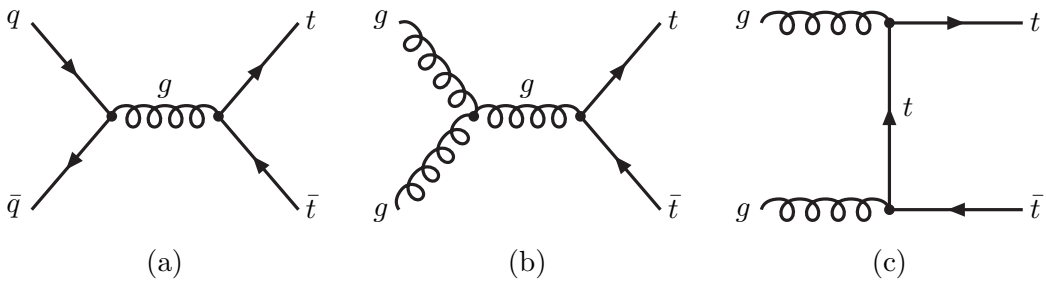

Figure 2.3: Top quark pair production, the leading order QCD diagrams at the Tevatron collider.

process (μ_F). This scale signifies the long-scale non-perturbative part of the cross section, which we are factoring in PDFs to be measured experimentally. A typical result of such measurements is illustrated in Figure 2.4.

As can be seen the dependence on the choice of factorization scale is fairly strong, so one has to pick PDFs close to the characteristic energy scale of the process. For top physics $\mu_F = Q = m_t = 175$ GeV is the proper choice. But what are the typical values of x? This can be estimated with a simple kinematic calculation [7]. The total center-of-mass energy of the $p\bar{p}$ collision is simply $\sqrt{s} \equiv \sqrt{2p_1p_2}$, while the effective energy of the colliding partons is $\sqrt{\hat{s}} = \sqrt{2x_1x_2p_1p_2} = \sqrt{x_1x_2s}$. At least $2m_t$ of energy is needed to produce a top pair, so the threshold value of x has to be $\approx \frac{2m_t}{\sqrt{s}}$. For the Tevatron ($\sqrt{s} = 1.96$ TeV) we have $x \approx 0.18$, which according to Figure 2.4 means that quark diagrams dominate $t\bar{t}$ production.

The total cross section can now be written as:

$$\sigma^{p\bar{p}\to t\bar{t}+X} = \sum_{i,j=q,\bar{q},g} \int dx_i dx_j f_i(x_i,\mu^2) \bar{f}_j(x_j,\mu^2) \hat{\sigma}^{i,j\to t\bar{t}}(\rho, m_t, \alpha_s(\mu^2), \mu^2) \tag{2.2}$$

where α is strong force's running coupling constant, arising as solution of the one-loop Renormalization Group Equation [9]:

$$\alpha_s(\mu^2) = -\frac{\alpha_s({\mu_R}^2)}{1 + b \ln \frac{\mu^2}{\mu_R}} \tag{2.3}$$

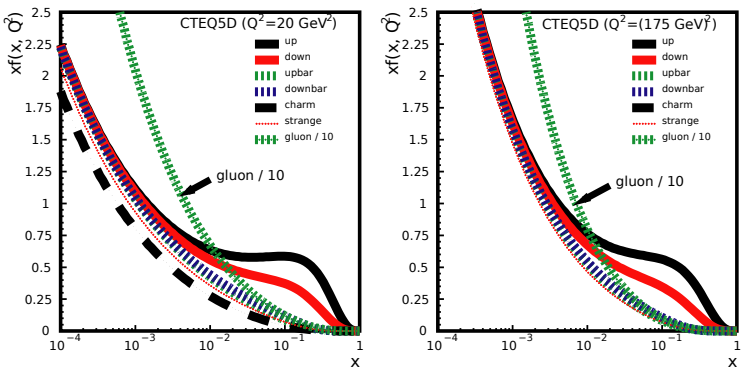

Figure 2.4: The quark, anti-quark, and gluon momentum densities in the proton as a function of the longitudinal momentum fractions x at $\mu_F = Q = \sqrt{20}$ (left) and $\mu_F = Q = m_t$ (right).

Here $b = (33 - 2n_f)/12\pi$ with n_F being the number of "active" flavors, that is the quarks lighter than μ. The renormalization scale μ_R is usually selected to be the same as the factorization scale. While this scale for top physics is normally chosen to be at m_t this choice biases the $t\bar{t}$ cross section prediction somewhat, as can be seen in Figure 2.5.

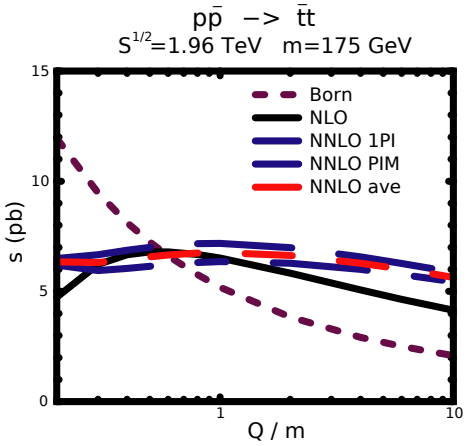

Figure 2.5: The renormalization scale ($\mu_F = Q$) dependence of the $t\bar{t}$ cross section [10].

Another important parameter is the top mass choice. Figure 2.6 demonstrates how the cross section is decreasing at higher masses due to smaller phase space. Both effects contribute to the theoretical uncertainties on the Standard Model $t\bar{t}$ cross section prediction. For the standard choice of parameters ($\mu_F = Q = m_t = 175GeV$ and $\sqrt{s} = 1.96TeV$) this

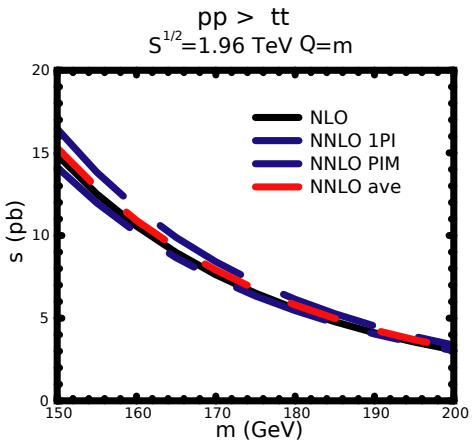

Figure 2.6: The top quark mass dependence of the $t\bar{t}$ cross section [10].

prediction is:

$$\sigma(p\bar{p} \rightarrow t\bar{t} + X) = 6.77 \pm 0.42\, pb \tag{2.4}$$

2.3 Top quark pair decay

While $t\bar{t}$ production is a QCD process, the decay of each of the two top quarks in the pair is electroweak process with the coupling at the decay vertex given by $\frac{-ig}{2\sqrt{2}}\bar{t}\gamma^{\mu}(1-\gamma^{5})V_{tb}bW_{\mu}$. In the SM $|V_{tb}|$ is close to 1 and the b-quark mass is negligible (compared to top) yielding the following total decay width to first order [11]:

$$\Gamma_t = \frac{G_F {m_t}^3}{8\pi\sqrt{2}}\left(1-\frac{{m_W}^2}{{m_t}^2}\right)^2\left(1+2\frac{{m_W}^2}{{m_t}^2}\right)\left(1-2\frac{\alpha_s}{3\pi}\left(\frac{2\pi^2}{3}-\frac{5}{2}\right)\right) = 1.5\, GeV \tag{2.5}$$

The W boson in turn decays into quarks ($BR = 6/9$) or leptons ($BR = 3/9$). Therefore, one can identify three main classes of $t\bar{t}$ final states:

- $t\bar{t} \rightarrow W^{+}b\,W^{-}b \rightarrow q_1\bar{q}_2 b\, q_3\bar{q}_4\bar{b}$ (the "all-jets" channel)
- $t\bar{t} \rightarrow W^{+}b\,W^{-}b \rightarrow \bar{l}\nu_l b\, q_1\bar{q}_2\bar{b}$ or $q_1\bar{q}_2 b\, l\bar{\nu}_l\bar{b}$ (the "lepton-jet" channel)
- $t\bar{t} \rightarrow W^{+}b\,W^{-}b \rightarrow \bar{l_1}\nu_l b\, l_2\bar{\nu}_l\bar{b}$ (the "lepton+jets" channel)

The "pie chart" in Fig. 2.7 demonstrates the relative branching fractions of these channels. From the experimental point of view lepton+jets [12] are the best channels, since di-leptons [13] have a very small cross section, while the all-jets channel [14] has overwhelming multijet QCD background. The $\tau + jets$ channel suffers from the same QCD problem, as will be described in Chapter 5. However, it is very important for testing the SM, especially the flavor universality, which is violated in many modern theories, some of which require the existence of charged Higgs bosons.

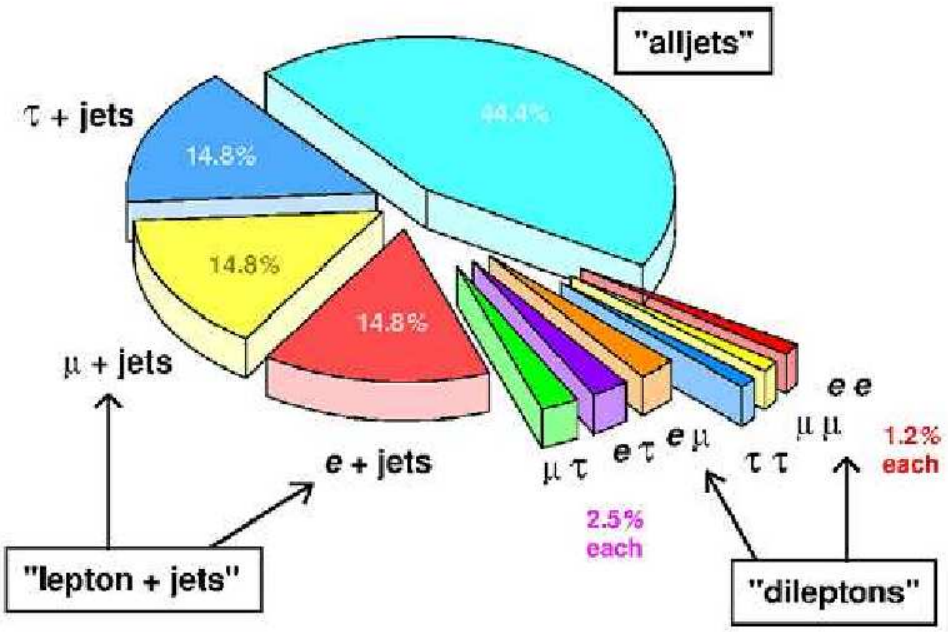

Figure 2.7: "Pie chart" displaying the branching fractions of different final states of top quark pair decay.

CHAPTER 3

THE HIGGS SECTOR IN THE STANDARD MODEL AND BEYOND

3.1 Standard Model Higgs

In the Standard Model electroweak symmetry is broken by introducing a scalar field, known as the Higgs field. But as described in §8.3 of [15], any complex scalar field breaks $SU(2)$ symmetry explicitly and completely across the entire parameter space. Since we want a *spontaneous* breakdown we must have a neutral component in the Higgs doublet. In other words, $\Phi \equiv \binom{\Phi^+}{\Phi^0}$.

This scalar field should have potential as in eq. 1.3, which means the gauge-invariant Lagrangian has to contain this potential along with appropriate pieces for fermion-fermion, fermion-scalar and vector boson-scalar interactions:

$$L_{unbroken} = L_{f-f} + L_{f-s} + L_{v-s} + (D_\mu \Phi)^\dagger (D^\mu \Phi) + \mu^2 \Phi \Phi^* - \lambda (\Phi \Phi^*)^2 \qquad (3.1)$$

where D_μ is the covariant (meaning Lorentz-invariant) derivative. For electroweak theory (SM excluding QCD) $D_\mu \equiv \partial_\mu - \frac{i}{2} g \tau \cdot \mathbf{A}_\mu - \frac{i}{2} g\prime B_\mu$, where g and $g\prime$ are the coupling constants of the electroweak force. At this point the Lagrangian of the theory is gauge-symmetric. But the scalar field has a non-zero vacuum expectation value, which can be without loss of generality written as the following:

$$< 0|\Phi|0 >= \begin{pmatrix} 0 \\ \frac{v}{\sqrt{2}} \end{pmatrix} \qquad (3.2)$$

where $v = (\mu^2/\lambda^2)^{\frac{1}{2}} = 2^{-1/4}{G_F}^{-1/2} \simeq 250$ GeV. This means that close to the "vacuum" state (near the minima of $V(x)$) the Lagrangian in eq. 3.1, expressed in terms of the scalar doublet Φ, can no longer be used for perturbative calculations. It is, however, possible to rewrite Φ in terms of 4 real scalar fields with vanishing VEVs, $\zeta_{1,2,3}$ and η:

$$\Phi = U^{-1}(\zeta)\begin{pmatrix} 0 \\ \frac{v+\eta}{\sqrt{2}} \end{pmatrix} \tag{3.3}$$

3 of these fields (called Goldstone bosons), however, disappear once we transform into the unitary gauge:

$$\Phi' = U^{-1}(\zeta)\begin{pmatrix} 0 \\ \frac{v+\eta}{\sqrt{2}} \end{pmatrix} \tag{3.4}$$

Now we can obtain the new (broken) Lagrangian, expressed in terms of the only real physical scalar field $\eta(x)$ remaining:

$$L_{broken} = L_{f-f} + L_{f-s} + L_{v-s} + (D_\mu \Phi'(\eta))^\dagger (D^\mu \Phi'(\eta)) - \mu^2\eta^2 - \lambda v\eta^3 - \frac{\lambda}{4}\eta^4 \tag{3.5}$$

As one can see, the new emerging terms ($-\mu^2\eta^2 - \lambda v\eta^3 - \frac{\lambda}{4}\eta^4$) are not gauge-invariant, which means that symmetry indeed spontaneously breaks. Not only that, but the new scalar field obtains mass, given by the term $\mu^2\eta^2$. It turns out, that once we express L_{f-f},L_{f-s} and L_{v-s} in terms of η the corresponding fields also get mass (self-interactive) Lagrangian terms. These terms are in fact proportional to the VEV of the scalar field $\eta(x)$:

$$M_\mu = \sqrt{2}\mu \tag{3.6}$$

$$m_f = f^l v/\sqrt{2} \tag{3.7}$$

$$M_W = gv/4 \tag{3.8}$$

$$M_Z = v\sqrt{g^2 + {g'}^2}/2 \tag{3.9}$$

where $f^{(f)}$ is the coupling constant in $L_{v-f} = f^{(f)}\bar{(}f)_1 \Phi f_2$. This field is called the Higgs

boson and, as can be seen from the preceding equation, it defines the entire mass spectrum of the Standard Model:

Because of this it is often said that the Higgs boson is "the origin of mass." Discovery of this particle is perhaps the most important goal of particle physics today, since it is the last "missing piece" of the Standard Model. The picture is even more interesting in the scenarios beyond the SM.

3.2 SUSY Higgs

Many of the proposed theoretical models require an extension of the SM Higgs sector to 2HDMs (Two-Higgs Doublet Models). Most prominent among them is MSSM, which is the basis of all SUSY theories [16]. There are many reasons why one chiral Higgs multiplet is not sufficient in MSSM. For one thing, the necessary conditions for the gauge field anomaly diagrams cancellation are violated for the Higgs's superpartners, so two Higgs doublets are needed to cancel each other's effect [4]. But even without invoking such an argument, the very nature of the supersymmetric Lagrangian requires two Higgs. Such a Lagrangian is customarily expressed in terms of the so-called "superpotential" W:

$$L_{SUSY} = -\partial^{\mu}\phi^{*i}\partial_{\mu}\phi_i - i\psi^{\dagger i}\bar{\sigma}^{\mu}\partial_{\mu}\psi_i - \frac{1}{2}\left(W^{ij}\psi_i\psi_j + W^{*}{}_{ij}\psi^{\dagger i}\psi^{\dagger j}\right) \tag{3.10}$$

For MSSM the superpotential is:

$$W_{MSSM} = \bar{u}\mathbf{y_u}QH_u - \bar{d}\mathbf{y_d}QH_d - \bar{e}\mathbf{y_e}LH_d + \mu H_u H_d\,. \tag{3.11}$$

Since the superpotential must be analytic, the $\bar{u}QH_u$ Yukawa terms cannot be replaced by something like $\bar{u}QH_d^*$, so both terms must be present, hence - two Higgs doublets. These two have opposite hypercharges: $Y = 1/2$ and $Y = -1/2$. So, we now have two complex $SU(2)_L$-doublets, which is equivalent to eight real, scalar degrees of freedom.

When the electroweak symmetry is broken (just like in the previous section), three of them are the would-be Nambu-Goldstone bosons G^0, $G^{\pm}$. The remaining five Higgs scalar mass eigenstates consist of two CP-even neutral scalars h^0 and H^0, one CP-odd neutral scalar A^0, and a charge $+1$ scalar H^+ and its conjugate charge -1 scalar H^-. The masses of these scalars are given by (to the leading order):

$$M^2_{A^0} = 2|\mu|^2 + M^2_{H_u} + M^2_{H_d} \tag{3.12}$$

$$M^2_{h^0,H^0} = \left(M^2_{A^0} + M^2_Z \mp \sqrt{(M^2_{A^0} - M^2_Z)^2 + 4M^2_Z M^2_{A^0}\sin^2(2\beta)}\right) \tag{3.13}$$

$$M^2_{H^\pm} = M^2_{A^0} + M^2_W \tag{3.14}$$

β is a very important parameter of the model, representing the ratio of VEVs of the two Higgs doublets: $\tan(\beta) = \frac{v_u}{v_d}$

3.3 Experimental signature of charged Higgs

Since Higgs coupling is proportional to mass it favors heavy τ to light e and μ. This prompts us to search for H^+ decaying to τ. If the charged Higgs also happens to be lighter then the top quark it is possible to search for it in top pair decays directly. Figure 3.1 [17] summarizes the relative BRs of different decays of $H^\pm$ as well as BR($t \to H^\pm b$), which would be the main production channel of charged Higgs at the Tevatron collider (section 4). DØ and CDF have performed such searches in Run I of the Tevatron ([18, 19]).

Table 3.1 shows all possible decay modes of $t\bar{t} \to \tau + X$ available if the H^+ exists. DØ [19] had optimized their selection criteria for the states 2, 4 and 5 ($\tau + jets$ channel). CDF [18] had chosen 1, 3 and 5 ($\tau + e$ and $\tau + \mu$ channels). Both analyses had to take into account the ditau channel. The measurement described in this dissertation establishes the foundation for undertaking such a search at Run II.

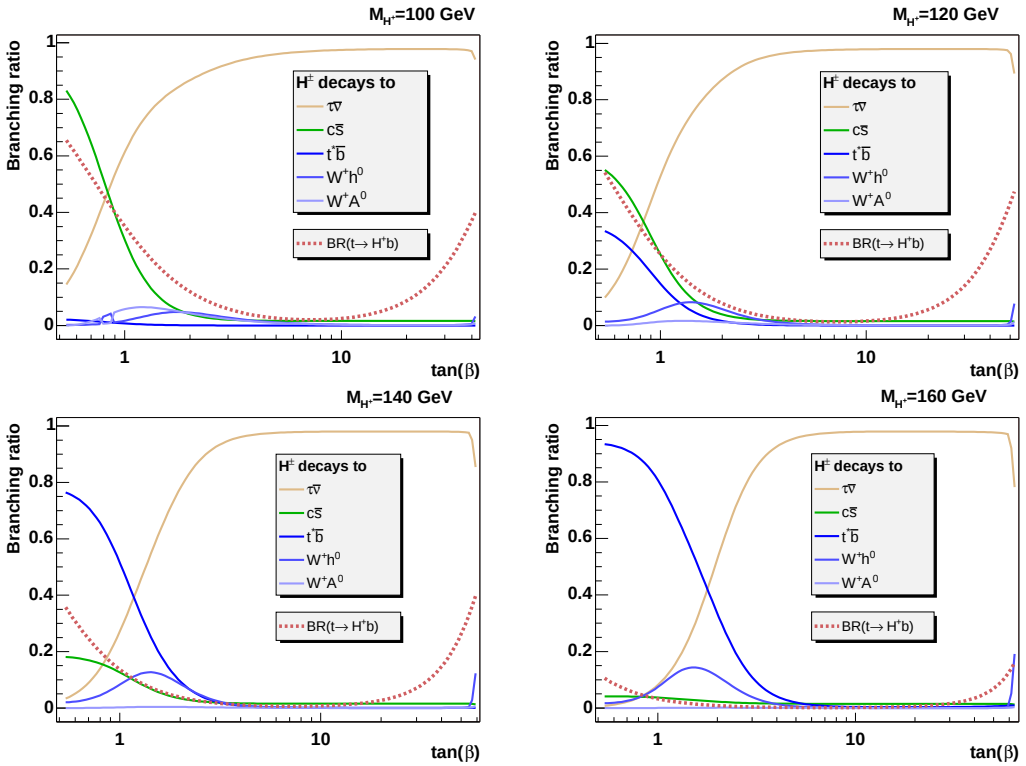

Figure 3.1: Charged Higgs production and decay versus $tan(\beta)$ for H^+ masses of 100, 120, 140 and 160 GeV

Table 3.1: Decay modes and their branching ratios, for $\tau + jets$, assuming large $\tan\beta$. The l refers to any single lepton channel (e or μ).

Final state	First decay	Secondary decays	BR for secondary decays at large $\tan\beta$
1	$t\bar{t}\rightarrow W^{\mp}W^{\pm}b\bar{b}$	$W^{\mp}\rightarrow\tau^{\mp}\nu$, $W^{\pm}\rightarrow l\nu$	0.012
2	$t\bar{t}\rightarrow W^{\mp}W^{\pm}b\bar{b}$	$W^{\mp}\rightarrow\tau^{\mp}\nu$, $W^{\pm}\rightarrow jets$	0.074
3	$t\bar{t}\rightarrow W^{\mp}H^{\pm}b\bar{b}$	$W^{\mp}\rightarrow l\nu$, $H^{\pm}\rightarrow\tau^{\pm}\nu$	0.11
4	$t\bar{t}\rightarrow W^{\mp}H^{\pm}b\bar{b}$	$W^{\mp}\rightarrow jets$, $H^{\pm}\rightarrow\tau^{\pm}\nu$	0.64
5	$t\bar{t}\rightarrow H^{\mp}H^{\pm}b\bar{b}$	$H^{\mp}\rightarrow\tau^{\mp}\nu$, $H^{\pm}\rightarrow\tau^{\pm}\nu$	0.95

CHAPTER 4

THE DØ DETECTOR AT THE TEVATRON ACCELERATOR

4.1 The Tevatron (Fig. 4.1)

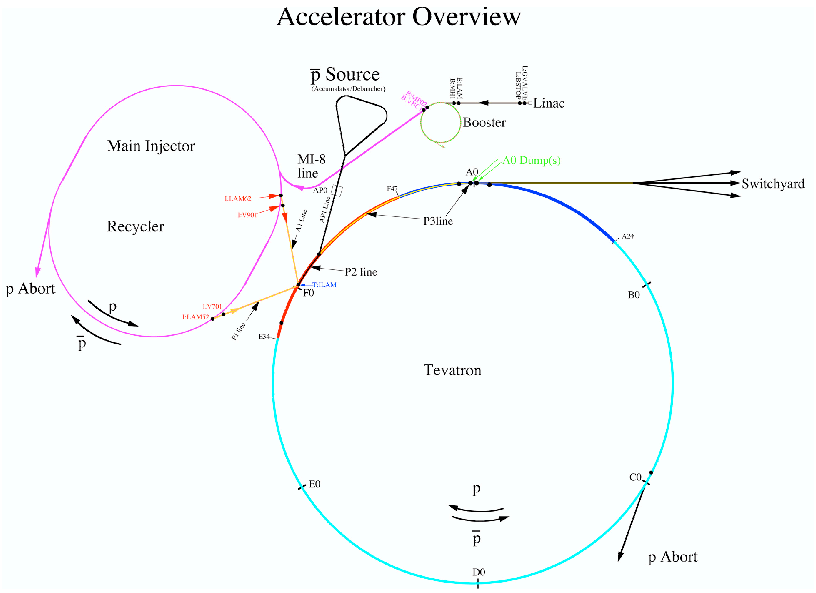

Figure 4.1: The Fermilab Collider Complex.

The Tevatron collider complex at Fermi National Accelerator Laboratory is currently the highest energy hadron particle collider on the planet. It accelerates proton and antiproton beams to an energy of 0.98 TeV each and collides them at two interaction points. DØ and CDF, two complex multi-purpose particle detectors located at these points study the outcome of these collisions. The analysis presented in this dissertation was performed with the data collected by the DØ experiment.

During the first run (1992-1996) of the Tevatron about 130 pb^{-1} of total luminosity

Table 4.1: Tevatron Collider Parameters.

Parameter	Run I	Run II	units
Peak luminosity	$1.6 \cdot 10^{30}$	$92 \cdot 10^{30}$	$\mathrm{cm}^{-2}\mathrm{s}^{-1}$
Integrated luminosity	3.2	18	$\mathrm{pb}^{-1}/\mathrm{wk}$
Total collected lumi	0.1	0.56	fb^{-1}
Beam energy	900	980	GeV
Number of bunches	6x6	36x36	
Protons/bunch	$230 \cdot 10^9$	$260 \cdot 10^9$	
Anti-Protons/bunch	$55 \cdot 10^9$	$38 \cdot 10^9$	
Proton emittance, 95%	23	19	$\pi\mu$m
Pbar emittance, 95%	13	17	$\pi\mu$m
β^* at IP	35	35	cm
Pbar production rate	$6.0 \cdot 10^{10}$	$13.5 \cdot 10^{10}$	hr^{-1}

was collected by each of the detectors. In 1995 this culminated in an especially remarkable discovery - the existence of the top quark, the last remaining "building block of nature" which was confirmed by both collaborations.

After the end of Run I the Tevatron underwent a significant upgrade in hopes of more exciting finds during Run II. Most importantly, the Main Ring was replaced with the Main Injector, which led to a large increase in the instantaneous luminosity. Also, the center-of-mass energy was increased to 1.96 TeV. Table 4.1 shows a comparison of the most notable features of the Tevatron in Run I and Run II [21, 22].

The Tevatron collider is in fact the last in a chain of different accelerators (Fig. 4.1) raising the proton's energy up until it reaches 150 GeV before being sent into the Tevatron Ring:

- Cockroft-Walton preaccelerator - accelerates hydrogen ions to 750 KeV
- Linear Accelerator - accelerates ions to 400 MeV and removes electrons
- The Booster Synchrotron - accelerates protons to 8 GeV and also supplies the

Anti-proton Source with them

- The Main Injector - accelerates protons to 150 GeV

The antiprotons are created in the Anti-proton Source and then pass through the Debuncher and Accumulator before entering the Tevatron Synchrotron.

4.2 DØ detector

4.2.1 The Detector (Fig. 4.2)

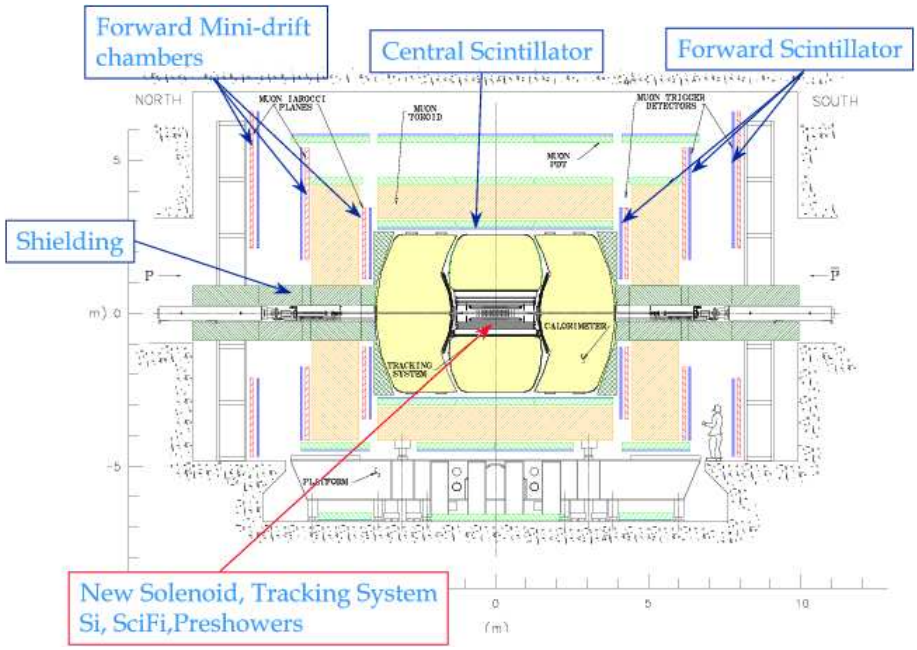

Figure 4.2: The DØ Detector [23]

The DØ experiment was proposed in 1983 to study proton-antiproton collisions at a center-of-mass energy of 1.8 TeV at the Fermilab Tevatron collider [24]. Its main distinctive features were excellent calorimeter compensation and segmentation (section 4.2.5) as well as an accurate dedicated muon system with wide η coverage (section 4.2.6). After successful operation in Run I, the detector underwent a major upgrade before the start

of the Run II physics program [25]. The most important additions were a Solenoid magnet and a new Silicon Microstrip Tracker (SMT) (section 4.2.3) which allowed efficient Secondary Vertex (SVT) tagging of b-jets, which is central to the $t\bar{t} \rightarrow \tau + jets$ analysis (section 5.7).

The major subsystems of the DØ detector are (from inner to outer radius as shown in Fig. 4.2):

- the Central Tracking System
- the Calorimeter
- the Muon System

All of them use the same coordinate system (see Figure4.3) .

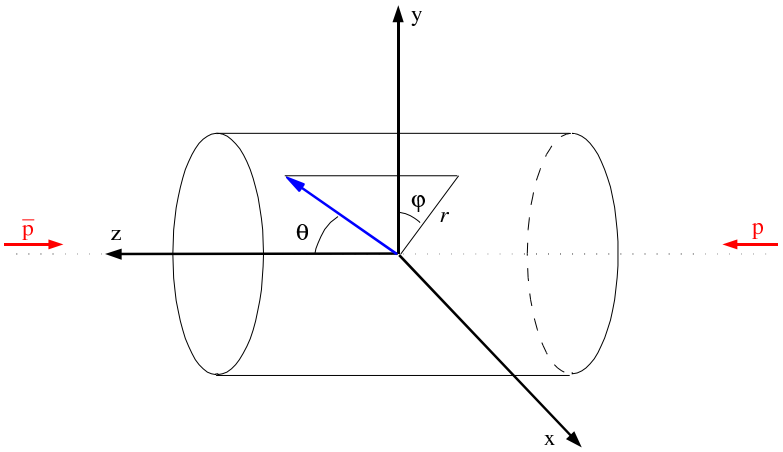

Figure 4.3: The DØ Detector Coordinate System.

4.2.2 The DØ Coordinate System

In the DØ Cartesian coordinate system (Fig. 4.3) the z axis points along the proton beam direction, the y axis - vertically upwards, and the x axis lies in the horizontal plane to correspond to a right-handed system. However, the polar coordinates are much more

suitable, due to cylindrical symmetry of the detector. The azimuthal angle ϕ spans 0 to 2π and the polar angle θ is counted from the z axis.

But these are also not sufficiently convenient variables due to peculiarities of the collision kinematics. The partons' total energy fraction cannot be measured in hadron collider experiments because remnants of the collided nucleons are lost down the beam pipe. Thus, the center-of-mass energy of the colliding partons remains unknown and the total momentum balance cannot be used for kinematic calculations. On the other hand, the momenta have to be balanced in the plane transverse to the beam direction and this can be exploited to construct a useful set of variables [20]. In the traditional set of variables which describe a particle's 4-momentum, (E, p_x, p_y, p_z), neither E nor p_z are invariant with respect to a boost along the z-direction.

The Lorentz transformation from the lab frame to the frame moving along the z-direction can be written as

$$p'_z = p_z \cosh y - E \sinh y$$

$$E' = -p_z \sinh y + E \cosh y$$

where y is rapidity.

The rapidity can be expressed as

$$y = \frac{1}{2} \ln \frac{E + p_z}{E - p_z}$$

or

$$y = \frac{1}{2} \ln \frac{1 + \beta \cos\theta}{1 - \beta \cos\theta}$$

where $\beta = p/E$.

Using the rapidity, any particle with mass m can be described with a set of kinematic variables, (p_T, y, ϕ, m). The advantage of such a system is that a boost along the z-direction only shifts the rapidity by a constant and leaves p_T, ϕ and m the same. This is the standard way to define 4-momenta at hadron collider experiments and it is used

everywere on DØ including this analysis.

In the limit $\beta \to 1$ we can define pseudorapidity as

$$\eta \equiv \frac{1}{2} \ln \frac{1 + \cos\theta}{1 - \cos\theta} = -\ln \tan \frac{\theta}{2}$$

which is a good approximation for Tevatron energies and is widely used. An angular distance between two objects is often expressed in terms of $\Delta R = \sqrt{(\Delta\phi)^2 + (\Delta\eta)^2}$, where $|\Delta\phi| < 2\pi$.

The transverse momentum of a particle is defined in terms of the 3-momentum $\vec{p}$ as

$$p_T = |\vec{p}| \sin\theta.$$

The transverse energy by definition is

$$E_T \equiv \sqrt{p_x^2 + p_y^2 + m^2} = \sqrt{p_T^2 + m^2} = \sqrt{E^2 - p_z^2}$$

and will be equal to $E \sin\theta$ only in the limit $\beta \to 1$.

4.2.3 The Central Tracking System

The tracking system (Fig. 4.4) consists of an inner silicon microstrip tracker (SMT), surrounded by a central scintillating fiber tracker (CFT). These systems are contained within the bore of a 2T superconducting solenoid, which is surrounded by a scintillator preshower detector.

The two tracking detectors locate the primary interaction vertex with a resolution of about 35 μm along the beamline. They can tag b-quark jets with an impact parameter resolution of better than 15 μm in $r - \phi$ for particles with transverse momentum $p_T >$ 10 GeV at $|\eta| = 0$. The high resolution of the vertex position allows good measurement

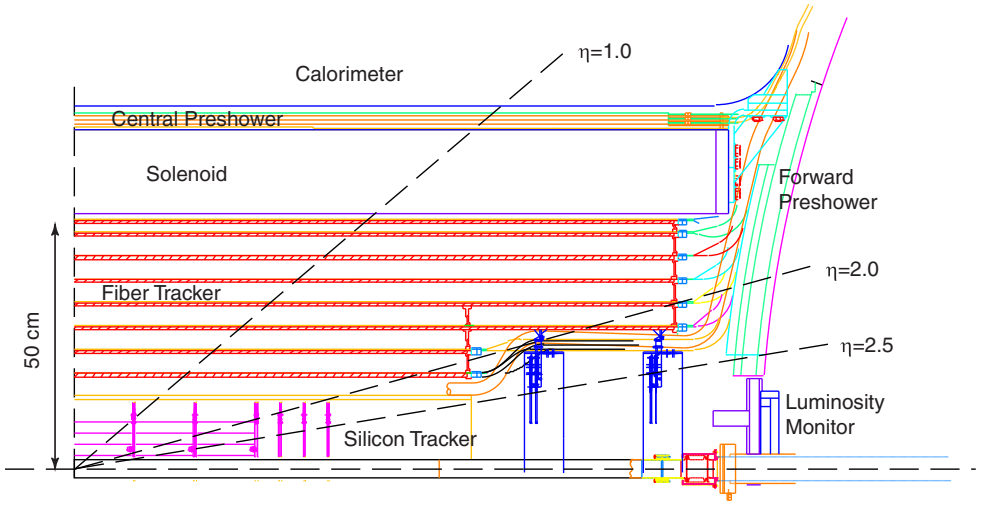

Figure 4.4: $r-z$ view of the tracking system. [23]

of lepton p_T, jet transverse energy (E_T), and missing transverse energy $\not\!\!E_T$.

4.2.3.1 Silicon Microstrip Tracker

The Silicon Microstrip Tracker is based on 50 μm pitch silicon microstrip detectors providing a spatial resolution of approximately 10 μm in $r\phi$. The high resolution is important to obtain good momentum measurement and vertex reconstruction. The detector consists of a system of barrels and interleaved disks designed to provide good coverage out to $|\eta| \approx 3$ for all tracks emerging from the interaction region, which is distributed along the beam direction with $\sigma_z \approx 25$ cm.

An isometric view of the SMT is shown in Fig. 4.5. The detector has six barrels in the central region. Each barrel has four silicon readout layers. The silicon modules installed in the barrels are called ladders. Layers 1 and 2 have twelve ladders each; layers 3 and 4 have twenty-four ladders each, for a total of 432 ladders. Each barrel is capped at high $|z|$ with a disk of twelve double-sided wedge detectors, called an F-disk. Forward of the three disk/barrel assemblies on each side is a unit consisting of three F-disks. In the far forward regions, two large-diameter disks, H-disks, provide tracking at high $|\eta|$. Twenty-four full

wedges, each consisting of two back-to-back single-sided half wedges, are mounted on each H-disk. There are 144 F-wedges and 96 full H-wedges in the tracker; each side of a wedge (upstream and downstream) is read out independently. The centers of the H-disks are located at $|z| = 100.4,\ 121.0$ cm; the F-disks are at $|z| = 12.5,\ 25.3,\ 38.2,\ 43.1,\ 48.1$, and 53.1 cm. The centers of the barrels are at $|z| = 6.2,\ 19.0,\ 31.8$ cm.

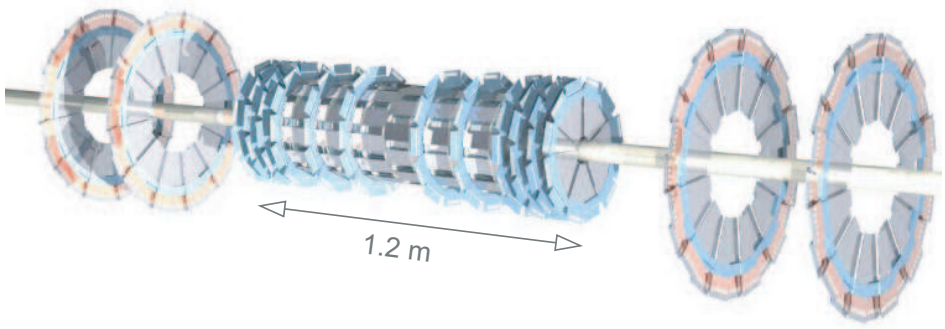

Figure 4.5: The DØ Silicon Microstrip Tracker. [25]

The SMT is read out by a custom-made front end CMOS readout chip (SVX IIe) [26]. It contains 128 channels, each channel comprising a double-correlated sampling amplifier, a 32-cell analog pipeline, and an analog-to-digital converter. The silicon tracker has a grand total of 912 readout modules, with 792,576 channels overall.

4.2.3.2 Central Fiber Tracker

The outer tracking in the central region is based on scintillating fiber technology with visible light photon counter (VLPC) readout [27]. The CFT consists of 8 layers, each containing 2 fiber doublets in a zu or zv configuration (z = axial fibers and $u, v = \pm 3^\circ$ stereo fibers). Each doublet consists of two layers of 830 μm diameter fibers with 870 μm spacing, offset by half the fiber spacing. The fibers are supported on carbon fiber support cylinders. This configuration provides very good efficiency and pattern recognition and results in a position resolution of ≈ 100 μm in $r\phi$. The CFT has a total of about 77,000

channels.

4.2.4 Preshower detectors

The central and forward preshower detectors (CPS and FPS) provide fast energy and position measurements for the electron trigger and offline electron identification. The preradiator consists of 5.5 mm lead in the CPS and 11 mm of lead in the FPS (see Fig. 4.6).

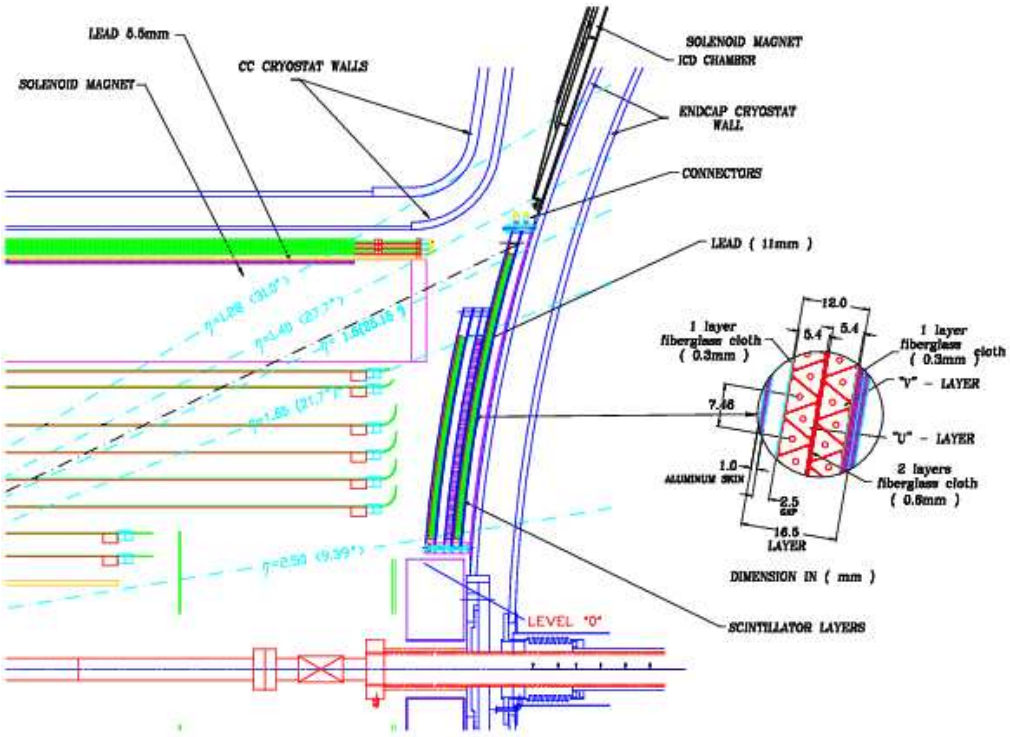

Figure 4.6: The central and forward preshower detectors. [23]

The CPS detector consists of three concentric cylindrical layers of interleaved triangular scintillator strips. The three layers are arranged in an xuv geometry (x = axial, $uv = \pm$ stereo angle of approximately 23°). Wavelength shifting fibers are used to pipe the light out to a VLPC readout system.

4.2.5 The Calorimeter

In the early era of particle collider experiments [28] it was found that hadrons produced in such collisions tend to be clustered in fairly narrow cones, flying in the same direction. Such objects, called "jets", are best measured by absorbing their energy by thick layers of dense material. Detectors based on this principle are called "calorimeters" and are standard in modern particle physics experiments.

A perfect calorimeter system should be

- hermetic (cover a solid angle close to 4π)
- compact
- well compensated (ratio $e/h \approx 1$, where e stands for the response to electron and h to hadron)

The DØ detector satisfies all these requirements admirably. In fact, it is the unmatched compensation and hermeticity of calorimeter system that allowed DØ to perform on par with CDF in Run I, despite the lack of a silicon tracker. For Run II the calorimeter system remained largely unchanged except for an electronic readout upgrade to account for higher luminosity and correspondingly larger trigger rate (section 4.2.7).

The DØ calorimeter system consists of three sampling calorimeters (primarily uranium/liquid-argon) and an intercryostat detector (Fig. 4.7). The depth of each layer of these three calorimeter sections is shown in Table 4.2 in the units of *radiation length* X_0 and *absorption length* λ (for uranium $X_0 = 0.32$ cm and $\lambda = 10.5$ cm, so the electromagnetic section contains about 0.6λ).

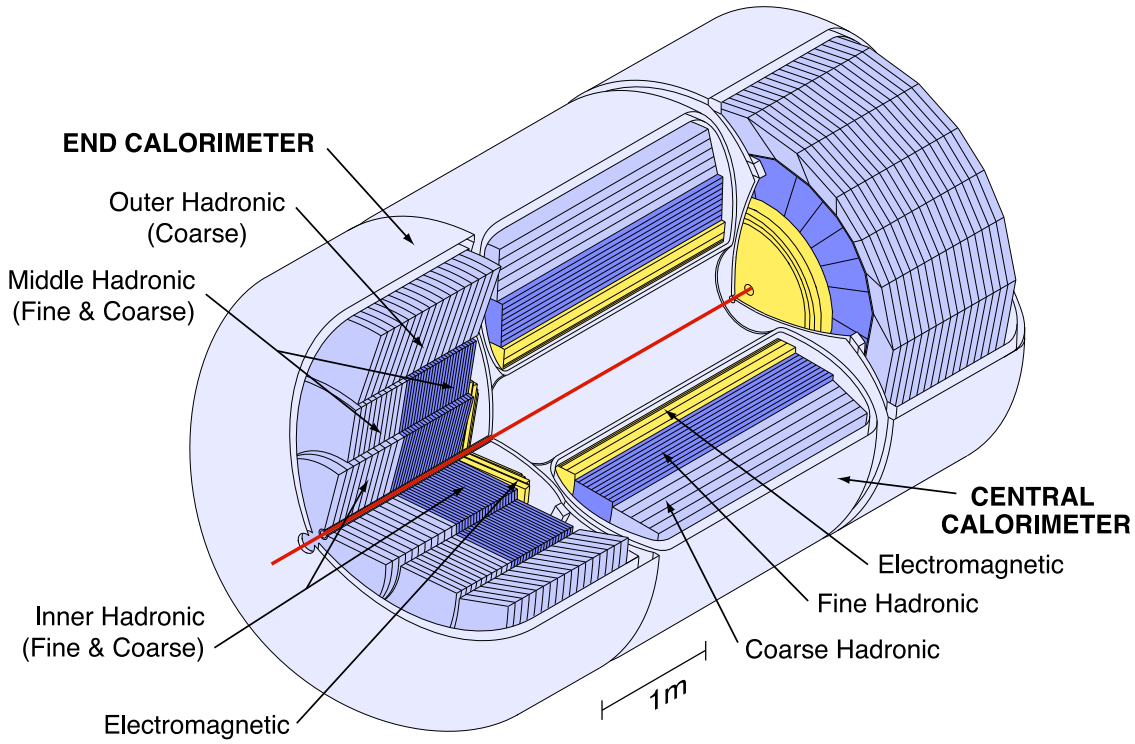

Figure 4.7: The DØ Calorimeter. [25]

4.2.5.1 Central and Endcap Calorimeters

As shown in Fig. 4.8, the central calorimeter (CC) covers $|\eta| < 1$ and the two end calorimeters, ECN (north) and ECS (south), extend coverage to $|\eta| \approx 4$. Each calorimeter contains an electromagnetic section closest to the interaction region followed by fine and coarse hadronic sections. The active medium for the calorimeters is liquid argon and each of the three calorimeters (CC, ECN, and ECS) is located within its own cryostat that maintains the detector temperature at approximately 90 K. Different absorber plates are used in different locations. The electromagnetic sections (EM) use thin plates (3 or 4 mm in the CC and EC, respectively), made from nearly pure depleted uranium. The fine hadronic sections are made from 6-mm-thick uranium-niobium (2%) alloy. The coarse hadronic modules contain relatively thick (46.5 mm) plates of copper (in the CC) or stainless steel (EC).

Table 4.2: The depth of the calorimeter layers at normal incidence ($\theta = \pi/2$).

	EM	FH	CH
CC Depth	$2, 2, 7, 10\ X_0$	$1.3, 1.0, 0.9\lambda$	3.2λ
EC Depth	$0.3, 2.6, 7.9, 9.3\ X_0$	$1.2, 1.2, 1.2\lambda$	3.6λ

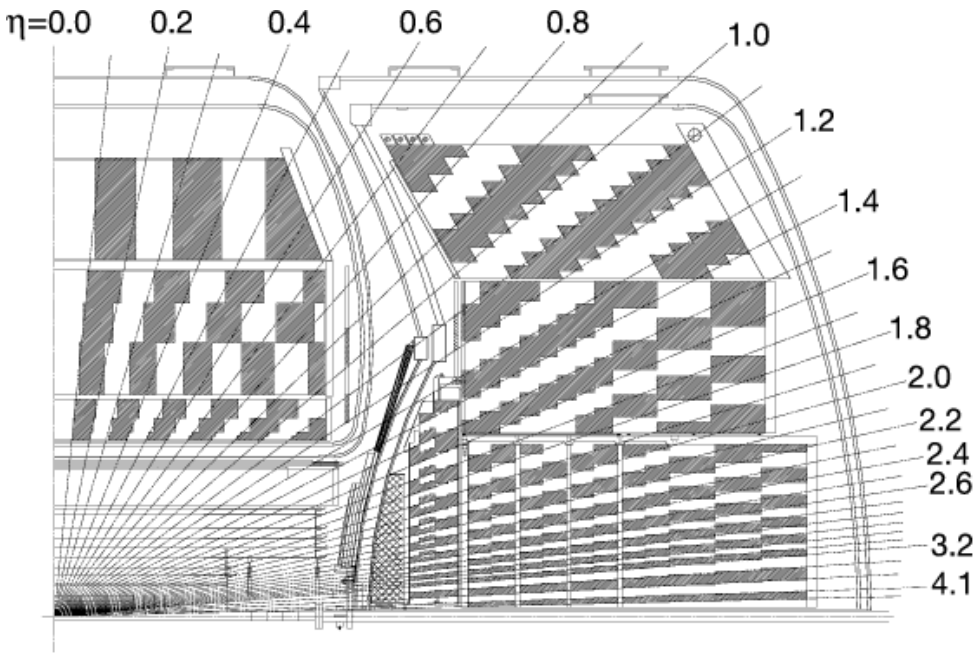

Figure 4.8: Schematic view of a portion of the DØ calorimeters showing the transverse and longitudinal segmentation pattern. The shading pattern indicates groups of cells ganged together for signal readout. The rays indicate pseudorapidity intervals from the center of the detector. [25]

A typical calorimeter cell has size of $\delta\eta \times \delta\phi = 0.1 \times 0.1$ (which defines the calorimeter segmentation) and is shown in Fig. 4.9. The electric field is established by grounding the metal absorber plates and connecting the resistive surfaces of the signal boards to positive high voltage (typically 2.0 kV). Passage of a charged particle from the hadronic or EM shower is detected by virtue of ionization of the liquid argon in the gap between the absorber plate and a G10 readout board. The electron drift time across the 2.3 mm liquid argon gap is approximately 450 ns.

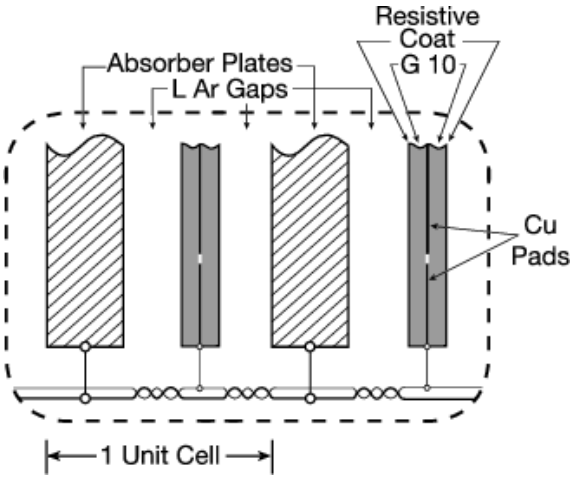

Figure 4.9: Calorimeter cell. [25]

Calorimeter readout cells form pseudo-projective towers as shown in Fig. 4.8, with each tower subdivided in depth. We use the term "pseudo-projective" because the centers of cells of increasing shower depth lie on rays projecting from the center of the interaction region, but the cell boundaries are aligned perpendicular to the absorber plates.

4.2.5.2 ICD and Massless Gaps

As can be seen in Fig. 4.8, the region $0.8 \leq |\eta| \leq 1.4$ contains a large amount of material, not covered by the standard calorimeter instrumentation. This includes the cryostat walls, module endplates and such. Rather than leaving gaps in the calorimeter,

an additional detector component was placed in each of those two regions. These two scintillation counter arrays are named the intercryostat detectors or ICDs. Each ICD consists of 192 scintillator tiles of size $\delta\eta = \delta\phi = 0.1$, which exactly matches the size of the regular calorimeter cells. The light output of the ICD tiles is collected by 1.3 cm diameter phototubes and sent over to the calorimeter electronics just as the liquid argon channels are.

In addition to ICDs there are two special regions in the calorimeter system - the so-called "Massless Gaps." They are special in that these channels have only the liquid argon and not the depleted uranium absorber plates. There are 320 such channels in CC and 192 in EC.

4.2.5.3 Calorimeter electronics

Figure 4.10 illustrates the main components in the calorimeter readout chain. There are 55,296 calorimeter electronics channels to be read out; 47,032 correspond to channels connected to physical readout modules in the cryostats. The remaining electronics channels are not connected to the detector. (The ADC cards are identical and contain enough channels to read out the most populated regions of the detector.) The readout is accomplished in three principal stages. In the first stage, signals from the detector are transported to charge preamplifiers located on the cryostats via low impedance coaxial cable. In the second stage, signals from the preamplifiers are transported on twisted-pair cables to the analog signal shaping and storage circuits on baseline subtractor (BLS) boards. The precision signals from the BLSs are transmitted on an analog bus and driven by analog drivers over 130 m of twisted-pair cable to ADCs. These signals then enter the data acquisition system for the Level 3 trigger decision (section 4.2.7) and storage to tape.

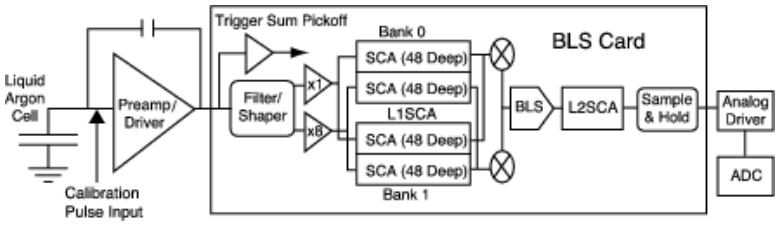

Figure 4.10: Readout chain of the calorimeter in Run II indicating the three major components: preamplifiers, baseline subtractor and storage circuitry (BLS), and the ADCs. [25]

4.2.5.4 Calorimeter Resolution

The calorimeter resolution is commonly parameterized in the form (the sign $\oplus$ means sum in quadrature)

$$\sigma/E = \sigma_S/\sqrt{E} \oplus \sigma_N/E \oplus C$$

where

σ_S represents the statistical sampling fluctuations

σ_N corresponds to the noise contribution

C is a constant due to calibration errors

The parameters for the DØ calorimeter are listed in Table 4.3.

Table 4.3: Resolution Parameters for the DØ Calorimeter.

	σ_S	σ_N	C
EM	0.13 $\text{GeV}^{1/2}$	0.40 GeV	0.015
HAD	0.80 $\text{GeV}^{1/2}$	1.5 GeV	0.04

4.2.6 The Muon System

Muons have sufficiently large lifetime to pass through the calorimeter depositing little energy in it. A dedicated muon detection system is needed in addition to the calorimeter.

For muon triggering and measurement, the upgraded DØ detector uses central muon system proportional drift tubes (PDTs) and toroidal magnets, central scintillation counters and a forward muon system. The central muon system provides coverage for $|\eta| < 1.0$. The forward muon system extends muon detection to $|\eta| \approx 2.0$. It uses mini drift tubes (MDTs) rather than PDTs, and includes trigger scintillation counters and beam pipe shielding.

4.2.6.1 Central muon detector

The central muon system consists of a 1.8 T toroidal magnet, drift chambers, the cosmic cap and bottom scintillation counters, and the $A\phi$ scintillation counters. The central toroid is a square annulus 109 cm thick whose inner surface is about 318 cm from the Tevatron beamline; it covers the region $|\eta| < 1$. It allowes a stand-alone muon-system momentum measurement, which *i*) enables a low-p_T cutoff in the Level 1 muon trigger, *ii*) allows for cleaner matching with central detector tracks, *iii*) rejects π/K decays, and *iv*) improves the momentum resolution for high momentum muons.

The three layers of drift chambers are located inside (A layer) and outside (B and C layers) of the central toroidal magnet. Approximately 55% of the central region is covered by three layers of PDTs; close to 90% is covered by at least two layers (Fig. 4.11). The drift chambers are large, typically 2.8×5.6 m^2, and made of rectangular extruded aluminum tubes. The PDTs outside of the magnet have three decks of drift cells, while the A layer has four decks, with the exception of the bottom A-layer PDTs, which have three decks. The cells are 10.1 cm across; typical chambers are 24 cells wide and contain 72 or 96 cells.

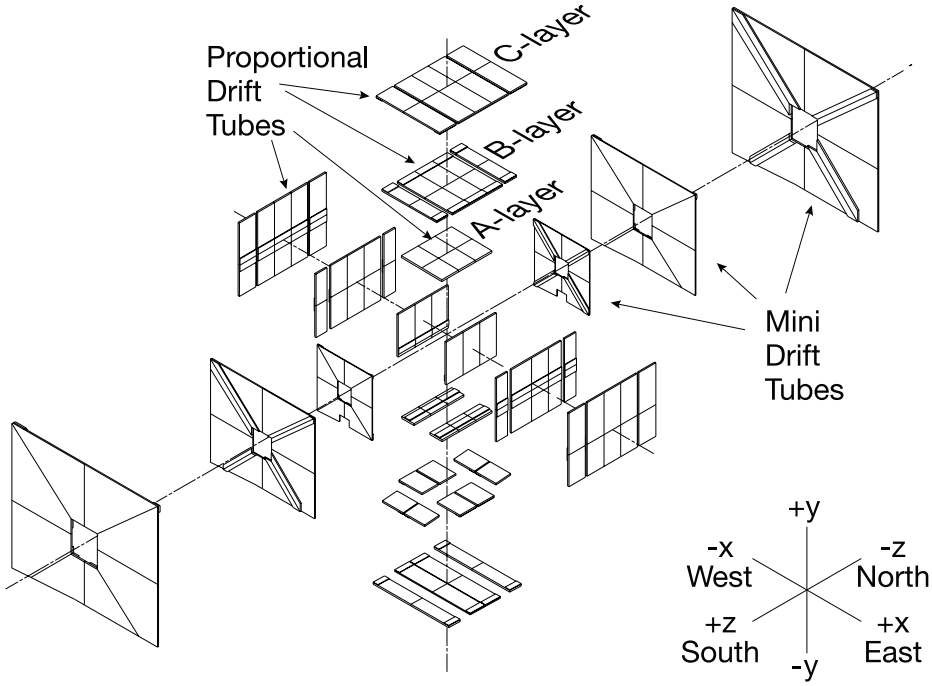

Figure 4.11: The DØ Muon System (PDT + MDT). [25]

The $A\phi$ scintillation counters cover in ϕ the A-layer PDTs, those between the calorimeter and the toroid. They provide a fast detector for triggering on and identifying muons and for rejecting out-of-time backscatter from the forward direction. Fig. 4.12 demonstrates the layout of these counters as well as the cosmic cap and bottom scintillation counters. All of them are used primarily for fast triggering and background rejection.

4.2.6.2 Forward muon detector

The forward muon detector system covers $1.0 < |\eta| < 2.0$ and consists of four major parts: the end toroidal magnets, three layers of MDTs for muon track reconstruction, three layers of scintillation counters for triggering on events with muons, and shielding around the beam pipe. The magnets and counters are described above; specific to the forward muon system are the Mini Drift Tubes (MDT). Mini drift tubes were chosen for their short electron drift time (below 132 ns), good coordinate resolution (less than 1 mm),

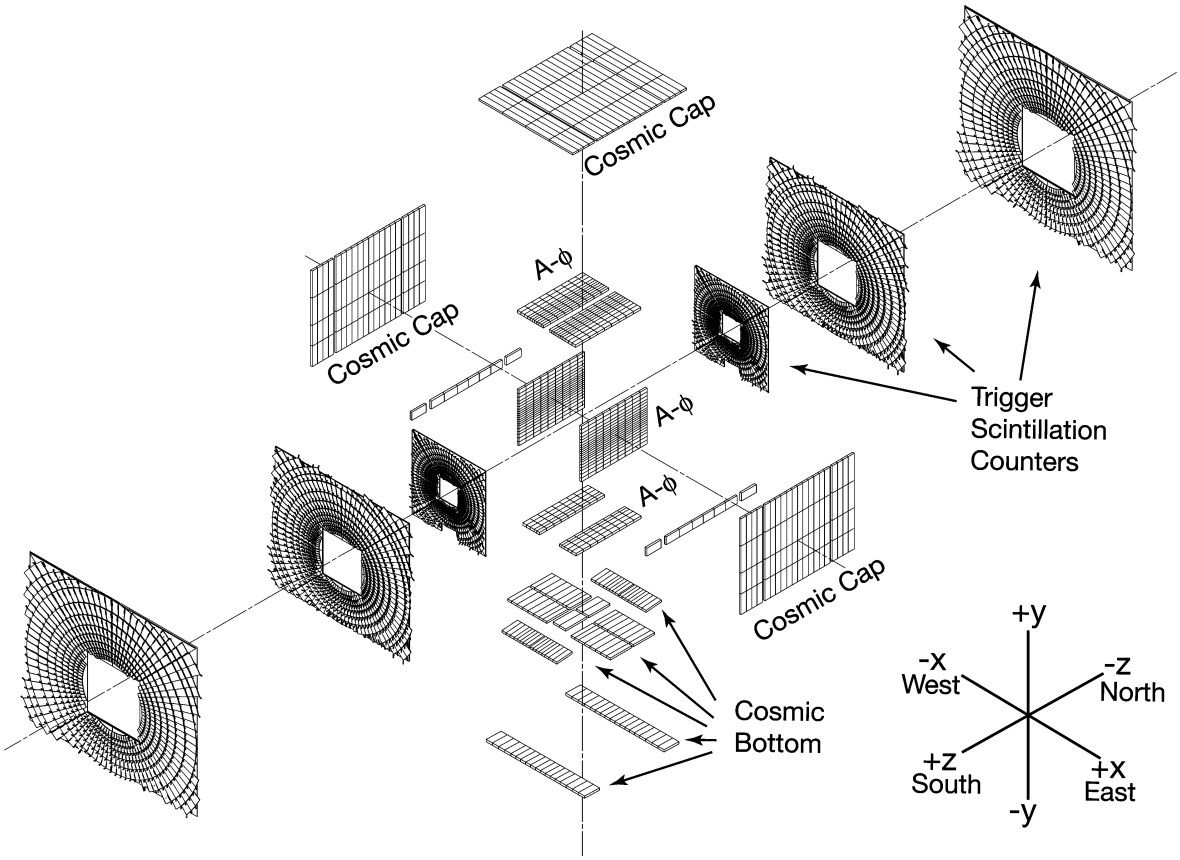

Figure 4.12: The DØ Muon System (Scintillators) [25]

radiation hardness, high segmentation, and low occupancy. The MDTs are arranged in three layers (A, B, and C, with A closest to the interaction region inside the toroidal magnet and C furthest away), each of which is divided into eight octants, as illustrated in Fig. 4.11. Each layer consists of three (layers B and C) or four (layer A) planes of tubes mounted along magnetic field lines. The entire MDT system contains 48,640 wires.

4.2.7 The DØ Trigger System

Three distinct levels form the DØ trigger system, with each succeeding level examining fewer events but in greater detail and with more complexity. The first stage (Level 1 or L1) comprises a collection of hardware trigger elements that provide a trigger accept rate of

about 2 kHz. In the second stage (Level 2 or L2), hardware engines and embedded microprocessors associated with specific subdetectors provide information to a global processor to construct a trigger decision based on individual objects as well as object correlations. The L2 system reduces the trigger rate by a factor of about two and has an accept rate of approximately 1 kHz. Candidates passed by L1 and L2 are sent to a farm of Level 3 (L3) microprocessors; sophisticated algorithms reduce the rate to about 50 Hz and these events are recorded for offline reconstruction. An overview of the DØ trigger and data acquisition system is shown in Fig. 4.13. A block diagram of the L1 and L2 trigger systems is shown in Fig. 4.14.

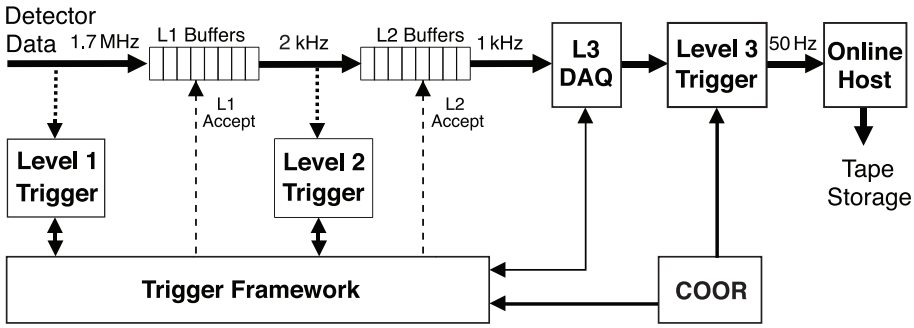

Figure 4.13: Overview of the DØ trigger and data acquisition systems.[25]

4.2.8 Luminosity determination

The luminosity $\mathcal{L}$ is determined from the average number of inelastic collisions per beam crossing $\bar{N}_{LM}$ measured by the Luminosity Monitor (LM) [29]: $\mathcal{L} = \frac{f\bar{N}_{LM}}{\sigma_{LM}}$ where f is the beam crossing frequency and σ_{LM} is the effective cross section for the LM that takes into account the acceptance and efficiency of the LM detector. Since $\bar{N}_{LM}$ is typically greater than one, it is important to account for multiple $p\bar{p}$ collisions in a single beam crossing. This is done by counting the fraction of beam crossings with no collisions and using Poisson statistics to determine $\bar{N}_{LM}$.

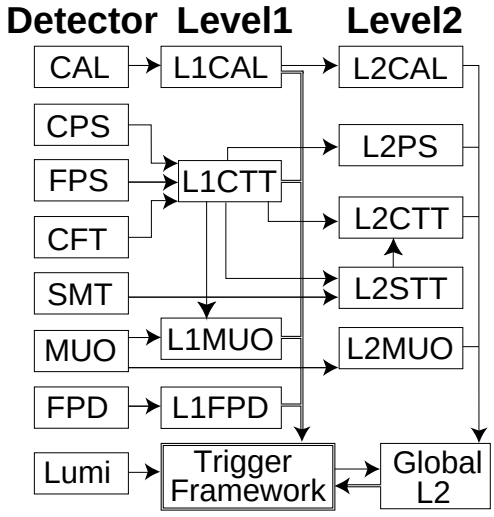

Figure 4.14: Block diagram of the DØ L1 and L2 trigger systems. The arrows show the flow of trigger-related data. [25]

CHAPTER 5

EVENT RECONSTRUCTION AND OBJECT ID

The data recorded by different detector components do not translate trivially into physically meaningful objects. The measured calorimeter cell signals, muon and central tracker hits have to be interpreted as jets, electrons, photons, muons and τ leptons with properties as close to reality as possible. This is the task of event reconstruction, which is handled on DØ by software package called DØRECO. It is a very CPU-intensive program that processes real collision events as well as simulated (Monte Carlo) events. The executable is run offline on production farms and the results are placed into the central data storage system [30] for further analysis.

5.1 Track and Vertex Reconstruction

The CFT and SMT detectors are both used in determination of the charged tracks in the detector. Tracks are fit to the hits in in these subsystems. Several different algorithms have been developed by DØ for this purpose. The most widely used is the Global TRacking (GTR) algorithm, which uses a Kalman fitter method [31] .

The GTR track finding algorithm involves several steps:

- Building the surfaces that model the shape of tracking detectors (cylinder for CFT and plane for SMT).
- Defining paths (ordered lists of surfaces that the particle would cross with associated uncertainties).

- Propagators are used to extrapolate the "seed" tracks across the surfaces.
- Fitters attempt to associate clusters to tracks at each surface crossing.
- Filter algorithms are used to reject the candidate tracks that share too many clusters, missed 2 or more surfaces, and so forth.

The tracks are defined by the list of surfaces crossed and the track parameters at each surface. Normally six parameters are needed: three position coordinates, two direction parameters and a curvature. However, when bound to a surface, one parameter is fixed and a track has five free parameters. The form of the parameters depends on the type of surface (Fig. 5.1).

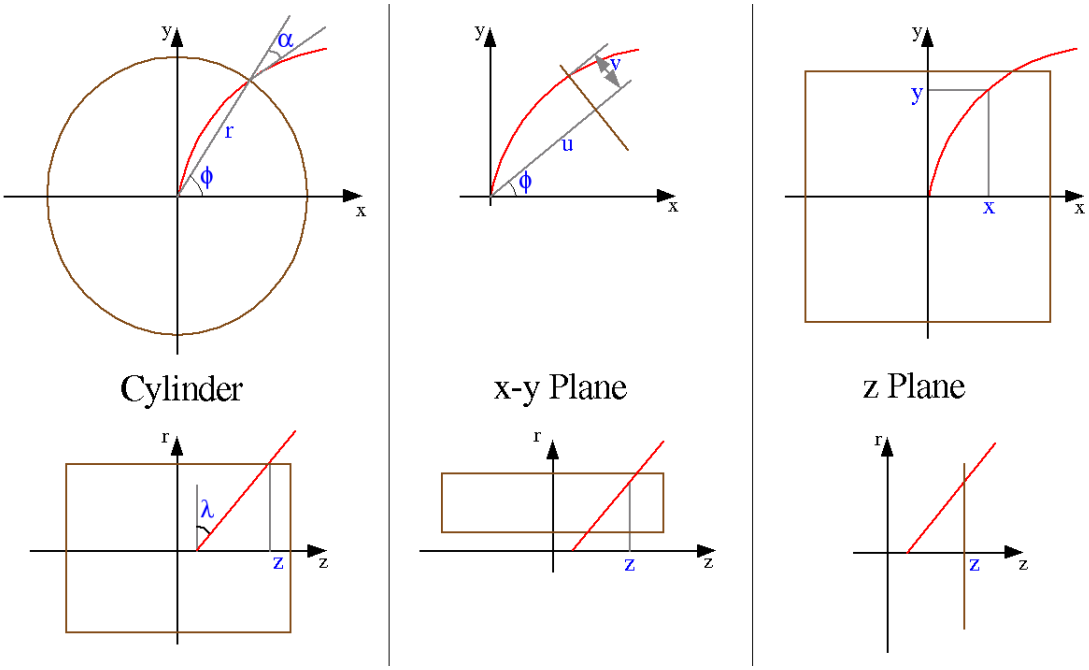

Figure 5.1: The track parameters used in GTR. The track is shown in red, with the surface in brown and track parameters in blue.

The reconstructed tracks are then propagated outside of the tracker volume in order to associate tracks with jets, electrons and muons. This is done in a similar fashion to the track reconstruction - additional surfaces are built to represent the calorimeter and muon system and propagators are used for track extrapolation.

Tracks are also used to reconstruct the primary and secondary interaction vertices of an event [32]. This involves both track filtering (determing which tracks are likely to belong to a primary vertex, which to a secondary and which are just fakes) and track fitting (minimizing χ^2 of the tracks fitted to a single vertex location).

Secondary vertices are used for b-jet ID (section 5.7).

5.2 Jet Reconstruction

Unlike tracks and muons, jets do not contain a single particle. Instead, a jet is the result of a complex cascade shower in the calorimeter, usually originated by an initial parton. For this reason jet reconstruction is somewhat an ambiguous procedure. Particles in the shower are not guaranteed to fly *exactly* in the same direction, so the ΔR "width" of a jet cone is not a fixed value. In fact, DØ uses jets defined with two cone sizes - 0.5 and 0.7. For the purpose of this analysis 0.5 jets are used, which were found to be more suitable for top quark physics. For the τ ID 0.3 cones are used (section 5.6).

The cone reconstruction algorithm follows the following scheme [33]. The cells in the calorimeter are grouped in towers as described in section 4.2.5. These towers are transformed into detector towers by removing cells whose energy deposit is less than 2.5σ of the measured electronics (or pedestal) noise level or otherwise fail data quality criteria. Reconstructed towers with energy above the predefined threshold (0.5 GeV at DØ) form the "seeds" of the jet cones. Next, all cells within ΔR of the seed are added to the forming "protocluster." If the centroid (E-weighted mean) of the protojet is more than 0.001 away in R from the starting position, then the process is repeated. A p_T threshold of 8 GeV is finally applied to the reconstructed jets.

5.3 Missing Transverse Energy

Calculation of the missing transverse energy ($\not\!\!E_T$) can be done on the reconstruction level calorimeter towers or directly on cells [34]. In either case the visible E_T of the objects are summed:

$$E_{Tx} = \sum_{i=1}^{n} E_{Ti} \cos\phi_i$$

$$E_{Ty} = \sum_{i=1}^{n} E_{Ti} \sin\phi_i$$

If there was no missing energy these would have to be 0, so $\not\!\!E_{Tx} = -E_{Tx}$ and $\not\!\!E_{Ty} = -E_{Ty}$. Hence:

$$\not\!\!E_T = \sqrt{(\not\!\!E_{Tx})^2 + (\not\!\!E_{Ty})^2}$$

This quantity has to be adjusted for Jet Energy Scale (JES) and muons, since the latter carry energy beyond the calorimeter. $\not\!\!E_T$ is the only evidence of neutrinos in an event since on their own they leave no trace in the detector.

5.4 Electromagnetic (EM) particle Identification

As discussed in section 4.2.5 the DØ calorimeter has excellent compensation with $e/h \approx 1$. This means that EM objects (electrons and photons) would evoke the same energy response as jets. Therefore EM ID can use a simple cone clustering algorithm nearly identical to one used for jet ID. 0.2 cone calorimeter objects are then used as a starting point of EM ID.

The task of EM ID is to identify which of these are in fact EM objects and which are not. This is a pattern recognition problem and is solved by examining the properties

which are different for hadronic and EM showers. One such variable is EM isolation. An electromagnetic shower is much narrower than a hadronic one and develops in the first (electromagnetic) layers of the calorimeter. This should be reflected in energy profile in $\eta - \phi$ space:

$$iso = \frac{E_{tot}(0.4) - E_{EM}(0.2)}{E_{EM}(0.2)},$$

where $E_{tot}(0.4)$ is the total calorimeter energy deposited in the 0.4 cone around the jet and $E_{EM}(0.2)$ is the energy deposited in the 0.2 cone in the electromagnetic layers only.

Additional discriminating variables used in EM ID are EM energy fraction and EM likelihood (defined using a covariance matrix method). All of this provides very efficient ID with low fake rate, as can be seen in [35].

5.5 Muon Identification

Reconstructed muon candidates are classified using two parameters: muon type and muon quality. The type of muon is given by the parameter *nseg* [36]. A positive value of nseg indicates that the muon reconstructed in the muon system was matched to a track in the central tracking system (by the track extrapolation procedure explained in section 5.1). For such muons the momentum of the track is used for the muon because the central tracker has much better p_T resolution then the muon system. A negative value of nseg tells that the local muon could not be matched to a central track. The absolute value —nseg— = 1, 2, or 3, respectively and indicates that the local muon is made up of A-layer only hits, B or C-layer only hits (outside the toroid), or both A- and B- or C-layer hits.

The second parameter used to classify muons is the quality. The muon quality can be *loose*, *medium* or *tight*. *Tight* muons must have nseg = 3 and requires

- at least two A layer wire hits

- at least one A layer scintillator hit
- at least three BC layer wire hits
- at least one BC scintillator hit
- a converged local fit

medium drops the fit requirement and *loose* allows one more of these conditions to fail. For nseg < 3 appropriate hit requirements are dropped for *medium* and *loose* muon candidates.

5.6 τ ID

5.6.1 Tau decay modes

The τ lepton has several decay channels, classified by the number and flavor of neutral and charged particles in its decay [11] :

- electron or muon ($\tau \rightarrow e\nu_e\nu_\tau$ or $\tau \rightarrow \mu\nu_\mu\nu_\tau$), BR = 35%
- charged hadron ($\tau \rightarrow \pi^-\nu_\tau$), BR =12%
- charged hadron + ≥ 1 neutral hadrons (i.e. $\tau \rightarrow \rho^-\nu_\tau \rightarrow n\pi^0 + \pi^-\nu_\tau$) , BR = 38%
- 3 charged hadrons + ≥ 0 neutral hadrons, BR = 15% (so-called "3-prong" decays)

5.6.2 Tau ID variables

The leptonic decay modes are impossible to distinguish from leptons that are not from τ decays. At D0 τs are identified in their hadronic modes (contributing to inefficiency

of τ ID) as narrow (R=0.3 cone) calorimeter showers, isolated and matched to a charged track. The most important discriminating variables are [37]:

- Profile - $\frac{E_T^1+E_T^2}{\sum_i E_T^i}$, where E_T^i is the E_T of the ith highest E_T tower in the cluster.
- Isolation, defined as $\frac{E(0.5)-E(0.3)}{E(0.3)}$, where $E(R)$ is the energy contained in a cone of radius R around the calorimeter cluster centroid.
- Track isolation, defined as $\sum p_T$ of non-τ tracks in a cone of R=0.5 around the calorimeter cluster centroid.

Using these and other variables, two artificial neural networks (NN) are trained to identify three types of τ (π-type, ρ-type and 3-prong).

The output of these NNs provides a set of 3 variables (nnout 1 ... 3) to be used to select a τ in the event. The NN outputs, nnout, are normalized to lie between 0 and 1. The NN are so trained as to give a high nnout for a real τ, and a low value for other objects, such as jets [37].

5.6.3 Energy scale

Most of the objects (electrons, photons and jets) reconstructed by the DØ detector have measured energy different from that of the corresponding particle (quark, photon or electron). The process of scaling the reconstructed object energy to the correct value is called "energy scale." Even more then the energy scale correction itself is the difference between ES in data and MC simulation. It is important to determine whether such a correction is necessary for τ candidates. In [38] the process $Z \rightarrow \tau\tau$ had been studied. In particular, Fig. 4 of that work demonstrates an excellent agreement between the data and $Z \rightarrow \tau\tau$ MC in the distribution of the invariant mass of the τ pair. Figure 15 of [39] shows other important properties (p_T of τ and $\not\!\!E_T$), which also agree very well. Since no

energy correction had been applied to the τ in this work, one can conclude that we can take the energy scale of τ ID to be 1.

5.6.4 Performance

The τ NN had been trained and optimized for low jet multiplicity events (i.e. $Z \rightarrow \tau\tau$). We wanted to compare its performance for the high multiplicity signal (top) that is the subject of this dissertation (Chapter 6).

In order to evaluate the ID efficiency reliably one has to match the reconstructed τ candidate with the true τ from MC. We start with all the τ candidates in an event, regardless of the NN output. We then want to select those that can be with high confidence associated with real τ leptons. The assumption is that those τ candidates whose energy and direction matched to the visible component of a τ lepton decay products are indeed representing the detector signature of this particle. We can then determine how well our τ identification algorithm fares in finding this τ lepton. Figure 5.2 illustrates the matching procedure - the τ candidates with ΔR ¡ 0.05 from a real MC τ and ΔP ¡ 10 GeV are deemed to be the "real" matched τ.

For such τ we plotted the NN for different τ types (Fig 5.3). From these one can determine the efficiency of τ ID for various cuts on NN (Fig 5.4).

In order to choose the best cut on τ NN one has to also consider the fake rate (the number of non-tau objects passing the tau identification requirements, henceforth refered to as "fakes"). For this purpose we had examined the τ candidates in the preselected ALLJET data sample (the details of preselection are described in section 8.2). Since this data sample is QCD-dominated (expected contribution from electroweak processes is less than 0.2%) it's safe to ignore the presence of real taus in this sample and assume all τ in it to be fake (this assumption will be employed again for our QCD background estimation in section 8.4). Figure 5.5 shows the distribution of NN for the τ. From this we can

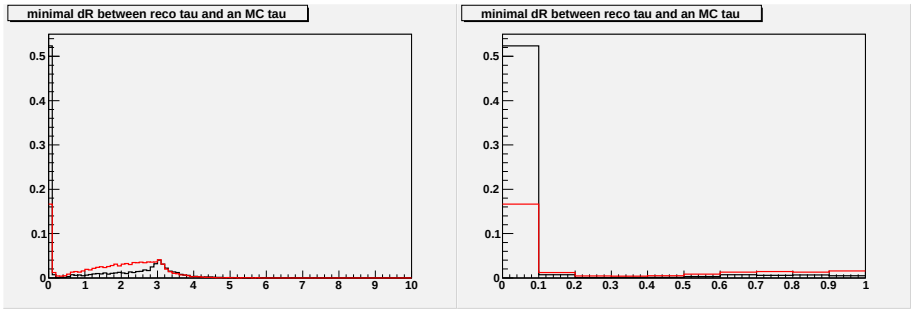

(a) ΔR between reco τ and MC τ

(b) ΔR between reco τ and MC τ (a close-up of low values)

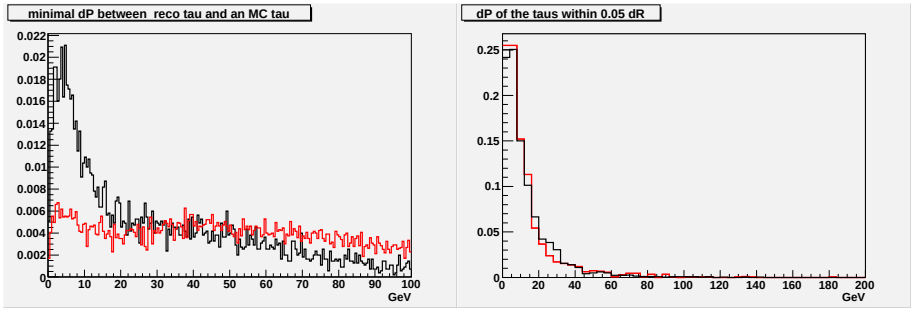

(c) Difference in energy between reco and MC τ

(d) Difference in energy between MC and reco τ that were matched in angle

Figure 5.2: Matching of MC τ and reco τ. Black is $Z \rightarrow \tau\tau$, red is $t\bar{t} \rightarrow \tau + jets$. The histograms are normalized to 1 for easy comparison.

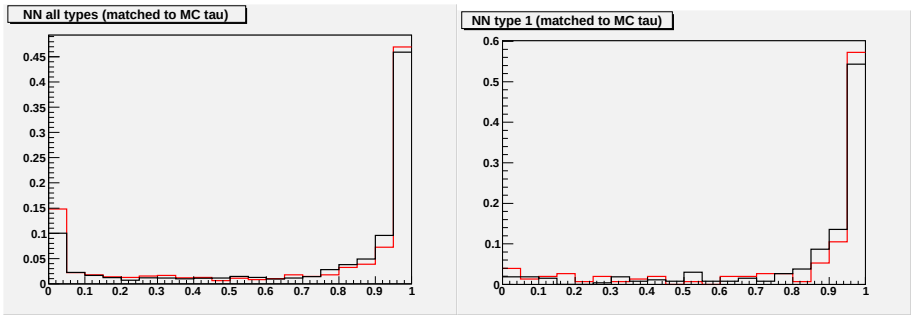

(a) NN output for ALL types (b) NN for type 1

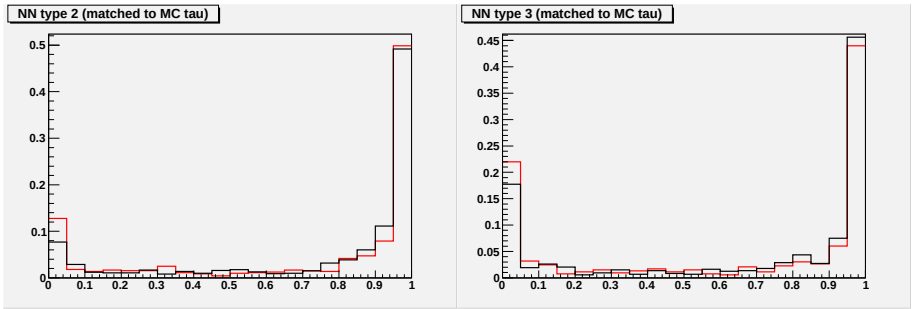

(c) NN output type 2 (d) NN for type 3

Figure 5.3: NN for matched τ. Black is $Z \rightarrow \tau\tau$, red is $t\bar{t} \rightarrow \tau + jets$. The histograms are normalized to 1 to enable comparison.

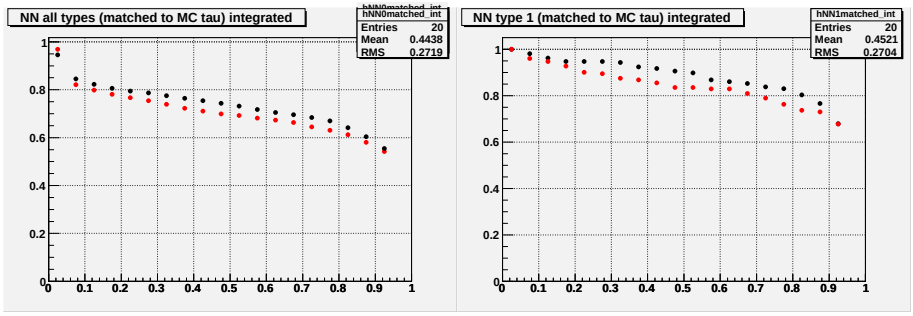

(a) ALL types (b) Type 1

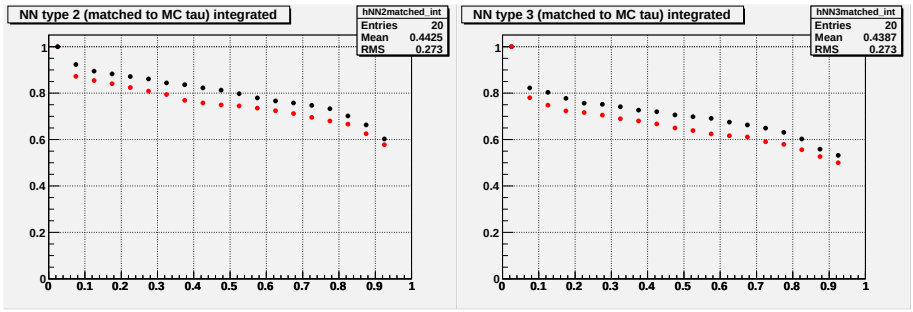

(c) Type 2 (d) Type 3

Figure 5.4: τ ID Efficiencies for different types. Black is $Z \rightarrow \tau\tau$, red is $t\bar{t} \rightarrow \tau + jets$.

determine the the fake rate as a function of NN output (Fig 5.6). Type 3 has a noticeably higher fake rate. This is to be expected, since most jets have higher track multiplicities than type 1 and 2 τ, making it harder for them to pass τ ID requirements.

Figure 5.7 shows the fake rate vs. efficiency of the τ ID for our channel. From this we can select the optimal selection cut on τ NN, based on the τ ID significance, defined as $\frac{Number\ of\ real\ taus}{\sqrt{Number\ of\ real + Number\ fakes}}$ (Fig 5.8). It is computed on our preselected analysis data set (section 8.2).

We conclude that the τ ID efficiences for $t\bar{t}$ events are about the same as those for $Z \rightarrow \tau\tau$ events. The optimal cut for our purpose is NNout>0.95 for all tau types.

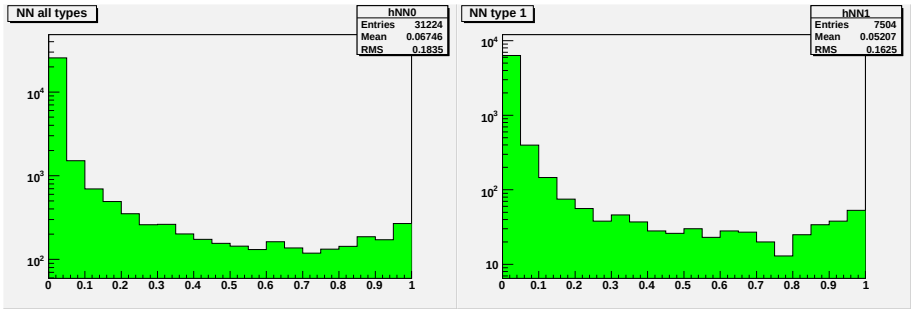

(a) NN for ALL types

(b) NN output for type 1

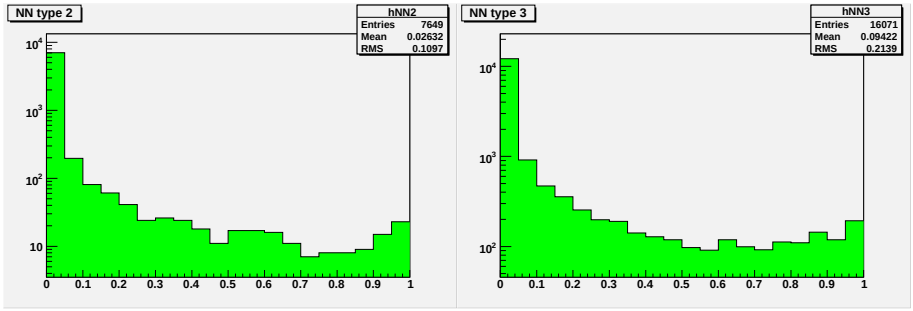

(c) NN type 2

(d) NN output for type 3

Figure 5.5: NN output for fake τ.

5.7 b tagging

We use the Secondary Vertex Tagger (SVT) [40] algorithm to tag jets originating from B hadrons. It is characterized by high (compared to other taggers) purity, which is essential for such a QCD-dominated channel as ours.

The algorithm reconstructs secondary vertices inside a jet, using the jet's associated tracks. The tracks are also required to pass a set of cuts outlined in Table 5.1. Then, the decay length significance is computed. If the jet has this significance $>$ than 7 (for SVT TIGHT) it is considered b tagged.

As can be seen from Figs. 5.9 and 5.10, the TIGHT cut is most appropriate for our signal.

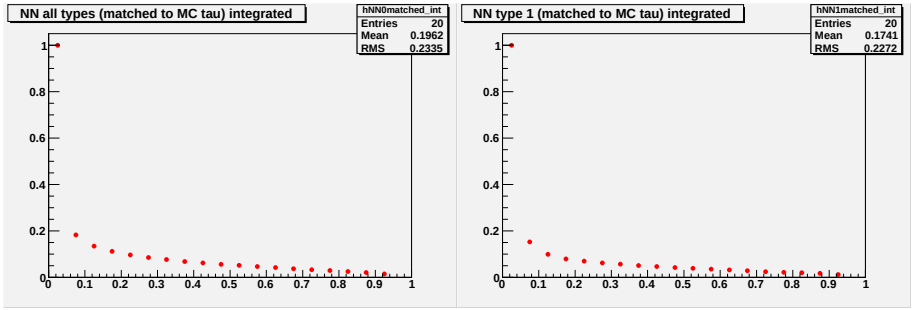

(a) ALL types (b) Type 1

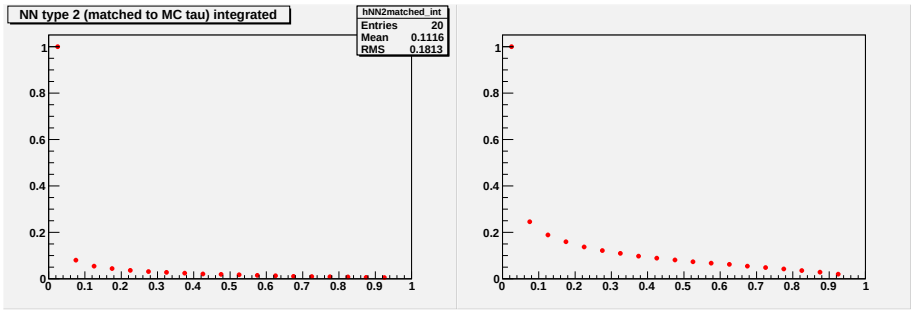

(c) Type 2 (d) Type 3

Figure 5.6: τ ID fake rate for different types.

Table 5.1: The standard cuts on SVT [40].

SVT			
	LOOSE	MEDIUM	TIGHT
Number of SMT hits	2	2	2
min p_T of tracks	1 GeV	1 GeV	1 GeV
min impact parameter significance of tracks	3	3.5	3.5
min track χ^2	10	10	10
max vertex χ^2	100	100	100
min vertex collinearity	0.9	0.9	0.9
max vertex decay length	2.6 cm	2.6 cm	2.6 cm
min decay length significance	5	6	7

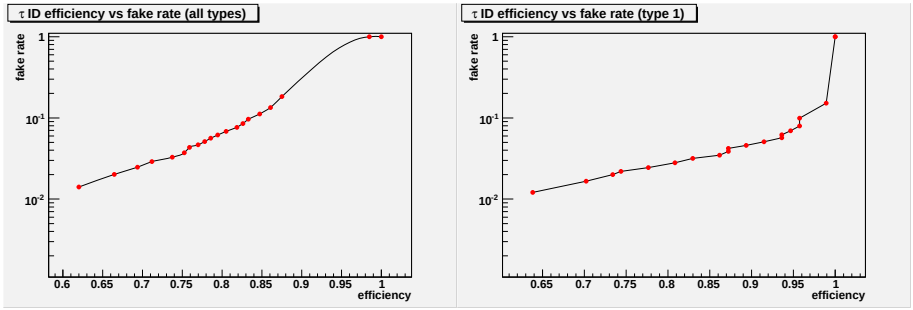

(a) ALL types

(b) Type 1

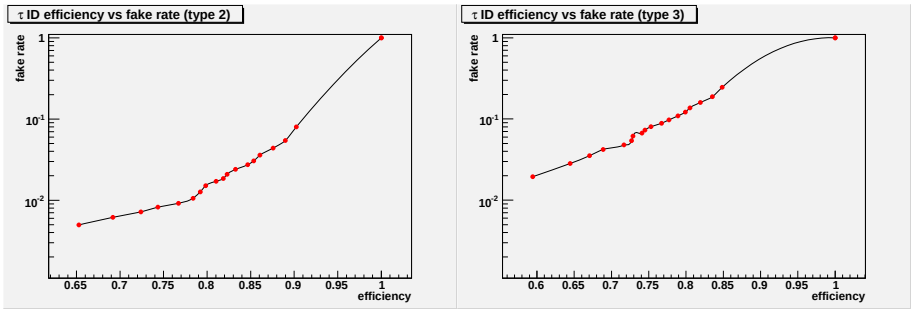

(c) Type 2

(d) Type 3

Figure 5.7: τ ID efficiency vs. the fake rate. Type 2 is the cleanest; type 3 has the highest fake rate, as expected.

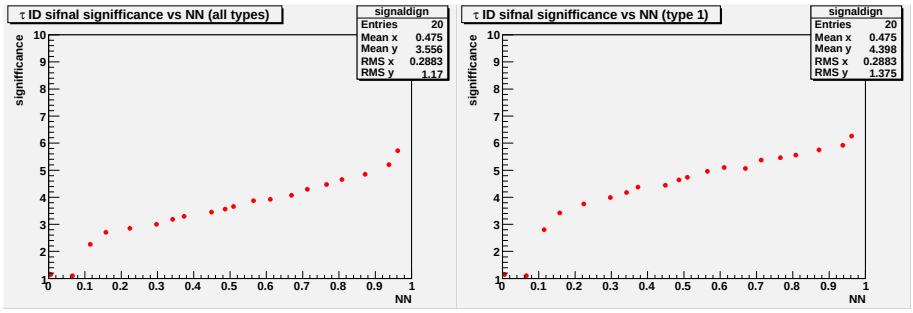

(a) ALL types (b) Type 1

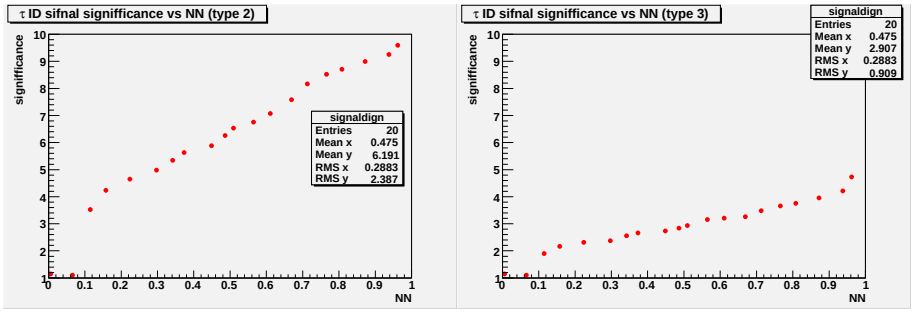

(c) Type 2 (d) Type 3

Figure 5.8: τ ID significance vs. the NN cut. The 0.95 cut appears to be advantageous for all the types.

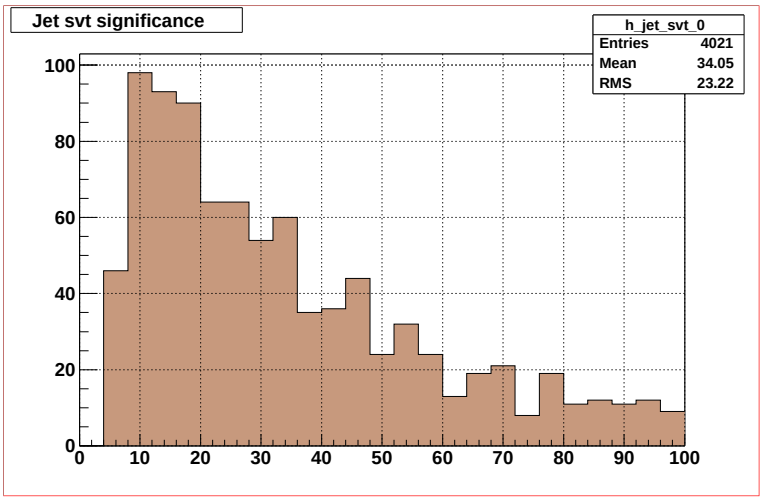

Figure 5.9: SVT decay length significance for the b jets in $t\bar{t} \rightarrow \mu + jets$ MC.

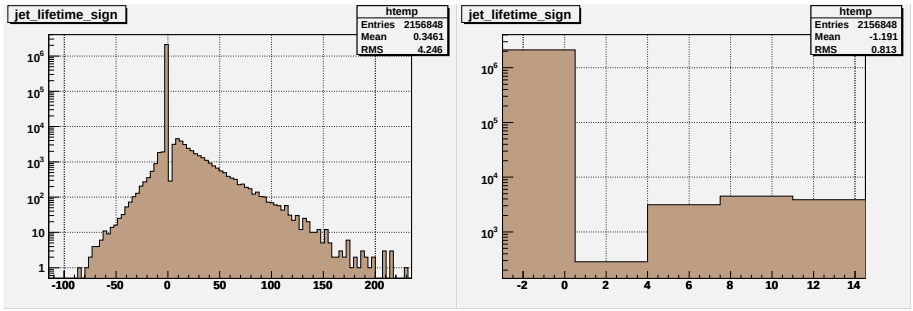

(a) SVT significance across the entire range

(b) SVT significance at values near 0

Figure 5.10: SVT decay length significance for all the jets in the ALLJET skim data.

5.7.1 Taggability

In order to reconstruct a secondary vertex in a jet, the jet must contain at least 2 tracks. If such tracks are found and their p_Ts are greater than 0.5 GeV the jet is called taggable. In MC it is important to distinguish the taggability from the tagging efficiency, since the latter depends on the jet's flavor.

5.7.2 b tagging efficiency

It is known that b tagging applied directly to MC gives an overestimated efficiency. In order to account for this, the SVT is parametrized on $t\bar{t} \rightarrow \mu + jets$ MC and $\mu + jets$ data to compute the correction factor, which has to be applied to MC. As result we obtain the MC tagging probability and the data corrected one (Fig. 5.11). The data corrected efficiency is indeed noticeably (>30%) lower than what we get by applying SVT directly to MC.

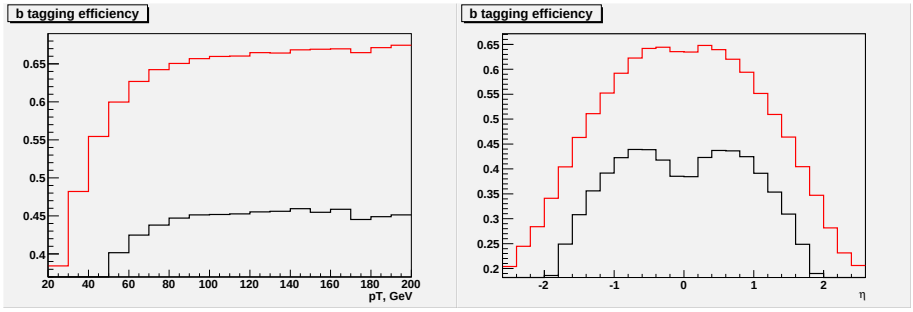

(a) SVT efficiency (b) SVT efficiency

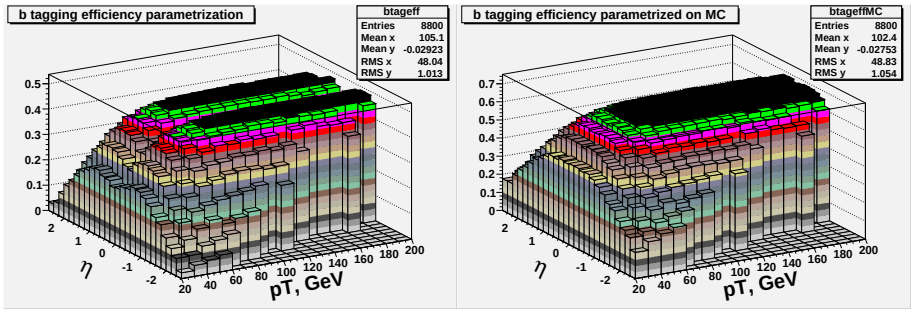

(c) SVT efficiency parameterized on data (d) SVT efficiency parameterized on MC

Figure 5.11: SVT Efficiency for $t\bar{t} \rightarrow \tau + jets$ MC. Red is MC parameterization; black is data-corrected. Flavor dependence is taken into account. The lower plots show 2D parameterizations.

5.7.3 c tagging efficiency

An assumption is made that the correction factor obtained by dividing the semi-leptonic b tagging efficiency in data to the one in MC is also correct for c jets. Hence the MC-obtained inclusive c tagging efficiency is multiplied by this factor (and by its taggability too) in order to estimate the c tagging probability.

5.7.4 Light jet tagging efficiency

The b tag fake rate from light quarks is computed by measuring the negative tag rate. It is defined by the rate of appearance of secondary vertices with negative decay length significance. It is assumed that the light quarks have equal chances to produce a separated vertex with positive and negative decay length significance (due to finite resolution effects), while the heavy flavor jets can only produce a separated vertex with positive decay length significance. This, however, is not quite true, and a special scaling factor (SF_{hf}) is introduced to correct for the fraction of heavy flavors among the jets with the negative decay length significance. Another correction is for the presence of long-lived particles in light jets (SF_{ll}). Both factors are derived from Monte Carlo.

5.7.5 Event tagging efficiency

The tag rates and the taggability had been combined and used to predict the probability for a jet to be b tagged (b tagging weight). The final resulting per-event probability of having at least one such tag for the $t\bar{t} \rightarrow \tau + jets$ MC is plotted in Fig. 5.12.

Finally, it has to be noted that we tried to avoid the overlap between τ ID and b tagging. That is, we remove the jets that are matched to a 0.8 τ candidate within $\Delta R <$ 0.5 from being considered as b jets.

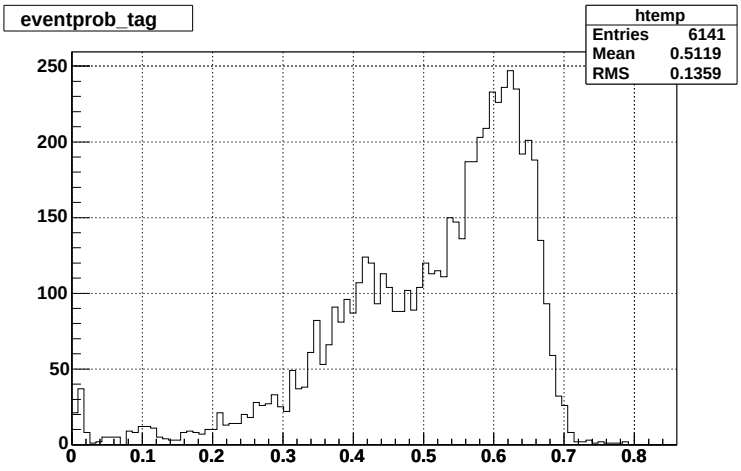

Figure 5.12: The probability to tag at least one jet with SVT for $t\bar{t} \rightarrow \tau + jets$ MC.

CHAPTER 6

$T\bar{T} \to \tau + JETS$ SIGNAL SIMULATION AND CHARACTERISTICS

Before describing the strategy of measuring $\sigma(p\bar{p} \to t\bar{t})$ in $\tau + jets$ channel we want to examine the properties of this signal and identify its most significant features. This allows us to identify the important variables and devise the selection criteria on them that would maximize the signal and minimize the background.

For this purpose we used MC simulated samples (∼10K events each) generated with ALPGEN [41] interfaced to Pythia [42] for showering and fragmentation. The event reconstruction described in Chapter 5 was run on these Monte Carlo samples.

6.1 Parton level MC

6.1.1 $t\bar{t}$

The most important MC sample is of course the top quark itself. Therefore we will start by examining its properties. Figure 6.1 shows the η, ϕ and p_T distributions.

6.1.2 τ and $\not\!\!E_T$

Unlike e and μ, a τ lepton decays well before reaching any detector element. The presence of one or more neutrinos in the decay contributes to the $\not\!\!E_T$ of the event while the visible daughters carry only a fraction of the parent tau's momentum. For this reason

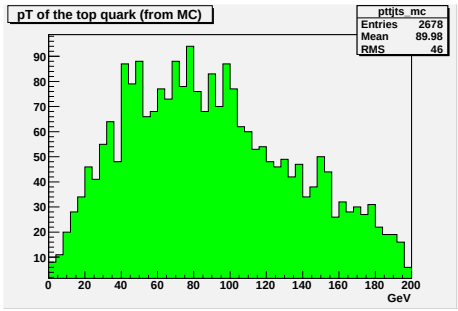

(a) p_T of t quarks

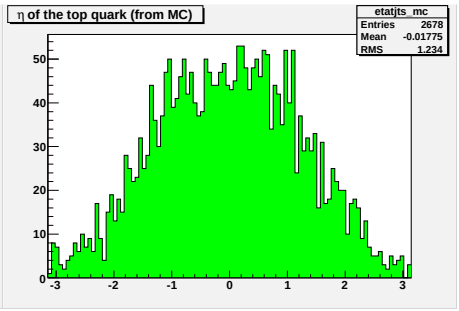

(b) η of t quarks

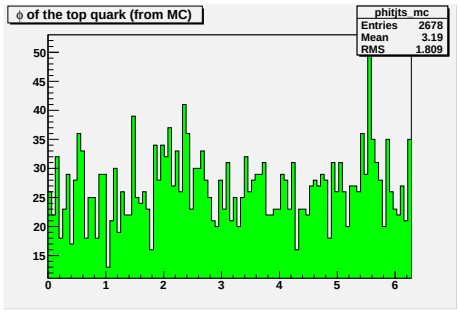

(c) ϕ of t quarks

Figure 6.1: Properties of t quarks at the parton level in signal MC sample, $p_T > 15$ GeV.

the τ available for measurement is not the same as physical τ produced. Figure 6.2 demonstrates how a sizable fraction of τ momentum (shown in 6.2e) goes missing. The plots of τ properties (p_T, η and transverse mass with $\not\!\!E_T$) are also shown in Figure 6.2.

This is to be compared with the $e + jets$ channel (Fig. 6.3). As one can observe, the "total" τ leptons behave very similarly to electrons, as of course expected. However, after taking into account the lost part of the τ energy the situation becomes very different.

6.1.3 Quarks

b quarks are shown in Fig. 6.4 while the products of W decay are shown in Fig. 6.5. This, however, doesn't account for all the jets that will be reconstructed. Distributions of first and second generation quarks and gluons from initial and final state radiation are shown in Fig. 6.6.

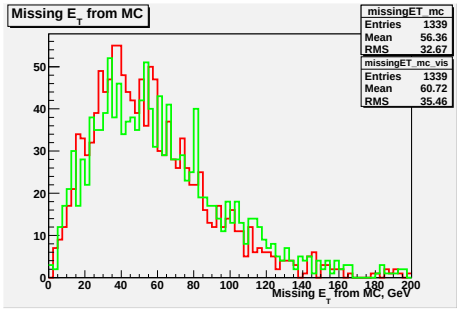

(a) Parton level $\not{E}_T$ for the signal MC (red is total, green is visible)

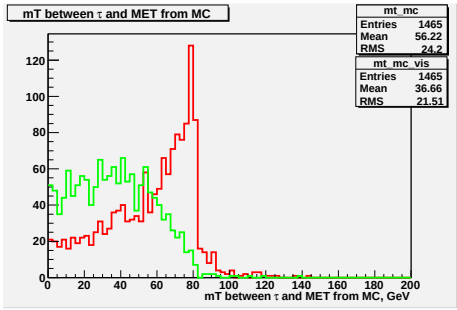

(b) mT (transverse mass) of MC τ and $\not{E}_T$ (red is total, green is visible)

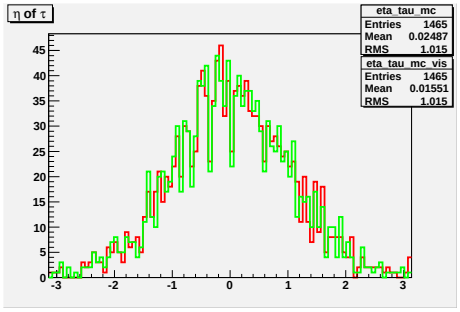

(c) η of the MC τ in signal MC (red is total, green is visible)

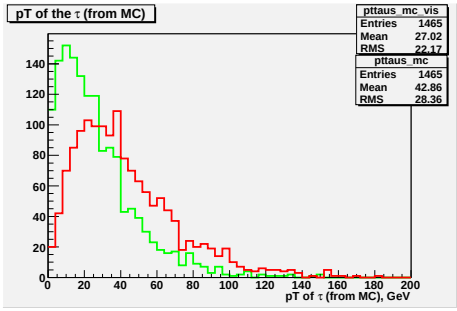

(d) p_T of the MC τ in signal MC (red is total, green is visible)

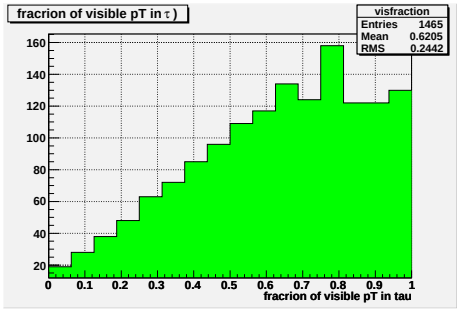

(e) visible fraction of τ energy in signal MC

Figure 6.2: Properties of $\not{E}_T$ and τ at the parton level in the signal MC sample.

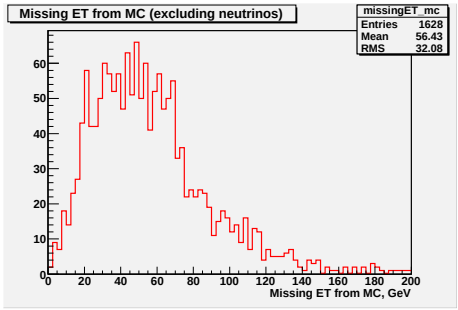

(a) Parton level $\not\!\!E_T$

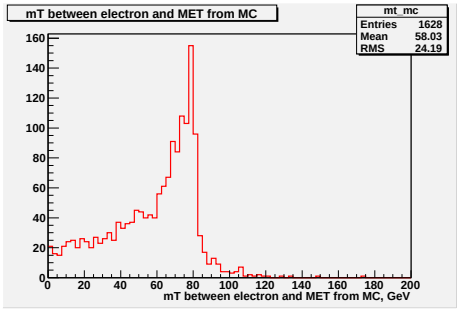

(b) mT of MC electron and $\not\!\!E_T$

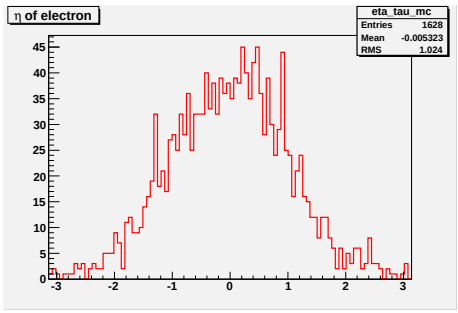

(c) η of the MC electron

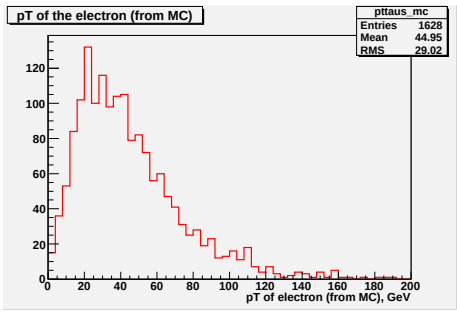

(d) p_T of the MC electron

Figure 6.3: Properties of $\not\!\!E_T$ and electron at the parton level in the $t\bar{t} \rightarrow e + jets$ MC sample.

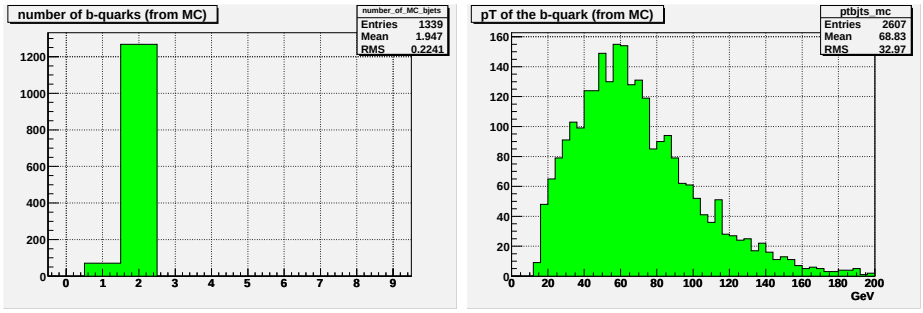

(a) Number of b quarks

(b) p_T of b quarks

(c) η of b quarks

(d) ϕ of b quarks

Figure 6.4: Properties of b quarks at the parton level in the signal MC sample, $p_T > 15$ GeV.

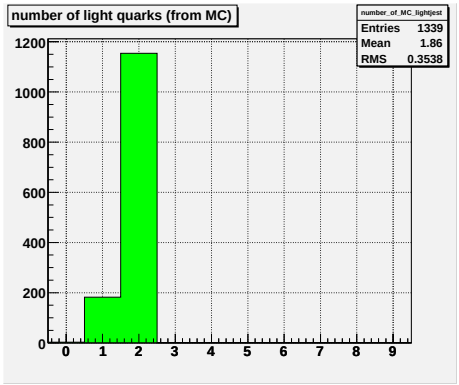

(a) Number of light quarks from the W decay

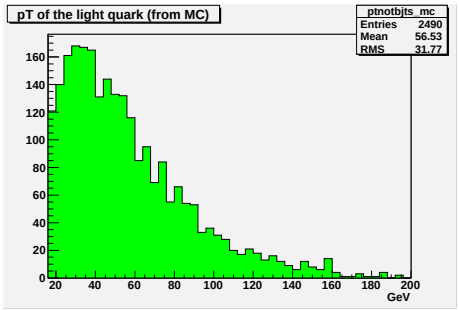

(b) p_T of light quarks from the W decay

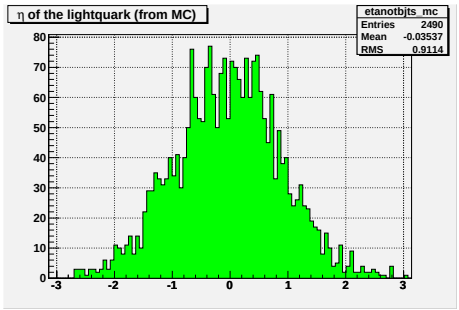

(c) η of light quarks from the W decay

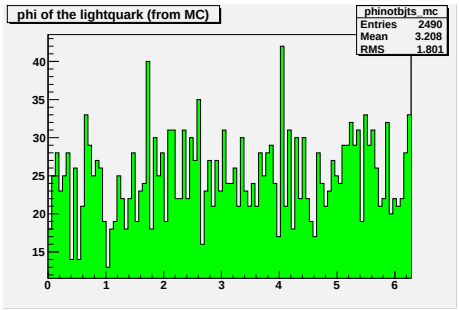

(d) ϕ of light quarks from the W decay

Figure 6.5: Properties of light quarks from W decay at the parton level in the signal MC sample, $p_T > 15$ GeV.

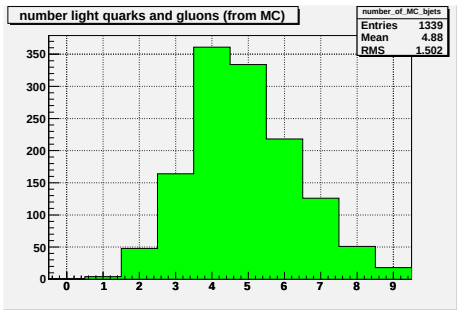

(a) Number of first and second generation quarks

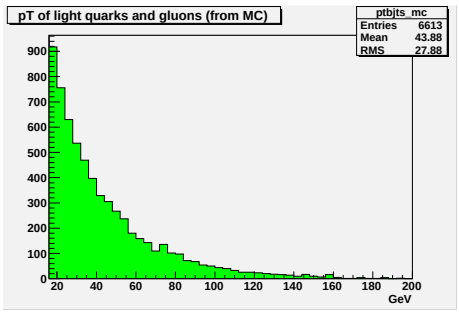

(b) p_T of first and second generation quarks

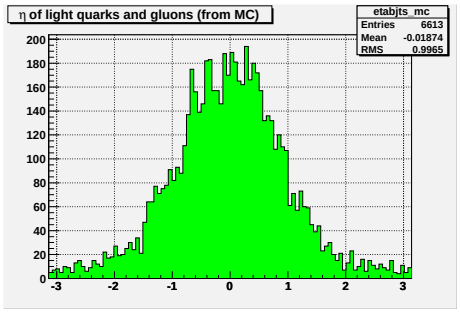

(c) η of first and second generation quarks

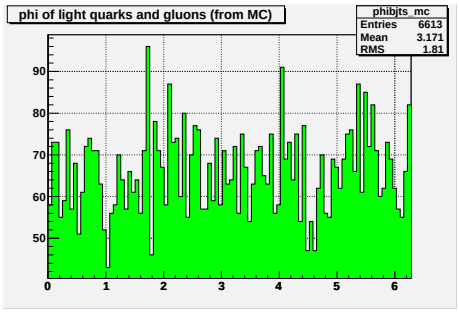

(d) ϕ of first and second generation quarks

Figure 6.6: Properties of all the light quarks and gluons in an event at the parton level in the signal MC sample, $p_T > 15$ GeV.

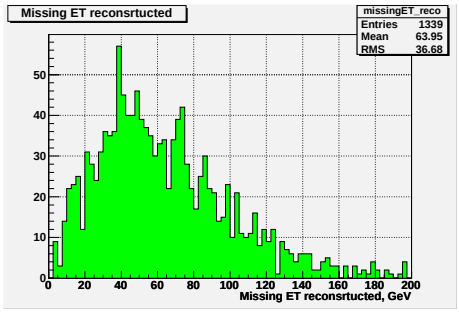

(a) Reconstructed $\not\!\!E_T$ for the signal MC

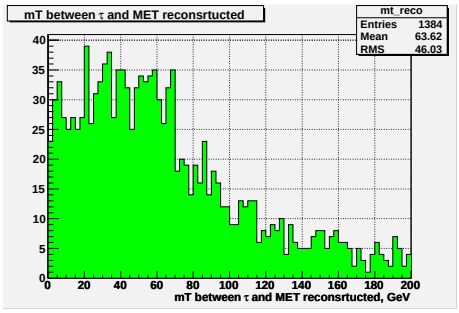

(b) mT of MC τ and $\not\!\!E_T$ reconstructed

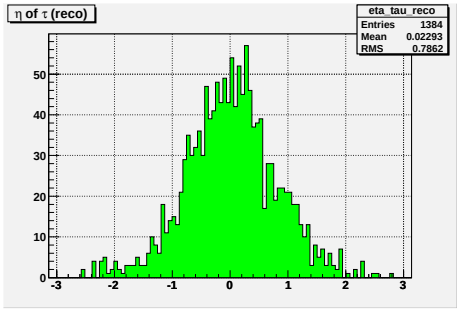

(c) η of the MC tau in signal MC reconstructed

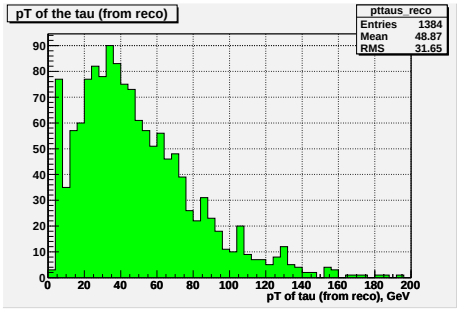

(d) p_T of the τ

Figure 6.7: Properties of detector reconstructed $\not\!\!E_T$ and τ in signal MC sample.

6.2 Detector signature (reconstructed Monte Carlo)

Now we need to find out how well our experiment observes and reconstructs this physical process. The $t\bar{t} \rightarrow \tau + jets$ Monte Carlo file was processed through the GEANT3-based simulation of the DØ Detector [43]. Taus are identified using tau ID algorithm and we apply a 0.8 cut on the τ selection neural net (section 5.6).

6.2.1 τ and $\not\!\!E_T$

We can see that for reconstructed τ's mT(of τ and $\not\!\!E_T$) (Fig. 6.7) doesn't look as good as for MC τs (Fig. 6.2). We observe a noticeable "tail" above 80 GeV.

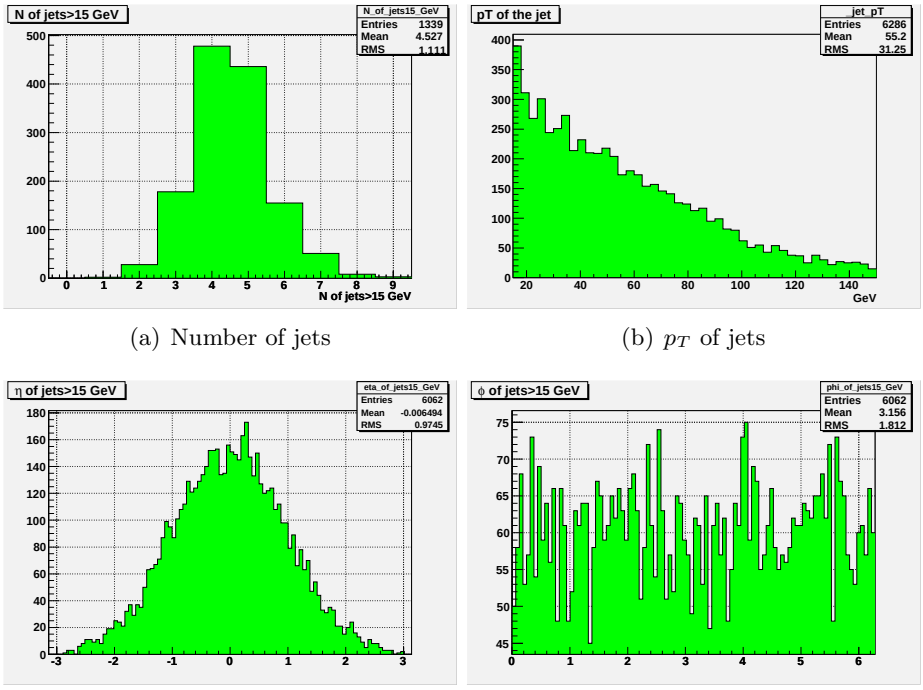

(a) Number of jets

(b) p_T of jets

(c) η of jets

(d) ϕ of jets

Figure 6.8: Properties of the jets in the signal MC sample, $p_T > 15$ GeV.

6.2.2 Jets

Before b-tagging (section 5.7) one can't separate b-jets from non-b jets, so we don't make a distinction at this point. The most important variables are the number of jets and their η and p_T distributions (Fig. 6.8).

Jets are arranged in the order of their p_T: leading (highest), sub-leading, etc. We can see in Fig. 6.8 that we typically have 4 or 5 jets in an event. It is interesting to compare the leading jet to the fourth and fifth jets (Fig. 6.9). We can see that jets after the third are very soft, as expected.

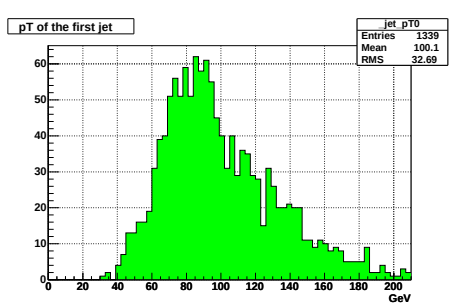

(a) 1st jet

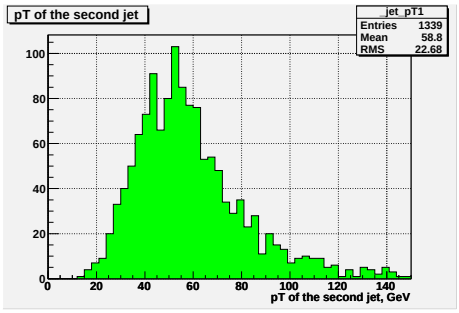

(b) 2nd jet

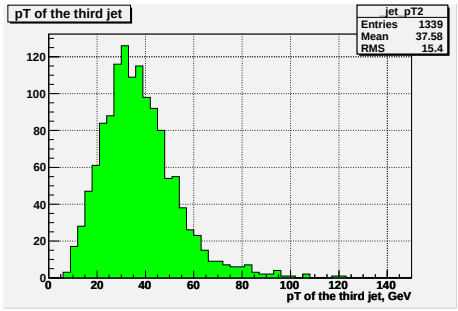

(c) 3rd jet

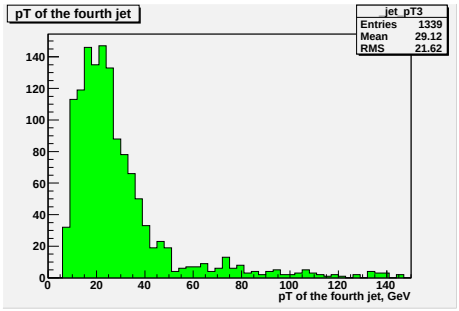

(d) 4th jet

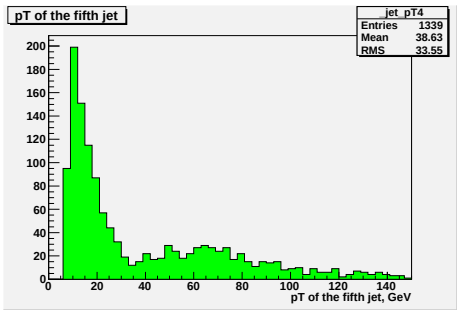

(e) 5th jet

Figure 6.9: p_T distributions for jets in the signal MC sample (including τ).

Table 6.1: Background sources, relevant for the $\tau + jets$ analysis. The branching fraction into hadronic τ has been applied.

Background	Description	Cross Section
$W + jjjj \rightarrow \tau\nu jjjj$	Has identical signature to the signal	~18 pb
$Z/\gamma + jjj \rightarrow \tau\tau jjj$	τ is usually found as a jet	~2.6 pb
$WZ \rightarrow \tau\nu jj$	needs two extra jets (can be gluon emission)	~0.2 pb
$WW \rightarrow \tau\nu jj$	needs two extra jets (can be gluon emission)	~0.5 pb
single top	small cross section, but has b-jets	~0.5 pb
QCD	Any 5-jet event, that doesn't have a real τ in it	>100 nb

6.3 Backgrounds

Two main distinctive features of the signal limit the spectrum of important backgrounds. In order to be relevant the process must have a high (>3) number of jets as well as sizable (>15 GeV) $\not\!\!E_T$. All the candidate processes are listed in Table 6.1. The cross sections listed include the branching fractions into τ.

We can conclude that two dominant background sources are QCD ("fake τ") and W+4jets. They have by far the largest cross section of all the processes in Table 6.1. These two sources are taken into account in these analyses.

CHAPTER 7

DATA COLLECTION

All events recorded by the DØ detector have to pass one of the "Global Physics Triggers." Each such trigger is a combination of specific Level 1, Level 2 and Level 3 (section 4.2.7) conditions. For this reason any physics analysis has to start by finding the most suitable set of triggers and measuring their efficiency. Also, it is necessary to know how much luminosity was collected by these triggers.

7.1 Trigger

7.1.1 Running TRIGSIM

In order to search for a signal one has to collect the data with a chosen set of triggers. We want to find such a combination so to maximize the fraction of the $t\bar{t}$ signal events written out. At the DØ experiment the processing time of the trigger system is extremely limited, forcing a limit to the set of triggers used for physics. Therefore, rather than designing a new trigger specifically for this measurement, our goal was to pick out of the set of triggers already available on the running physics trigger list. This allows us to share the dataset with other analysis groups and to make use of the data already collected with existing triggers.

To estimate trigger efficiencies the DØ trigger simulation program TRIGSIM [44] was run on the MC signal. The efficiencies for 12.30 version of the global DØ trigger definition

Table 7.1: Trigger efficiencies and overlaps between the most efficient triggers for selecting $t\bar{t} \to \tau + jets$. As one can see, 3J15_2J25_PVZ has large overlap with 4JT12, and since 4JT12 is better studied it has been chosen for this analysis.

Trigger	Fraction of events passing
4JT12	0.74±0.05
3J15_2J25_PVZ	0.73±0.05
MHT30_3CJT5	0.68±0.04
MU_JT20_L2M0	0.30±0.01
MU_JT20_L2M0 and MHT30_3CJT5	0.20±0.01
MHT30_3CJT5 and 4JT12	0.40±0.04
4JT12 and 3J15_2J25_PVZ	0.67±0.04

list are shown in Table 7.1.

The following 3 triggers give a combined efficiency of ∼85%:

MHT30_3CJT5 - $\not\!\!E_T$ trigger, requiring at least 30 GeV at level 3, which leads to ∼30% inefficiency, since our missing E_T peaks around 50 GeV.

Description: L1: At least three calorimeter trigger towers with E_T>5 GeV. L2: Require jet E_T>20. L3: Vector H_T sum >30 GeV (vector H_T sum is the transverse component of the vector sum of jet E_Ts). Additionally, one in 4000 random events is recorded and marked as "unbiased."

4JT12 - This trigger is designed for the $t\bar{t} \to jets$ analysis [14]. Does not have $\not\!\!E_T$ requirement but needs four 12 GeV jets at L3. Sizable fraction (again ∼30%) of the $t\bar{t} \to \tau + jets$ events does not satisfy this condition.

Description: L1: At least three calorimeter jet trigger towers having E_T>5 GeV. L2: Three jet candidates with E_T>8 GeV and H_T > 50 GeV. L3: Four jet candidates with $|\eta|$<3.6 and E_T>10 GeV found using a simple cone algorithm. At least three of those jets must have E_T>15 GeV. Additionally, one in 500 random events is recorded and marked as "unbiased."

MU_JT20_L2M0- Muon trigger with <20% efficiency for our signal, but it has little

overlap with others.

Description: L1: A single muon trigger based on muon scintillator and also requiring one calorimeter jet trigger tower with E_T >3 GeV. L2: At least one muon found meeting MEDIUM quality requirements but no p_T > or region requirement. Also requires at least one jet with E_T >10 GeV. L3: At least one jet with E_T >20 GeV is found using a simple cone algorithm. Additionally, one in 500 random events is recorded and marked as "unbiased."

7.1.2 Triggers in version 13

A newer trigger list collecting a part of data used in this analysis includes a number of new triggers and modifications to existing ones. Running TRIGSIM on this list we find that variants of the triggers that were best in v12 (*4JT12* and *MHT30_3CJT5*) are also most efficient in v13. In fact, an OR of just these two triggers gives an efficiency of 90±5%. The names and definitions of these triggers had changed as follows:

4JT12 became JT2_4JT12L_HT. An additional H_T cut of 120 GeV is applied.

Description: L1: Three calorimeter trigger towers with $E_T > 5$ GeV. L2: Pass events with at least three jet candidates with $E_T > 6$ GeV and H_T, formed with jets above 6 GeV, greater than 70 GeV. L3: Require at least four jets with $E_T > 12$ GeV, at least three of them with $E_T > 15$ GeV and at least two with $E_T > 25$ GeV . Event H_T calculated using all jets with $E_T > 9$ GeV must exceed 120 GeV .

MHT30_3CJT5 became JT2_MHT25_HT.

Description:: L1: Three calorimeter trigger towers with $E_T > 4$ GeV, $|\eta|$ <2.4, and two calorimeter trigger towers with $E_T > 5$ GeV. L2: Require at least three jet candidates with $E_T > 6$ GeV and H_T, formed with jets above 6 GeV, to be greater than 70 GeV L3: Vector H_T sum for the event must be above 25 GeV. Also require event scalar H_T (calculated using all jets with $E_T > 9$ GeV) to exceed 125 GeV.

7.1.3 Turn-on curves

In order to study the performance of the chosen triggers we have to determine not only the overall efficiency for the $t\bar{t} \rightarrow \tau + jets$ signal but also the fraction passed after making offline objects cut on the signal MC. For instance, it is clear that events with many high p_T jets are more likely to pass the 4JT12 trigger.

These features are reflected in the corresponding turn-on curves (efficiency of passing events with given offline object threshold) obtained using TRIGSIM. Such a curve for MHT30 and 4JT12 triggers is shown in Fig. 7.1.

7.1.4 Trigger simulation

At the time of this analysis TRIGSIM had not reached the state in which it could reliably reproduce the trigger efficiency on data. The TRIGSIM results shown in previous sections are reliable enough to base the trigger selection decision on, but the efficiencies obtained are not accurate enough to use for the cross-section measurement that is our goal. Therefore, the accepted practice is to parameterize the trigger turn-on curves using data and apply that parameterization to MC events.

Such a procedure was performed with the top_trigger package [46]. The results of a test to check the validity of this exercise is shown in Fig. 7.2 . We used the data collected by a single muon trigger (MU_JT20_L2M0). This data has little bias with respect to the 4JT10 trigger. Hence, if we count the number of the 4-jet events that passed 4JT10 and compare it with the top_trigger prediction for the same events, then that serves as a validation of top_trigger. As seen in Fig. 7.2, the agreement is fairly good, especially in the region of interest to this analysis (we require jets to have $p_T > 20$ GeV). The efficiency turn-on curve, produced by top_trigger, shown in Fig. 7.3, is found to be in agreement with the TRIGSIM prediction shown in Fig. 7.1.

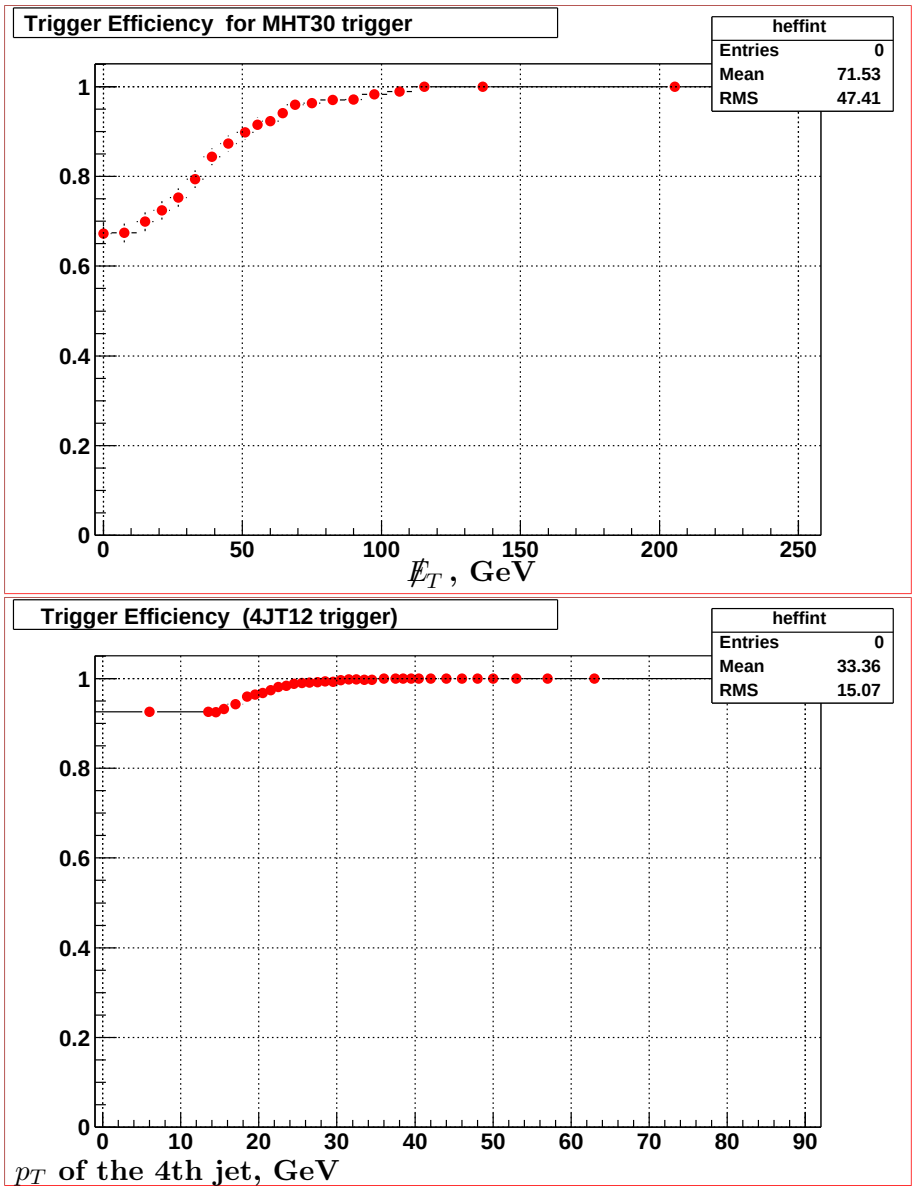

Figure 7.1: Trigger efficiency for MHT30 and 4JT12 triggers for the $t\bar{t} \rightarrow \tau + jets$ MC, obtained using TRIGSIM.

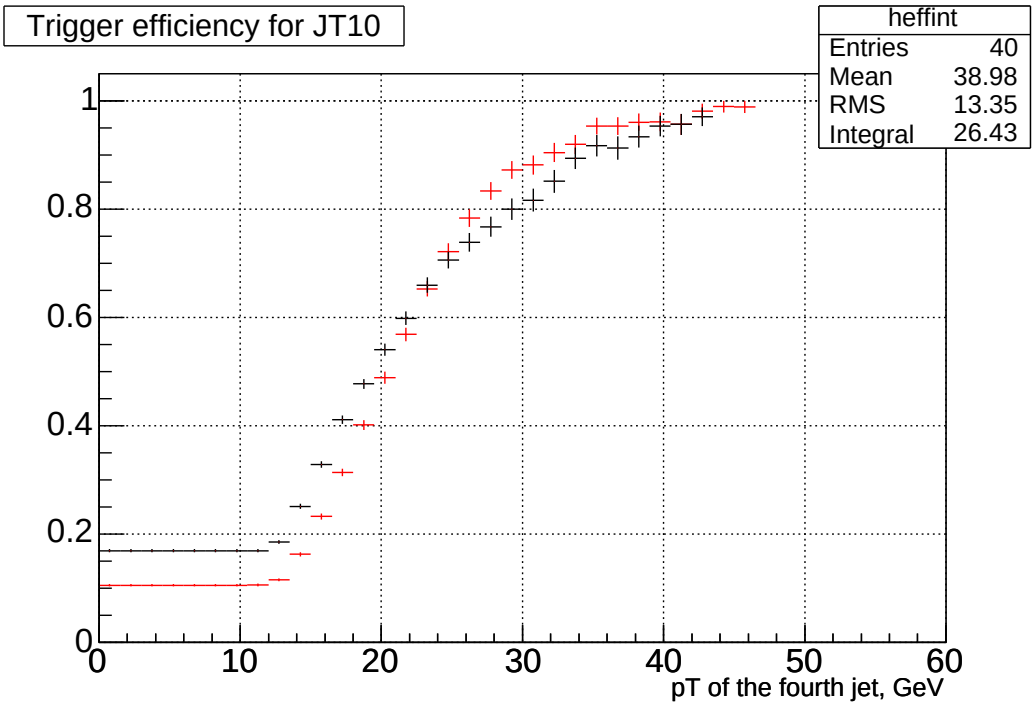

Figure 7.2: The trigger efficiency closure plot. Black is the MU_JT20_L2M0 data while red is top_trigger prediction for this data.

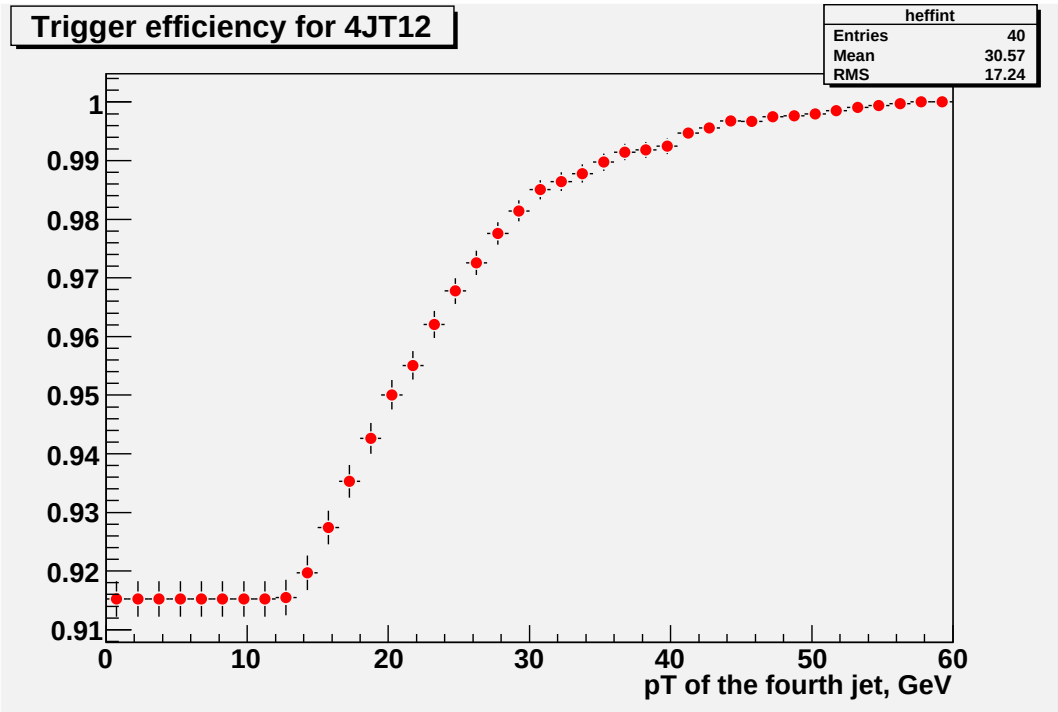

Figure 7.3: The trigger efficiency of the $t\bar{t} \rightarrow \tau + jets$ MC obtained using top_trigger as a function of the p_T of the 4th jet.

Table 7.2: The results of luminosity calculation for the PASS2 ALLJET top skim.

Stage	Luminosity (pb^{-1})	Stage efficiency (%)	Cumulative efficiency (%)
Delivered	482.6	100	100
Recorded	411.6	85.3	85.3
Good	352.5	85.6	73.0
Reconstructed	349.3	99.1	72.4

7.2 Data set

As described in section 7.1.1, the optimal combination of triggers for this analysis is composed of:

- The missing H_T trigger (MHT30_3CJT5)
- The ALLJET trigger (4JT10)

Together they yield over 85% signal acceptance.

The data skim (as subsets of the DØ recorded data are called), utilizing both of these triggers, would be optimal for this analysis. However, the closest thing available at the time of this work was the so-called ALLJET skim [45], which only contains the data collected by the 4JT10 trigger (and its subsequent varations). The ALLJET skim is 70% efficient for the signal.

The full PASS2 (all DØ data up to September 2004) ALLJET skim is processed through the standard DØ top group data quality criteria, discarding bad luminosity blocks, at the same time computing the recorded luminosity (as described in section 4.2.8). The results are presented in Table 7.2. The total luminosity available for the analysis amounts to 349 ± 23 pb^{-1} [14].

Table 7.3 lists the breakdown of this luminosity between the different trigger versions.

Table 7.3: Luminosity of the ALLJET skim for different DØ trigger list versions.

Trigger version	Trigger name	Luminosity (pb^{-1})
8.0	4JT10	19.4
9.0	4JT10	21.2
10.0	4JT10	15.1
11.0	4JT10	57.3
12.0	4JT12	195.0
13.0	JT2_4JT12L_HT	13.5
13.1	JT2_4JT12L_HT	27.8
13.3	JT2_4JT12L_HT	0

CHAPTER 8

$T\bar{T} \rightarrow \tau + JETS$ ANALYSIS

In this chapter the measurement of the $t\bar{t} \rightarrow \tau + jets$ cross section is presented. The major challenge of this channel lies in the fact that while its branching fraction is much less than that of the all jet channel (see Fig. 2.7) ,it has a similar background composition (dominated by multijet QCD). We start by briefly outlining the steps followed in order to suppress the background and extract the cross section.

8.1 Outline

The analysis procedure involved several stages:

- Preselection (section 8.2). At least 4 jets and $\not\!\!E_T$ significance > 3 are required. 653,727 events are selected in the data, with a prediction of 109.9 $\pm$ 7.3 $t\bar{t}$ events, for a S:B $\approx$ 1:6,000.

- ID cuts (section 8.3). At least one good τ lepton candidate and at least one tight SVT tag are required. We also required ≥ 2 jets with $|\eta| < 2.4$ and $p_T > 20$ GeV. 216 events are selected in the data while 9.3 $\pm$ 0.6 $t\bar{t}$ among them are expected. S:B $\approx$ 1:58.

- Topological NN (section 8.5). A sequence of two feed-forward NNs are trained and applied. The output is required to be greater than 0.9. With this final cut, we obtained 13 events in data with 4.9 $\pm$ 0.3 $t\bar{t}$ among them expected. S:B $\approx$ 1:2.5.

The W background was modeled using ALPGEN Monte Carlo simulation, while the QCD background was extracted from the data using the procedure described in section 8.4.

8.2 Preselection

The total number of events recorded by our trigger in the 349 pb^{-1} data is 17 million. The main goal of the preselection was to reduce this dataset, while imposing the most obvious and straightforward requirements that characterize the signal. Such characteristic features include the following:

- Moderate $\not\!\!E_T$ arising from the W leptonic decay and the τ decay.
- At least 4 jets must be present.
- At least 1 τ lepton and 2 b jets are present.

Since both τ ID and b-tagging involve complex algorithms which are likely to be signal-sensitive and may require extensive tuning, we have chosen not to use them at the preselection stage. Similarly, we chose not to impose any jet p_T cuts, since such cuts strongly depend on the JES corrections. It is better to apply those at a later stage.

The first 3 preselection criteria were chosen similar to the $t\bar{t} \rightarrow jets$ analysis [14]:

- Primary vertex is reconstructed within the central tracker volume (60 cm in z from the detector center) and has at least 3 tracks associated with it.
- Veto on isolated electrons and muons to avoid overlap with the $t\bar{t} \rightarrow lepton + jets$ cross section analysis.
- $N_{jets} \geq 4$ with $p_T > 8$ GeV.

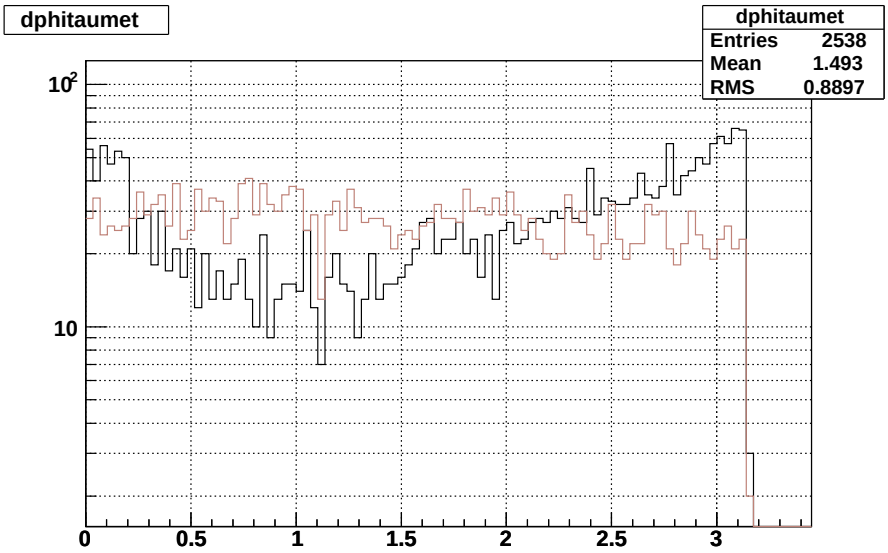

Figure 8.1: $\Delta\phi$ between reconstructed τ and $\not\!\!E_T$ for QCD (black) and $t\bar{t} \to \tau + jets$ (red).

At this point, the $t\bar{t} \to e + jets$ and $t\bar{t} \to \mu + jets$ analysis [12] are applying cuts on $\Delta\phi$ between the lepton and $\not\!\!E_T$ as well as so-called "triangular" cuts in the $\Delta\phi$ - $\not\!\!E_T$ plane. The goal is to eliminate events with fake $\not\!\!E_T$. The neutrino and the lepton coming from the W are expected to fly in the opposite azimuthal directions most of the time. However, as can be observed in Fig. 8.1, no such simple cuts are obvious in the case of τ. That is to be expected since the τ itself produces a neutrino in its decay, contributing to $\not\!\!E_T$. So, instead, a new variable is proposed to cut off the fake $\not\!\!E_T$ events and reduce the sample size.

$\not\!\!E_T$ significance [47] is defined as the measure of likelihood of the reconstructed $\not\!\!E_T$ arising from invisible particles, such as neutrinos, rather than fluctuations in detector measurements. It can be seen from Fig. 8.2 that it is an effective way to reduce the data skim. $\not\!\!E_T$ significance > 3 is required in preselection.

Now we need to scale the original 10K events of the MC sample to 349 pb^{-1}. The total $t\bar{t}$ cross section is 6.8 pb [10]. Taking into account the branching fraction to the hadronic decaying $\tau + jets$ mode, the effective cross section comes out to be:

$$B(\tau \to hadrons) \cdot B(t\bar{t} \to \tau + jets) \cdot \sigma(t\bar{t}) = 0.65 \cdot 0.15 \cdot 6.8 = 0.66 \text{ pb}$$

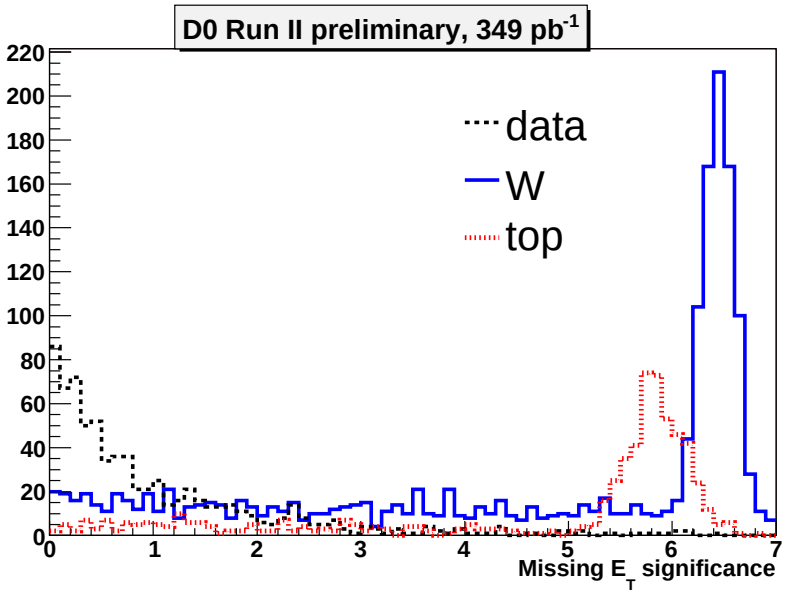

Figure 8.2: $\not\!\!E_T$ significance for QCD-dominated data (black), $W + jets$ (blue) and $t\bar{t} \rightarrow \tau + jets$ (red).

Throughout this work we had, however, used the value of $\sigma(t\bar{t})$ of 5.5 pb, the value computed by the ALPGEN simulation taking into account the generation cuts. The effective cross section used for scaling is then 0.53 pb. Since this value is only used for reference and optimization of S:B it's of no importance which number is used.

The relative fractions of the $W + jets$ processes for different jet flavors were taken from ALPGEN simulation as ratios of cross sections. These cross sections ware then normalized to the measured total value of $\sigma(W + jets) = 4.5 \pm 2.2$ pb [48].

Table 8.1 shows the results of the preselection for both data and the backgrounds.

8.3 Results of the ID cuts

The next step was to apply the requirement of τ and b tagging. Table 8.2 shows the selection criteria that we apply to data and MC and the resulting selection efficiencies. The results of this procedure are given in Table 8.3. It can be noted that S:B at this stage

Table 8.1: Preselection results. Shown are the total acceptances (including preselection) and the number of events scaled to 349 $\pm$23 pb^{-1} (no systematic uncertainties except for this luminosity error are included). The ALPGEN generation parameters are described in [12]. An estimate of the QCD background is not included. "j" stands for a light quark or a gluon.

	# passed	ALPGEN σ, pb	# passed scaled
data	653727/17M		653727
$t\bar{t} \to \tau + jets$	6141/10878	0.821 $\pm$ 0.004	109.93 $\pm$7.26
$Wbbjj \to \tau\nu + bbjj$	2321/11576	0.222 $\pm$ 0.044	9.98 $\pm$ 2.08
$Wccjj \to \tau\nu + ccjj$	2289/10995	0.527 $\pm$ 0.059	24.77 $\pm$ 3.22
$Wcjjj \to \tau\nu + cjjj$	2169/10435	0.920 $\pm$0.087	42.23 $\pm$ 4.87
$Wjjjj \to \tau\nu + jjjj$	2683/11920	14.14 $\pm$ 1.30	720.33 $\pm$ 81.48

Table 8.2: b-tagging and τ ID. In the MC we use the b-tagging certified parameterization rather than actual b-tagging. That is we applied the b-tagging weight ($bTagProb$). We also used the triggering weight as computed by the trigger efficiency parameterization ($TrigWeight$).

	Data	taggingMC
	≥ 1 τ with $\lvert\eta\rvert < 2.4$ and $p_T > 20$ GeV	≥ 1 τ with $\lvert\eta\rvert < 2.4$ and $p_T > 20$ GeV
	≥ 1 SVT	$TrigWeight \cdot bTagProb$
	≥ 2 jets with $\lvert\eta\rvert < 2.4$ and $p_T > 20$ GeV	≥ 2 jets with $\lvert\eta\rvert < 2.4$ and $p_T > 20$ GeV

is 1:58, which is way too low. In section 8.5 we will describe the topological NN used to enhance the signal content.

For the purposes of this analysis we define 3 subsamples out of the original preselected data sample:

- The "signal" sample - requires at least 1 τ lepton with $NN_\tau > 0.95$ and at least one SVT tag (as in Table 8.2). This is the main sample used for the measurement. It contains 268 events.

- The "τ veto sample" - Same selection, but instead of $NN_\tau > 0.95$, $0 < NN_\tau < 0.5$ was required for τ lepton candidates and no events with "good" ($NN_\tau > 0.8$) τ

Table 8.3: b-tagging and τ ID results. Shown are the total acceptances (including preselection) and the number of events scaled to 349 pb^{-1}. An estimate of QCD background is not included.

	# passed	Acceptance	# passed scaled
data	216/653727		216
$t\bar{t} \to \tau + jets$	524.0/6141	0.0480±0.0020	9.320±0.620
$Wbbjj \to \tau\nu + bbjj$	54.5/2321	0.0150±0.0024	0.012±0.002
$Wccjj \to \tau\nu + ccjj$	13.3/2289	0.0039±0.0012	0.034±0.005
$Wcjjj \to \tau\nu + cjjj$	8.0/2169	0.0025±0.0010	0.160±0.020
$Wjjjj \to \tau\nu + jjjj$	3.3/2683	0.0009±0.0006	0.860±0.100

leptons were allowed. This sample is used for the topological NN training. It contains 21022 events.

- The "b veto" sample - at least 1 τ lepton with $NN_\tau > 0.95$, but no SVT tags. This sample is to be used for the QCD prediction. It contains 4642 events.

8.4 QCD modeling

The difference between the total number of $t\bar{t}$ and W events and data is attributed to QCD events, where the τ candidate is a misidentified jet. In order to estimate this background contribution the following strategy was employed.

8.4.1 Parameterization

In this section our definition of the τ fake rate is different from the one in Fig. 5.7. There, the goal was to determine the total number of fake τ candidates per event in the ALLJET data skim. Now our goal is to estimate the number of events that would pass all

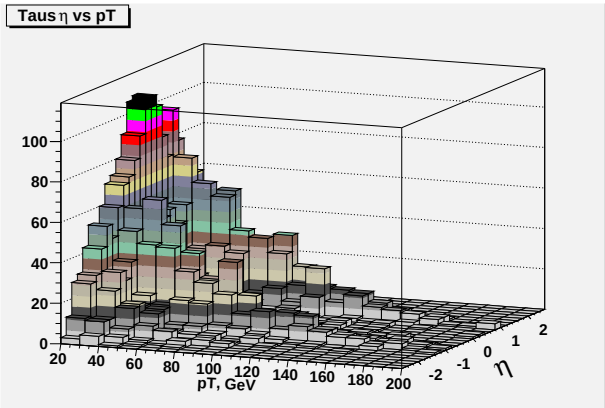

Figure 8.3: τ candidates in the QCD sample.

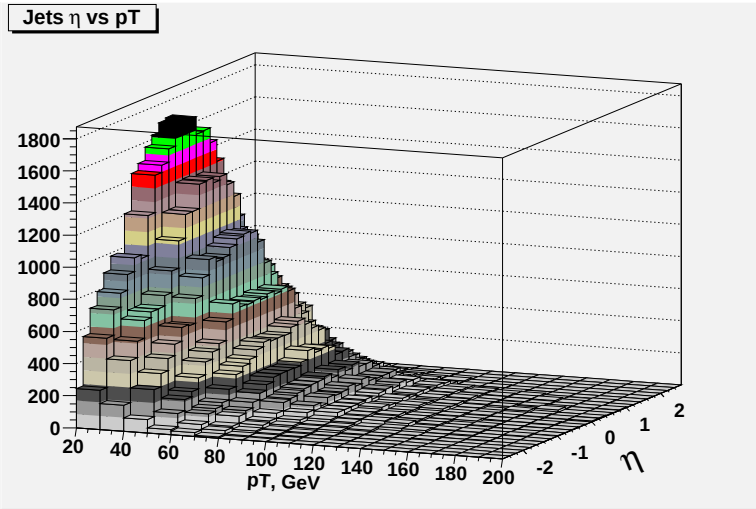

Figure 8.4: Jets in the QCD sample.

our signal selection criteria, yet contain no real τ leptons but only fakes. In other words, we are modeling the QCD contribution to our final $t\bar{t}$ candidate event selection.

We started with the "b veto" sample, which, for all practical purposes, consists purely of QCD events. Almost all τ candidates in it have to be fake. Fig. 8.3 shows the distribution of these candidates by p_T and η. On the other hand, Fig. 8.4 displays the jets found in the same events.

Since the τ here are really jets, we can simply divide the τ histogram by the jet histogram bin by bin to parameterize the τ fake rate. Figure 8.5 demonstrates this pa-

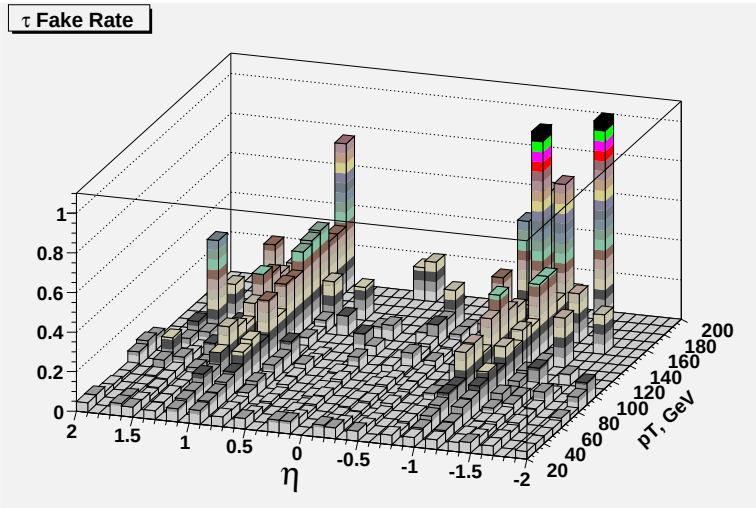

Figure 8.5: τ fake rate parameterization.

rameterization.

The large isolated spikes are due to the small statistics available in the bins. In order to reduce this effect and minimize the statistical uncertainty we had performed a 2D fit to this distribution. This fit is then to be used for the QCD prediction.

8.4.2 Fit

Fitting was done separately in η and p_T projections. We assumed that the 2D parameterization can be simply factored in two components:

$$F(\eta, p_T) \equiv A(\eta) \cdot B(p_T)$$

The η fitting function was chosen to be a 7th degree polynomial:

$$A(\eta) \equiv \sum_{i=0}^{7} a_i \eta^i$$

if $\eta = 0$ $a_1 = 0$ was set to avoid singularity.

The fitting function for p_T has been picked so that it would describe the data well and had not been monotonous (that is we want $\lim_{p_T \to \infty} B\left(p_T\right) \to \text{const}$) :

$$B(p_T) \equiv b_1 \cdot \exp\left(\frac{p_T}{\left(p_T + b_3\right)^2}\right) + b_2 \cdot \left(\frac{p_T}{p_T + b_3}\right)$$

The distributions in η and p_T had been separately and fitted with $A(\eta)$ and $B(p_T)$. The result of this procedure is shown in Fig. 8.6.

The fit in η fails around $\eta = 1$. This is the ICD region (section 4.2.5.2), which is expected to have different effects on different τ types. In order to account for this effect we have performed the fit for each type separately, as shown in Fig. 8.7. We see that the effect of the ICD region is largest in type 1 and is minor for type 2. At the same time the η distribution in signal (Fig. 6.7) is fairly uniform.

Hence we imposed the following cuts to remove these ICD fakes :

- For type 1: $0.8 < |\eta| < 1.3$ region removed
- For type 3: $0.85 < |\eta| < 1.1$ region removed

With these cuts, the fits were significantly improved (Fig. 8.8).

As can be seen from Table 8.4, type 1 τ contributes less than 1 signal event even before the η cut. After the cut its contribution is totally negligible. So, we decided to discard these events from the $t\bar{t}$ cross section measurement. The final 2D parameterization of the τ fake rate ($F(\eta, p_T)$) is shown in Fig. 8.9. Table 8.5 shows how the η selection affects the number of events.

8.4.3 Closure tests

The validity of fitting separately in η and p_T ignoring any possible correlations needs to be checked. Figure 8.10 shows the results of the closure test perfomed for this purpose. In the same "b veto sample" we had applied the resulting $F(\eta, p_T)$ to each jet and compared

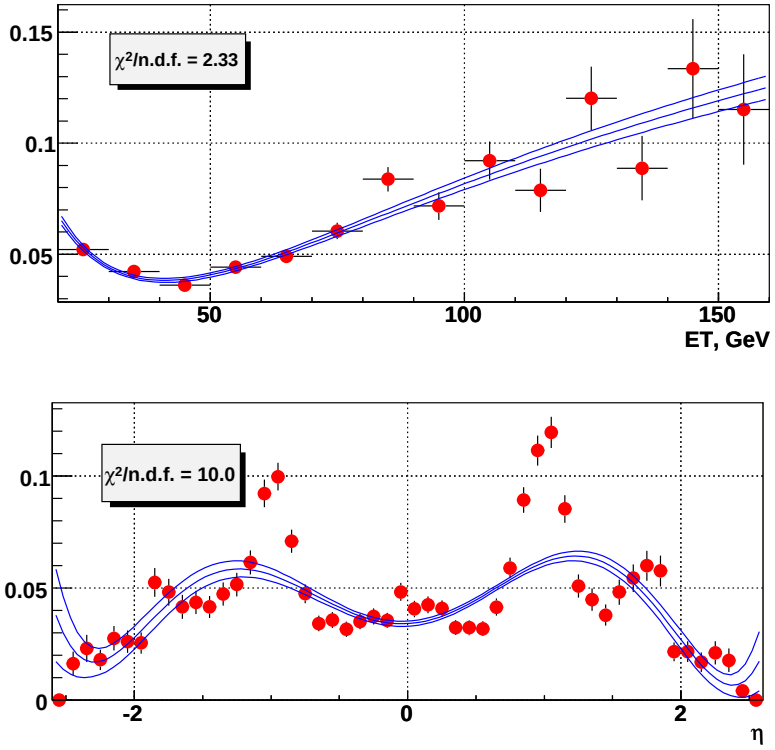

Figure 8.6: Fit of the η and p_T distributions of the τ fake rate.

Table 8.4: b-tagging and τ ID results per type. Shown are the number of events predicted in signal and observed in the data as well as the cuts applied.

data	taggingMC
≥ 1 τ with $\|\eta\| < 2.4$ and $p_T > 20$ GeV	≥ 1 τ with $\|\eta\| < 2.4$ and $p_T > 20$ GeV
≥ 1 SVT	$TrigWeight \cdot bTagProb$
≥ 2 jets with $\|\eta\| < 2.4$ and $p_T > 20$ GeV	≥ 2 jets with $\|\eta\| < 2.4$ and $p_T > 20$ GeV

	Type 1	Type 2	Type 3
data	28	91	94
$t\bar{t} \rightarrow \tau + jets$	0.73±0.05	5.61±0.37	3.12±0.20
$W \rightarrow \tau\nu + jets$	0.09±0.01	0.93±0.04	0.39±0.02

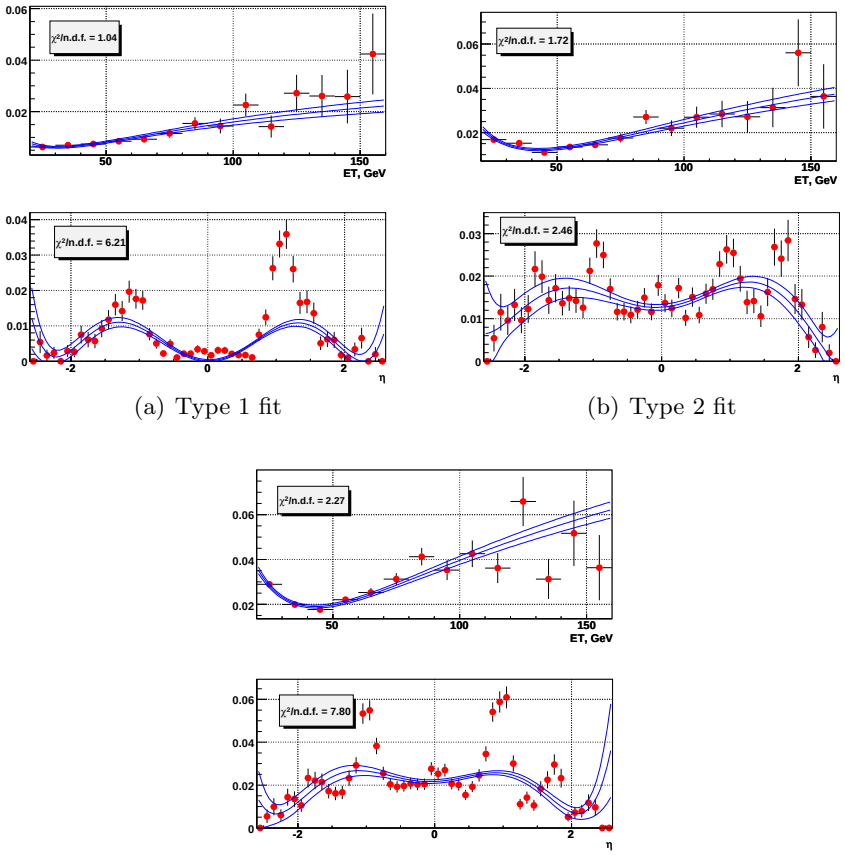

(a) Type 1 fit

(b) Type 2 fit

(c) Type 3 fit

Figure 8.7: Fit of the η and p_T distributions of the τ fake rate by different types of τ decays.

Table 8.5: b-tagging and τ ID results per type after the η cut (as explained in section 8.4). Shown are the number of events predicted in signal and observed in the data. An estimate of QCD background is not included.

	Type 2	Type 3
data	91	71
$t\bar{t} \rightarrow \tau + jets$	5.61±0.37	2.81±0.18
$W \rightarrow \tau\nu + jets$	0.93±0.04	0.32±0.01

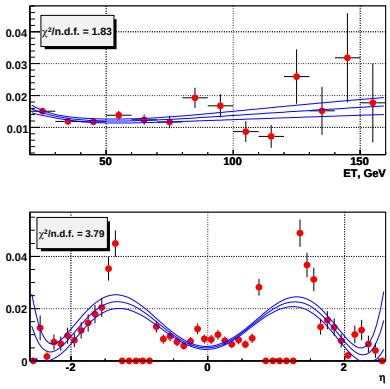

(a) Type 1 fit

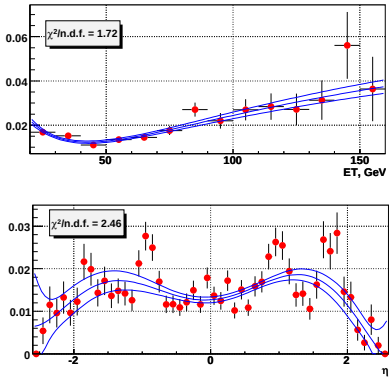

(b) Type 2 fit

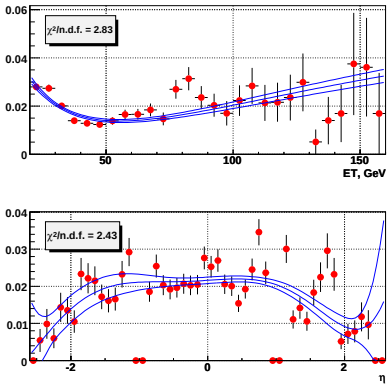

(c) Type 3 fit

Figure 8.8: Fit of the η and p_T distributions of the τ fake rate. The ICD region has been cut off for types 1 and 3.

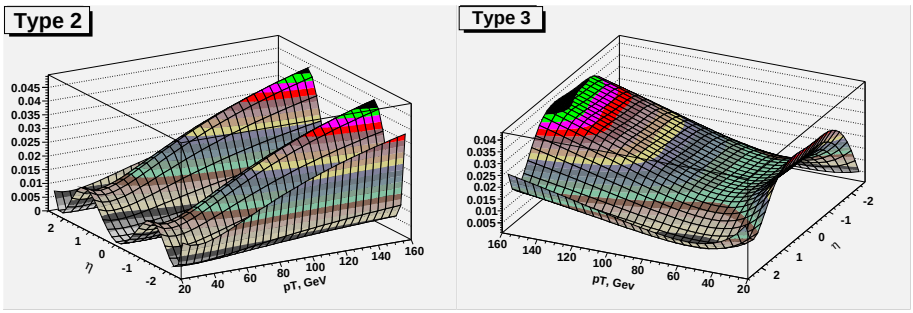

(a) Type 2 2D fit

(b) Type 3 2D Fit

Figure 8.9: The 2D combined parametrization (in η and p_T) of the τ fake rate.

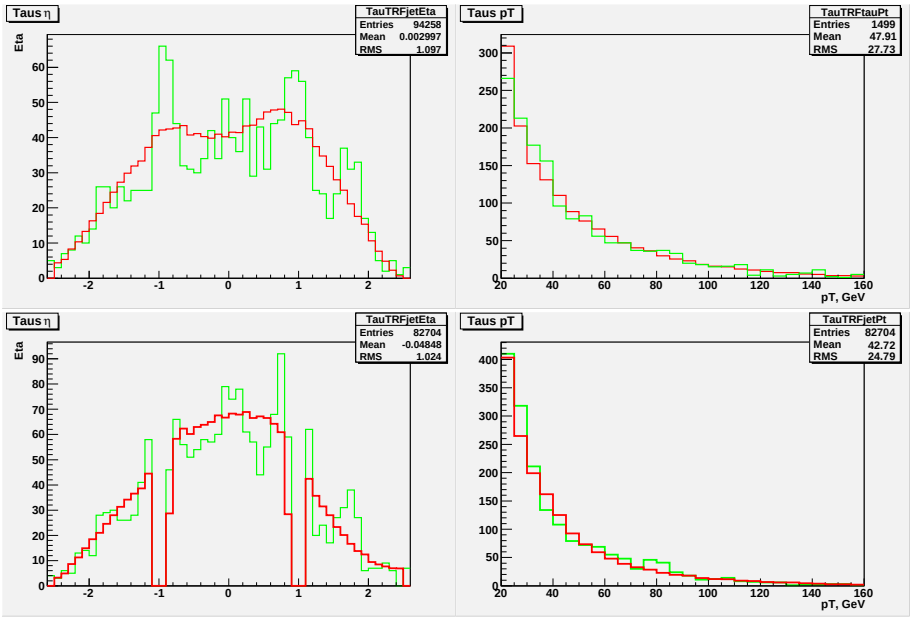

Figure 8.10: The closure test of the τ fake rate function. The red histograms are for the actual τ candidates in the "veto" sample. The green ones are the prediction. The η distributions show differences, but they are within the uncertainties of the fit.

the resulting (predicted) τ distributions with ones obtained from the actual τ candidates (which are predominantly fakes).

However, one could imagine a pair of 2D distributions that would agree perfectly in both projections and yet be very different. In order to test against such a possibility we performed the same cross-check as before, but we required the jets to be from 0.5 to 1 in η. For such η "slice" we had applied $F(\eta, p_T)$ and compared the actual p_T with the predicted. Figure 8.11 demonstrates that the agreement is still fairly good.

8.4.4 Computing the QCD fraction

We assume that the probability for a jet to fake a τ is simply $F(\eta, p_T)$. Then, the probability that at least one of the jets in the event will fake a τ can be computed as follows:

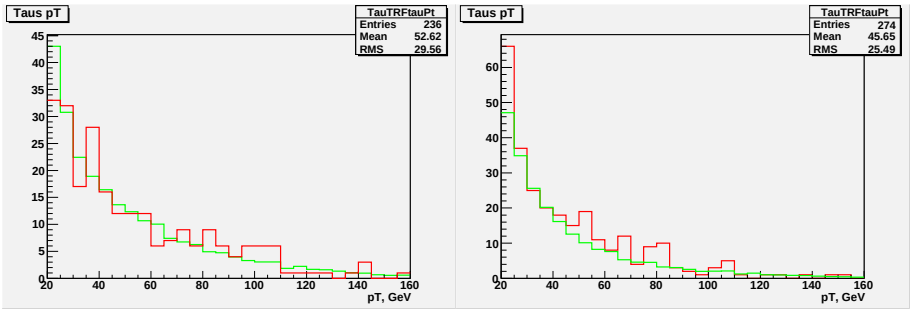

(a) Type 2 (b) Type 3

Figure 8.11: The closure test of the τ fake rate function. The red histograms are for the actual τ candidates in the "veto" sample. The green ones are the prediction. The jets had been selected with $0.5 < \eta < 1$. An asymmetric range was chosen to avoid possible bias.

$$P_{event} = 1 - \prod_j (1 - F(p_T^j, \eta^j))$$

Summing up such probabilities over the tagged data we obtain the QCD background estimation.

Using the results described in the previous section we get $N_{QCD} = 71.13 \pm 1.56$ for the τ type 2 and $N_{QCD} = 77.46 \pm 0.80$ for the τ type 3, which agrees with the observed data (in Table 8.5) fairly well. Also, the predicted distributions of the main topological variables (section 8.5) are in fairly good agreement with what is observed in the data (see the appendix).

8.5 Topological NN

For signal training sample 7481 preselected $t\bar{t}$ MC events were used (not the same as the 6141 selection sample events). For the background, the τ veto sample was used.

Similar to the all-jets analysis [14] we define 2 networks:

1. NN1: uses 3 topological variables: aplanarity, sphericity and centrality and 2 energy-based variables: H_T and $\sqrt{S}$.

2. NN2: uses the output of the first, W and top mass likelihood, b-jet's p_T and b-jet's decay length.

These are the kinematic and topological variables used:

- H_T - the scalar sum of all jet p_Ts (and τ).
- $\sqrt{S}$ - the invariant mass of all jets.
- Sphericity and Aplanarity - these variables are formed from the eigenvalues of the normalized momentum tensor of the jets in the event. These are expected to be higher in a typical top pair events than in a typical QCD event.
- Centrality, defined as $\frac{H_T}{H_E}$, where H_E is the sum of energies of the jets.
- Top and W mass likelihood - χ^2-like variable. $L \equiv \left(\frac{M_{3j}-M_t}{\sigma_t}\right)^2 + \left(\frac{M_{2j}-M_W}{\sigma_W}\right)^2$, where $M_t, M_W, \sigma_t, \sigma_W$ are top and W masses (175 GeV and 80 GeV respectively) and resolution values (45 GeV and 10 GeV, respectively [14]). M_{3j} and M_{2j} are 3 jet invariant masses composed of the jet combinations that minimize L.
- p_T and lifetime significance of the leading b-tagged jet.

Many of these variables (for instance, mass likelihood and aplanarity) are only defined for events with 2 or more jets. So, we require now 2 jets with $p_T > 20$ GeV and $|\eta| < 2.5$.

All these variables are plotted in the appendix, which serves also as an additional check of an agreement between the data and prediction. Two such plots are shown in Fig. 8.12. The NN input variables show fairly good agreement between between data and MC, which gives us confidence that the NN based on these variables will provide sensible output.

8.6 NN optimization

For training the NN we used the Multi Layer Perceptron (MLP) [50], as implemented in the ROOT framework. 7466 events were used for training, and 14932 for testing. The

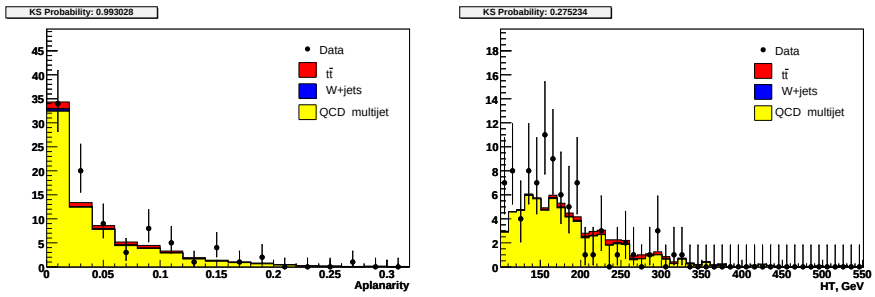

Figure 8.12: 2 of the 5 input variables of the first topological NN before the NN cut (τ type 2). The Kolmogorov-Smirnov (KS) probabilities [49] are shown, indicating how good the agreement is.

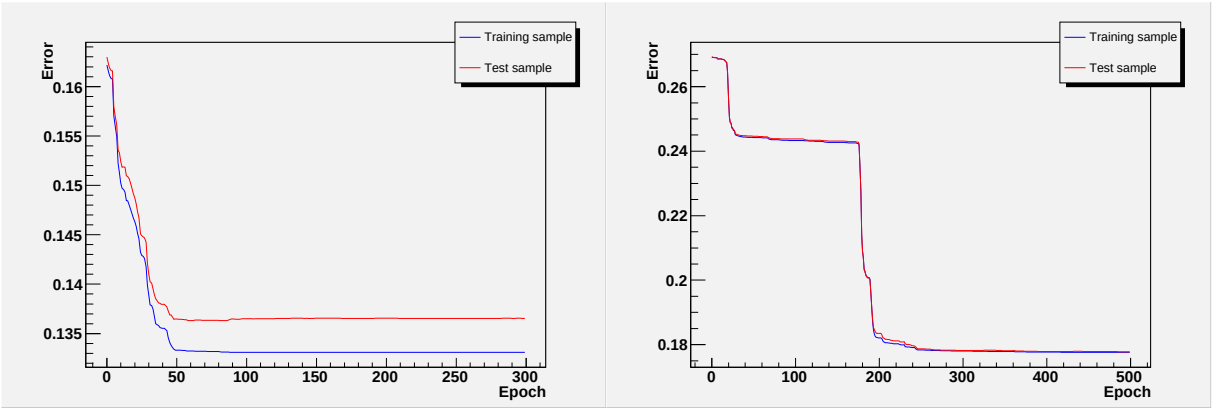

(a) The first NN

(b) The second NN

Figure 8.13: NN error. Red is test sample, blue is training sample.

fractional error for both signal and background is evaluated at each of the 500 training "epochs", showing how successful it has been in discriminating the test events (Fig. 8.13).

Figures 8.14 and 8.15 show the structure of the trained NN (blue interconnected nodes) and the performance evaluation based on the training samples. Figures 10.9 and 10.10 in the appendix show the final NN output in the main analysis data sample as well as in the signal and in the backgrounds.

The result of applying this NN to data is shown in Fig. 8.16. At this point we had to determine what cuts on the topological NN output maximize the signal significance. The signal significance is defined as $\frac{Number\,of\,signal\,events}{\sqrt{Number\,of\,Signal+Background\,events}}$ and is shown in Fig. 8.17 . The maximum is attained with $NN1 > 0.9$ for both types 2 and 3. Therefore this

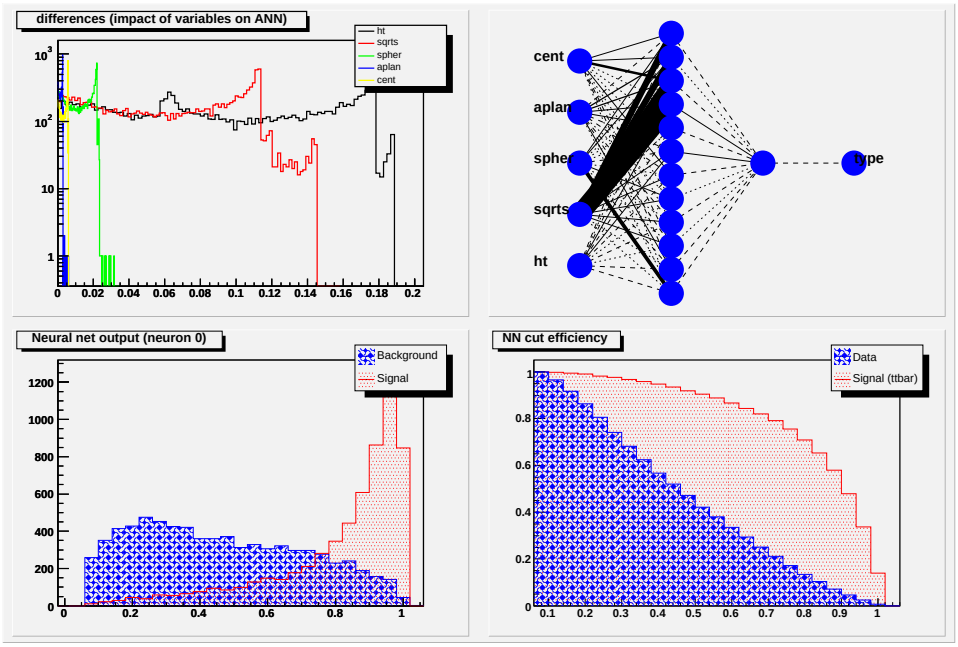

(a) The first NN

Figure 8.14: NN0 structure. The upper left plot shows the relative impact of the variables on the NN output. The bottom left is distribution of NNout, the bottom right - efficiencies. Red is signal, blue is background.

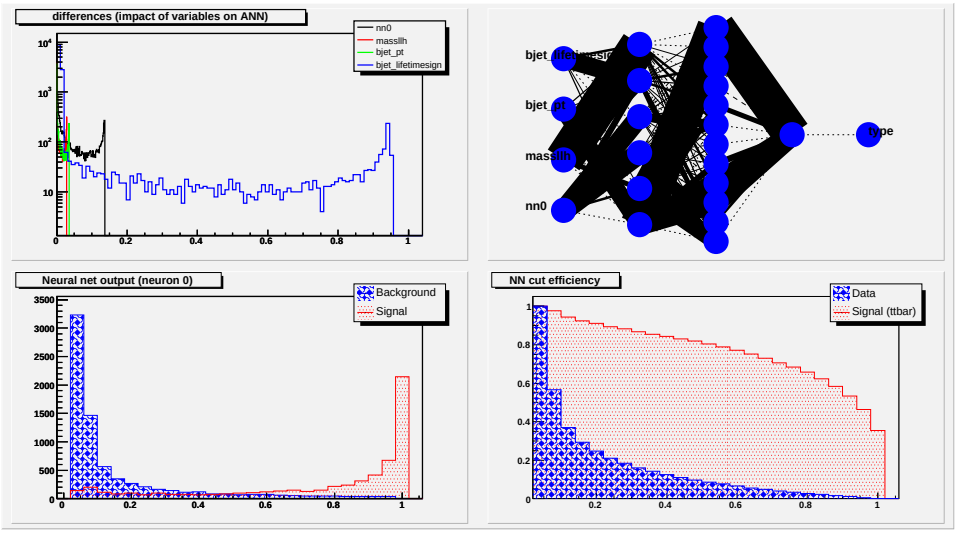

Figure 8.15: NN1 structure. The upper left plots show the relative impact of the variables on the NN output. The bottom left is distribution of the NN output, the bottom right - efficiencies. Red is signal, blue is background.

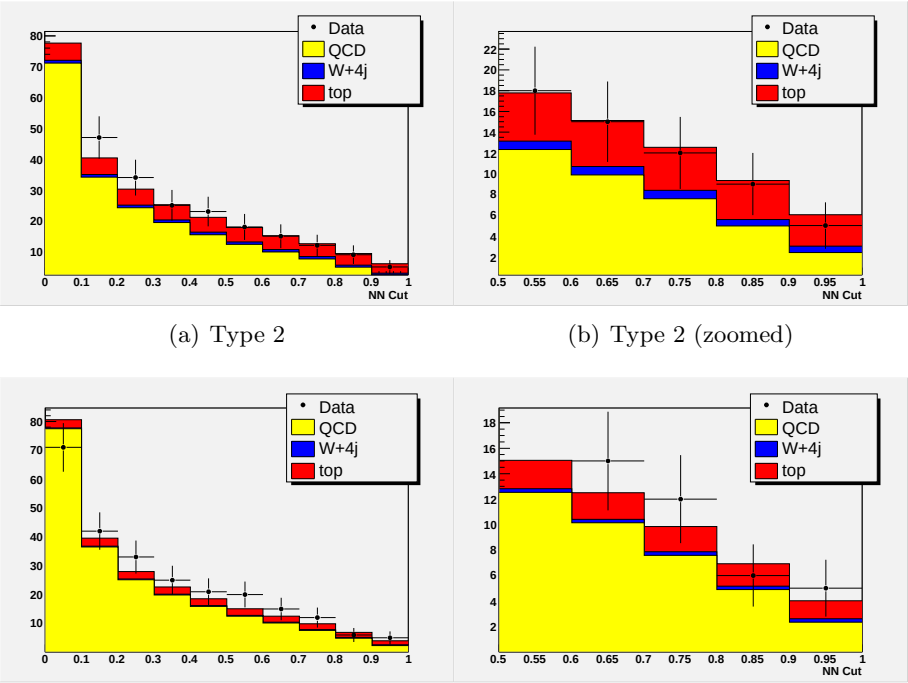

(a) Type 2 (b) Type 2 (zoomed)

(c) Type 3 (d) Type 3 (zoomed)

Figure 8.16: The result of applying the NN cut. $t\bar{t}$, W and QCD are plotted incrementally in order to compare with # of events observed in data. Only statistical uncertainties are shown. $\sigma(t\bar{t}) = 5.54$ pb is assumed. The right plot only shows the entries with high NN.

is the cut we've used for the cross section measurement. The results of this measurement are summarized in Table 8.6.

Table 8.6: The final result summary after the NN>0.9 cut; $\epsilon(t\bar{t})$ is the total signal acceptance.

Channel	N^{obs}	BR	$\int \mathcal{L}dt$, pb^{-}1	Backgrounds		$\varepsilon(t\bar{t})$ (%)	s (7 pb)	s+b
τ+jets type 2	5	0.1	349.3	$W \to \tau\nu$	0.60±0.03	1.57±0.01	$3.83^{+0.46}_{-0.51}$	$6.84^{+0.46}_{-0.51}$
				fakes	2.41±0.09			
τ+jets type 3	5	0.1	349.3	$W \to \tau\nu$	0.27±0.01	0.73±0.01	$1.80^{+0.22}_{-0.23}$	$4.39^{+0.22}_{-0.23}$
				fakes	2.33±0.09			

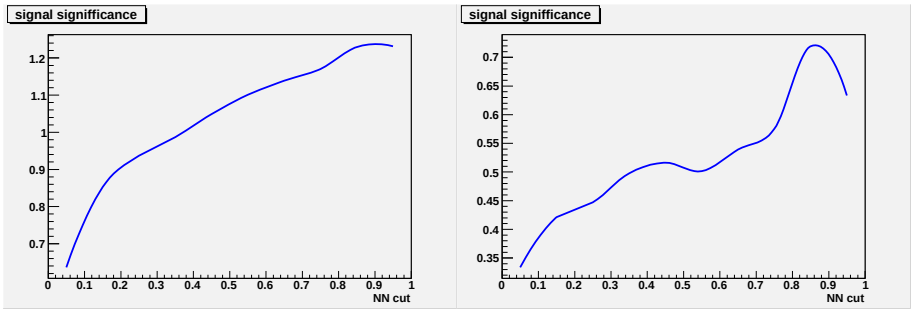

(a) Type 2 (b) Type 3

Figure 8.17: $t\bar{t} \rightarrow \tau + jets$ signal significance as functions of the minimum NN output requirement..

Table 8.7: Systematic uncertainties on $\sigma(t\bar{t})$ (in pb).

Channel	τ+jets type 2	τ+jets type 3
Jet Energy Scale	$^{+0.30}_{-0.27}$	$^{+0.53}_{-0.69}$
Primary Vertex	$^{-0.036}_{+0.037}$	$^{-0.093}_{+0.095}$
MC stat	$^{-0.22}_{+0.25}$	$^{-0.58}_{+0.65}$
Trigger	$^{+0.0025}_{-0.020}$	$^{+0.0056}_{-0.069}$
Branching ratio	$^{-0.071}_{+0.074}$	$^{-0.18}_{+0.19}$
QCD fake rate parameterization	$^{-0.17}_{+0.17}$	$^{-0.34}_{+0.34}$
$W \rightarrow \tau\nu$	$^{-0.19}_{+0.19}$	$^{-0.19}_{+0.19}$

8.7 Systematic uncertainties

. The most important systematic effects (except for the b-tagging, which is treated later) are summarized in Table 8.7.

8.7.1 The jet energy scale (JES)

The JES applied to data and MC have uncertainties associated with them. These uncertainties result in systematic shift in the measured cross section. To compute these sys-

tematics the JES corrections in MC were shifted up (or down) by $\delta JES^{data} = \sqrt{(\delta^{data}_{syst})^2 + (\delta^{data}_{stat})^2 + (\delta$

8.7.2 Primary Vertex and Branching Fraction

The PV and $t\bar{t}$ and W branching fractions had been assigned uncertainties of 1% and 2% correspondingly, the same as in [14].

8.7.3 Luminosity

The total integrated luminosity of the data used in this analysis is 349±23 pb^{-1}). This error yields the uncertainty quoted in Table 8.7.

8.7.4 Trigger

The trigger parameterization systematics is computed by top_trigger [46].

8.7.5 B-tagging

B-tagging uncertainty effects are taken into account by varying the systematic and statistical uncertainties on the MC tagging weights and observing the change in measured cross section.

These errors arise from several independent sources:

- B-jet tagging parameterization.
- C-jet tagging parameterization.

Table 8.8: b-tagging systematics sources.

Channel	τ+jets type 2	τ+jets type 3
b-tagging	$^{+0.076}_{-0.13}$	$^{+0.41}_{-0.26}$
c-tagging	$^{+0.16}_{-0.20}$	$^{+0.60}_{-0.48}$
l-tagging	$^{+0.0051}_{-0.0051}$	$^{+0.014}_{-0.014}$
SF_{hf}	$^{+0.00036}_{-0.00036}$	$^{+0.00094}_{-0.00094}$
SF_{ll}	$^{+0.00036}_{-0.00036}$	$^{+0.00094}_{-0.00094}$
μ b-tagging (data)	$^{+0.094}_{-0.091}$	$^{+0.25}_{-0.24}$
μ b-tagging (MC)	$^{-0.10}_{+0.11}$	$^{-0.25}_{+0.28}$
taggability	$^{+0.049}_{-0.048}$	$^{+0.13}_{-0.13}$

- Light jet tagging parameterization (negative tag rate). Derived by varying by $\pm 1\sigma$ the parameterization and adding in quadrature 8% relative uncertainty from the variation of the negative tag rate measured in different samples.

- Systematic uncertainties on the scale factors SF_{hf} and SF_{ll} (see section 5.7) are derived from the statistical error due to finite MC statistics.

- Semi-leptonic b-tagging efficiency parameterization in MC and in data.

- Taggability. This includes the statistical error due to finite statistic in the samples from which it had been derived and systematic, reflecting the (neglected) taggability dependence on the jet multiplicity.

The resulting effect of all of these error sources on the final number is summarized in Table 8.8 along with the total b-ID systematic uncertainty (quoted in Table 8.7).

8.7.6 Fake rate

The systematic uncertainty associated with the τ fake rate is just the statistical error of the fit, described in section 8.4.2.

8.7.7 W background prediction

The method used to describe the $W \rightarrow \tau\nu$ background is not perfect. There are two potential sources of error:

- Only W+4 partons MC have been used. It is, however, expected that W+2 partons and W+3 partons give some (albeit smaller) contribution. In order to properly take this into account one would need to combine all jet multiplicity samples. At the time of this work the ALPGEN generator did not have this capability. This leads to a slight underestimation of the result.

- The "b veto" sample may contain some W contribution, from $WJJJJ$ events. This leads to double-counting of these events and hence overestimation of the result.

A conservative estimate of 50% uncertainty on the number of W events in the final sample has been applied. That is, by varying this number up and down by 50% we observed the effect on the cross section (as quoted in Table 8.7). Since W is a small contributor the effect of such an overestimated uncertainty on the final $\sigma(t\bar{t})$ is small.

8.8 Cross section

The cross section is defined as $\sigma = \frac{Number\,of\,signal\,events}{\varepsilon(tt)\cdot BR(tt)\cdot Luminosity}$. The results are:

$\sigma(t\bar{t})$ from type 2 τ + jets:

$$3.63\ ^{+4.72}_{-3.50}\ (\text{stat})\ ^{+0.49}_{-0.48}\ (\text{syst})\ \pm 0.24\ (\text{lumi})\ \text{pb}$$

$\sigma(t\bar{t})$ from type 3 τ + jets:

$$9.39\ ^{+10.10}_{-7.49}\ (\text{stat})\ ^{+1.25}_{-1.18}\ (\text{syst})\ \pm 0.61\ (\text{lumi})\ \text{pb}$$

The combined cross section was estimated by minimizing the sum of the negative log-likelihood functions for each channel. The functional form of the likelihood function was the same as that used for the $e\mu$ channel ([13]):

$$L(\sigma, \tilde{N}_i, {N_i}^{obs}) \equiv -\log\left(\prod_{i=1}^{2} \frac{{\tilde{N}_i}^{{N_i}^{obs}}}{{N_i}^{obs}} e^{-\tilde{N}_i}\right) \tag{8.1}$$

Here $\tilde{N}_i =$ is the number of events in each channel i assuming the cross section σ and ${N_i}^{obs}$ is the actual number of candidate events in the data. Combined cross section yields

$$\sigma(t\bar{t}) = 5.05 \ {}^{+4.31}_{-3.46} \ \text{(stat)} \ {}^{+0.68}_{-0.67} \ \text{(syst)} \ \pm 0.33 \ \text{(lumi)} \ \text{pb}$$

CHAPTER 9

SUMMARY AND OUTLOOK

This note presents the measurement of $\sigma(t\bar{t})$ at $\sqrt{s} = 1.96$ TeV from DØ Run II. The decay channel studied involves one hadronically decaying τ lepton, two b-jets, two light jets and $\not\!\!E_T$. The trigger and the corresponding 349±23 pb^{-1} dataset were shared with the all-jet channel [14].

The main challenge was to reject the very large QCD multijet background, while at the same time properly handling the physical $W+4j$ background. In order to achieve this, NN-based τ ID and SVT b-tagging algorithms were employed. In addition, the relevant topological variables were combined into a NN trained to differentiate the signal from QCD. The type 2 and 3 τ were treated as independent channels and then combined.

In the end we measured the cross section (assuming a top mass of 175 GeV) to be

$$5.05\ ^{+4.31}_{-3.46}\ \text{(stat)}\ ^{+0.68}_{-0.67}\ \text{(syst)}\ \pm 0.33\ \text{(lumi)}\ \text{pb}$$

This result is in agreement with the theoretically predicted value of 6.8±0.4 pb ([10]) as well as other DØ and CDF measurements ([14, 12]), as shown in Fig. 9.1. Statistical uncertainties are far larger than the systematic ones in this measurement. Therefore, with more data collected by the DØ experiment, the result will improve and will afford good sensitivity for new physics, such as the Charged Higgs boson (section 3).

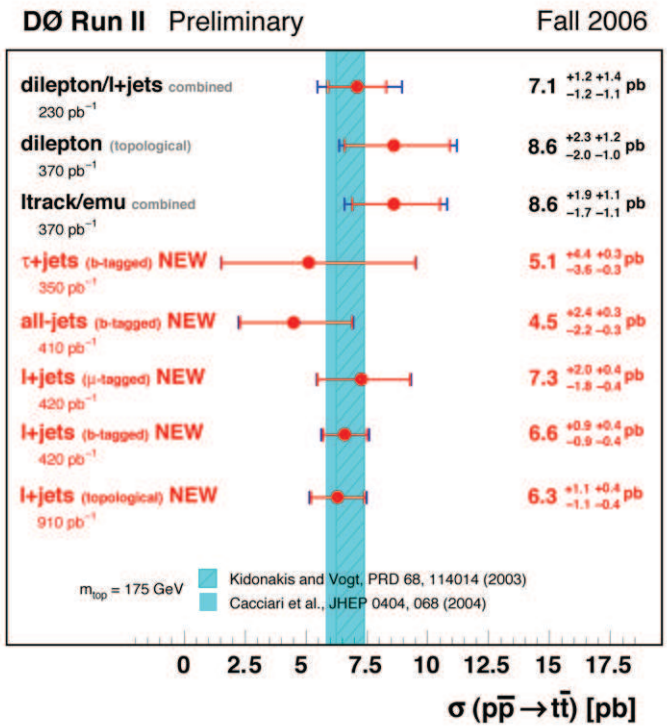

Figure 9.1: Results of Run II top pair production cross section measurement at DØ .

REFERENCES

[1] S. F. Novaes, Standard Model: An Introduction, arXiv:hep-ph/0001283v1.

[2] Standard Model Lagrangian.
URL `http://home.broadpark.no/~aklepp/astri/thesis/node52.html`

[3] P.Langacker, W and Z Physics, in: Proc. 1990 CCAST (World Laboratory) Symposium/Workshop on TeV Physics, Beijing, China, Vol. 8, 1990, p. 108.

[4] S. Martin, A Supersymmetry Primer, hep-ph/9709356.

[5] LEP Collaborations: Phys. Lett. B 276 247, 1992.

[6] S. Abachi, et al., Phys. Rev. Lett. 74 (1995) 2632.

[7] G. Otero, Measurement of the top quark pair production cross section in pbar-p collisions at sqrt(s)=1.96 TeV, PhD Thesis, 2006

[8] S. Willenbrock: Hadron Colliders, the Standard Model and Beyond, hep-ph/0212032,2002.

[9] M.E. Peskin and D.V. Schroeder, An introduction to quantum field theory (Perseus, 1995).

[10] Next-to-next-to-leading order soft-gluon corrections in top quark production, Phys. Rev. D 68, 114014 (2003).

[11] S.Eldelman *et al.* (Particle Data Group), Phys. Lett. B 592, 1(2004) and 2005.

[12] Measurement of the ttbar cross section in the lepton+jets channel at sqrt(s) = 1.96 TeV (topological) , DØ Notes **4667** and **4662**.

[13] M.Besancon et al. Measurement of the $t\bar{t}$ Production Cross-Section at $\sqrt{s} = 1.963\,TeV$ in Electron Muon Final States, DØ Note **4877**.

[14] Measurement of the $t\bar{t} \rightarrow all - jets$ production cross section using Secondary Vertex Tagging, DØ Note **4830**.

[15] Ta-Pei Cheng, Ling-Fong Li, Gauge Theory of Elementary Particle Physics, (Oxford, 1988).

[16] J. A. Coarasa, J. Guasch, and J. Sola, Report No. UAB-FT-451, 1999, hep-ph/9903212.

[17] CDF Charged Higgs webpage.
URL `www-cdf.fnal.gov/physics/new/top/2005/ljets/charged_higgs/`

[18] Search for the charged Higgs boson in the decays of top quark pairs in the $e\tau$ and $\mu\tau$ channels at sqrt[s]=1.8 TeV, PRD 62:012004, 2000.

[19] Direct Search for Charged Higgs Bosons in $t\bar{t}$ events, DØ Note **4357**.

[20] Baden, A. R., Jets and kinematics in hadronic collisions. Int. J. Mod. Phys. A13:1817-1845,1998.

[21] V. Shiltsev, Status of Tevatron Collider Run II and Novel Technologies for Luminosity Upgrades, in: Proc. 2004 European Particle Accelerator Conference, Lucern, Switzerland, Vol. 1, 2004, p. 239.

[22] Tevatron Run II Handbook.
URL `www-bd.fnal.gov/lug/`

[23] J. Ellison, The 0̸ Detector Upgrade and Physics Program arXiv:hep-ex/0101048v2.

[24] S. Abachi, et al., Nucl. Instrum. Methods Phys. Res. A 338 (1994) 185.

[25] V. M. Abazov *et.el*. [D0 Collaboration], Nucl. Instrum. Methods (to be published), arXiv:physics/0507191.

[26] T. Zimmerman, et al., IEEE Trans. Nucl. Sci. **42** (1995) 803.

[27] M.D. Petroff and M.G. Staplebroek, IEEE Trans. Nucl. Sci., **3 6**, No. 1 (1989) 158; M.D. Petroff and M. Attac, IEEE Trans. Nucl. Sci., **36**, No. 1 (1989) 163.

[28] DiLella L. Annu. Rev. Nucl. Part. Sci. 35:107 (1985).

[29] T. Edwards, et al., Fermilab-TM-2278-E (2004).

[30] A. Baranovski, et al., Fermilab-TM-2175 (2002).

[31] G. Hesketh., "Central Track Extrapolation Through the D0 Detector", DØ Note **4079** (2003).

[32] Ariel Schwartzman, Meenakshi Narian, "Vertex fitting by means of the Kalman Filter Technique", DØ Note **3907** (2001).

[33] E. Busato, B. Andrieu, Jet Algorithms in the D Run II Software: Description and Users Guide, DØ Note **4457** (2004).

[34] L. Saweyer and A.L Stone, Missing ET Reconstruction: Variables and Meth- ods, DØ Note **3957** (2002).

[35] EM ID certification,
URL `http://www-d0.fnal.gov/phys_id/emid/d0_private/certification/`

[36] C. Clement, et al.,"MuonID Certification for p14", DØ Note **4350** (2004).

[37] DØ τ ID certification, DØ Note **4773**.

[38] Search for the Associated Production of Charginos and Neutralinos in the muon + tau + lep Final State (Conference Note), DØ Note **4742**.

[39] Search for The Associated Production of Charginos and Neutralinos in the muon+tau+lep Final State, DØ Note **4743**.

[40] SVT webpage
URL http://www-d0.fnal.gov/phys_id/bid/d0_private/certification/p14Pass2/SVT/

[41] ALPGEN home page.
URL http://mlm.home.cern.ch/mlm/alpgen/

[42] PYTHIA 6.206, [hep-ph/0108264].

[43] D0GSTAR home page.
URL http://www-d0.fnal.gov/d0dist/dist/releases/p14.07.00/d0gstar

[44] TRIGSIM home page.
URL http://www-d0.fnal.gov/computing/trigsim/trigsim.html

[45] Luminosity of the ALLJETS data skim.
URL http://www-clued0.fnal.gov/~gwatts/pass2/ALLJETS.html

[46] Top Trigger Efficiency Measurements and the top_trigger package, DØ Note **4512**.

[47] $\not\!\!E_T$ Significance Algorithm in RunII data, DØ Note **4254**.

[48] Measurement of $W^{\pm} \rightarrow e^{\pm}\nu$ + Inclusive n-jet Cross Sections with CDF Data at Tevatron Run II.
URL http://www-cdf.fnal.gov/physics/new/qcd/wjets/Wjet_ana/Wjet_ana.ps

[49] Kolmogorov-Smirnov Goodness-of-Fit Test.
URL http://www.itl.nist.gov/div898/handbook/eda/section3/eda35g.htm

[50] MLPfit home page.
URL http://schwind.home.cern.ch/schwind/MLPfit.html

CHAPTER 10
CONTROL PLOTS

In Figs. 10.1 and 10.2 one can see the plots of the first NN before the final cut, and on 10.3 and 10.4 are the input variables of the second NN.

After requiring NN2 > 0.95 the same variables were plotted in Figs. 10.5, 10.6, 10.7 and 10.8.

On the Figs. 10.9 and 10.10 we can see how the NN distributions look for type 2 and 3 channels respectively.

The last two Figures in this appendix (10.11 and 10.12) show jet multiplicity for these channels.

The error bars represent the statistical uncertainties only.

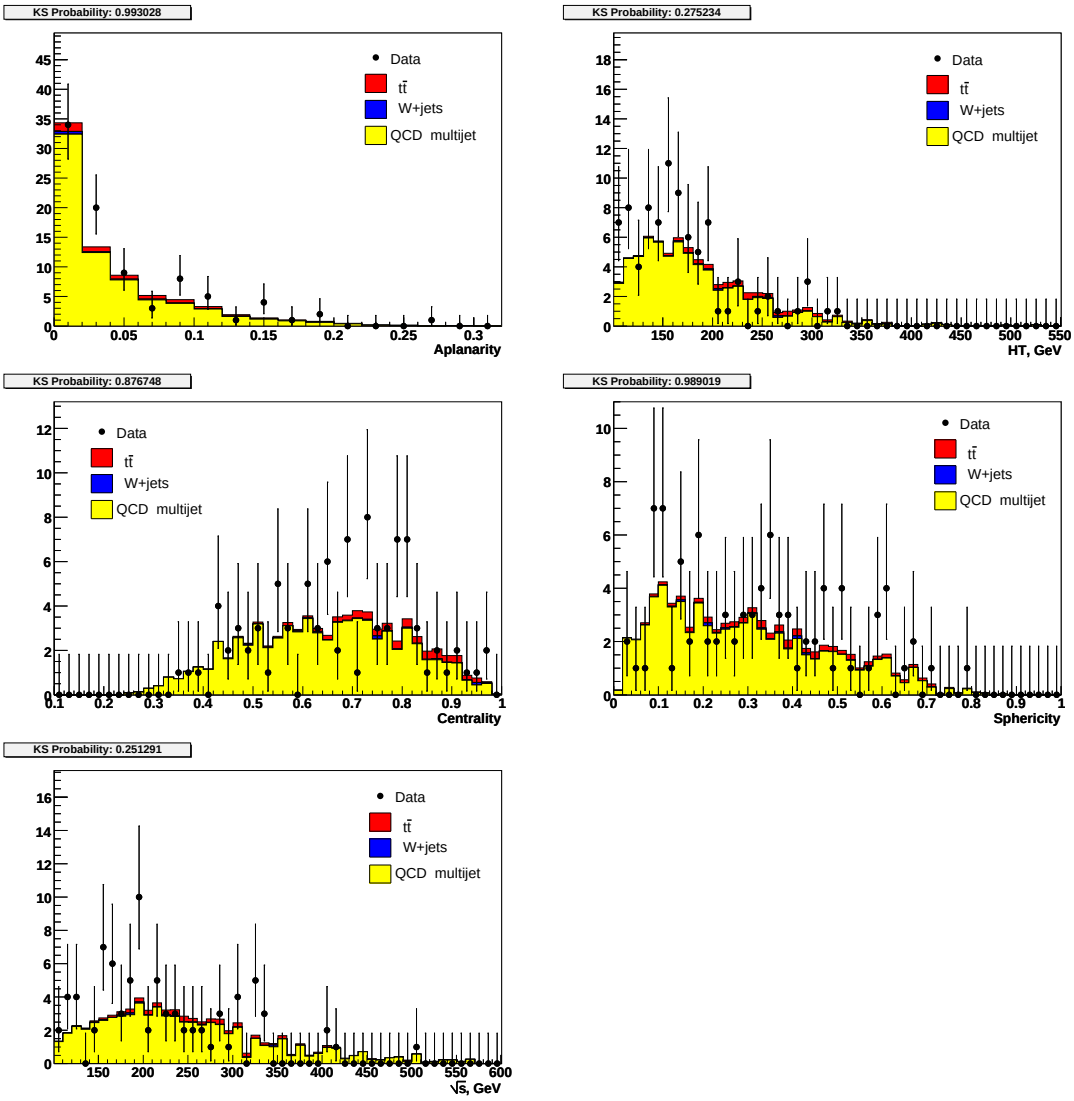

Figure 10.1: The 5 input variables of the first topological NN before the NN cut (τ type 2). The Kolmogorov-Smirnov (KS) probabilities are shown, indicating how good the agreement is.

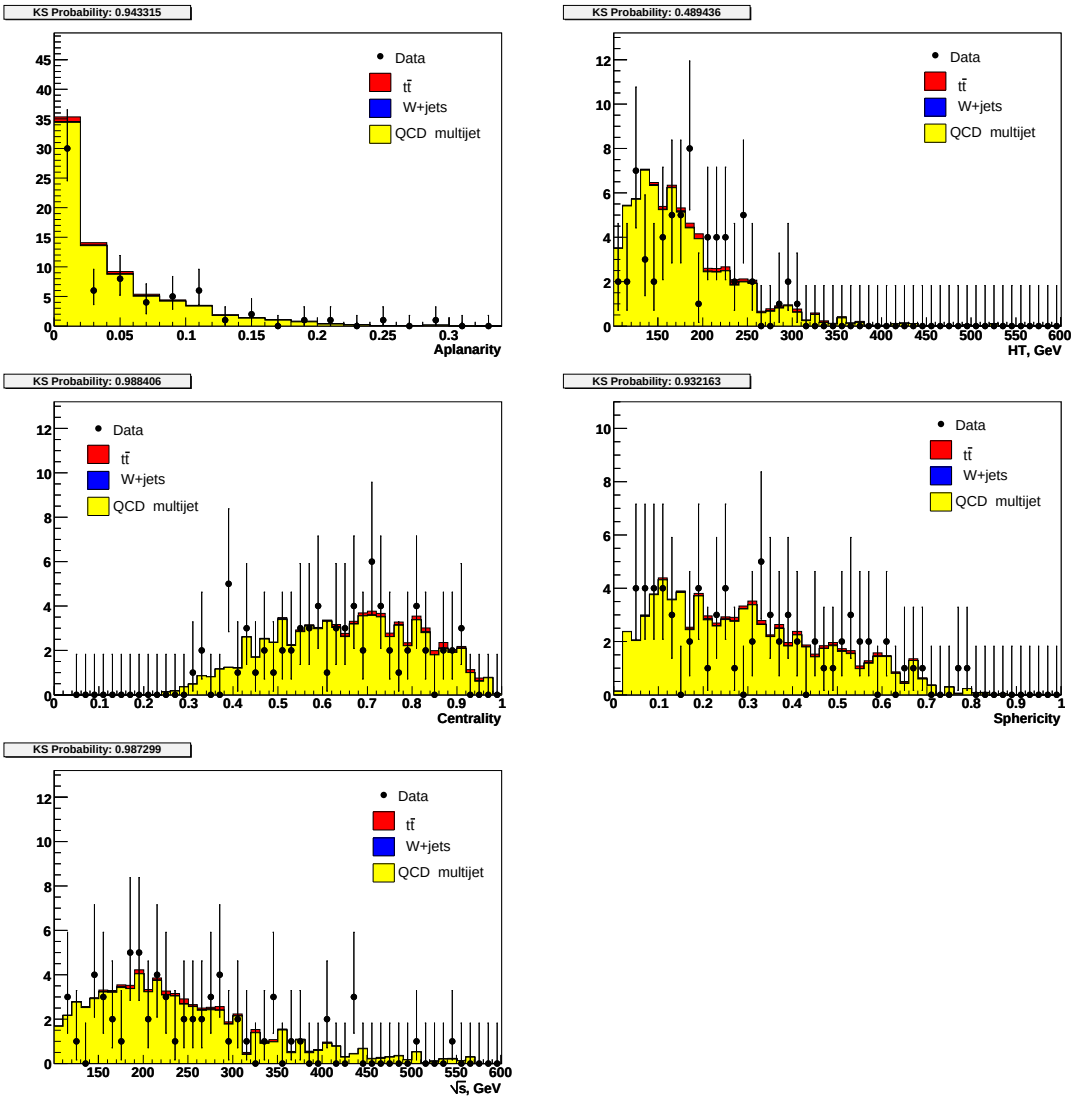

Figure 10.2: The 5 input variables of the first topological NN before the NN cut (τ type 3). The Kolmogorov-Smirnov (KS) probabilities are shown, indicating how good the agreement is.

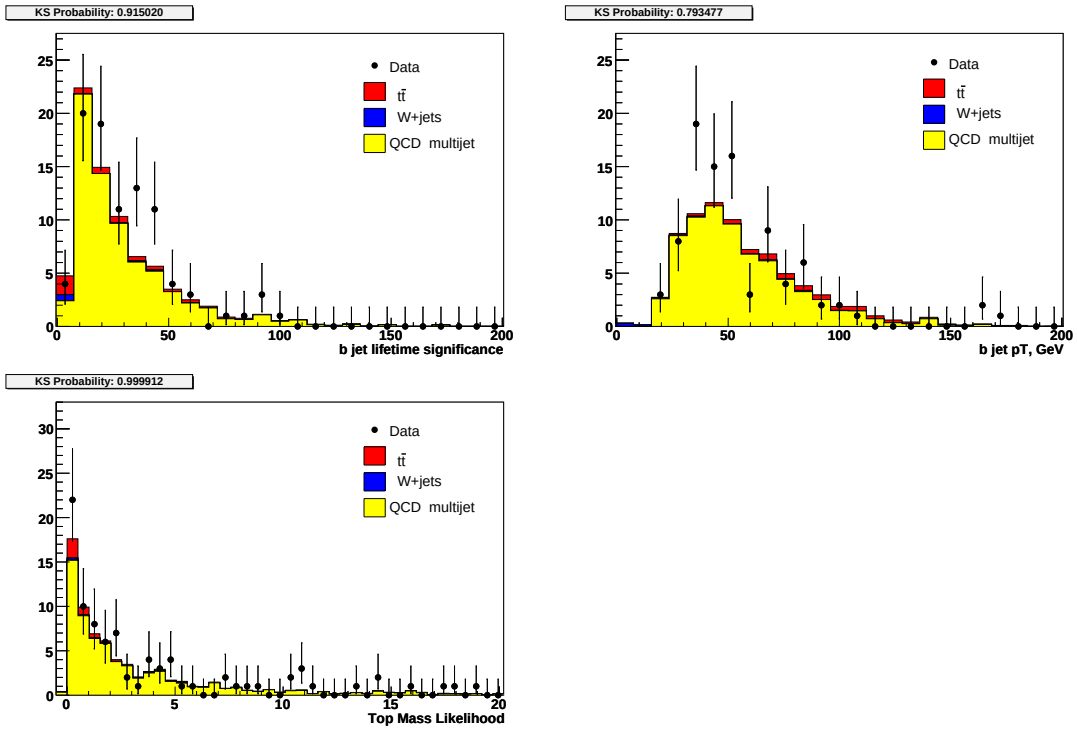

Figure 10.3: The 3 input variables of the second topological NN before the NN cut (τ type 2). The Kolmogorov-Smirnov (KS) probabilities are shown, indicating how good the agreement is.

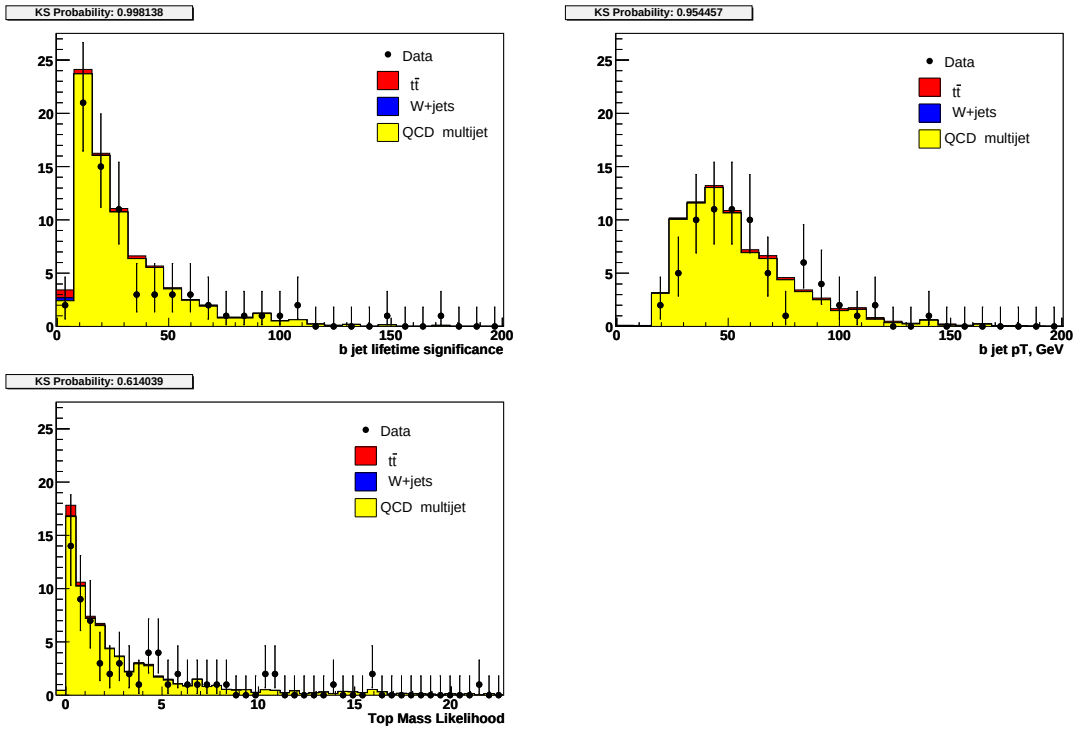

Figure 10.4: The 3 input variables of the second topological NN before the NN cut (τ type 3). The Kolmogorov-Smirnov (KS) probabilities are shown, indicating how good the agreement is.

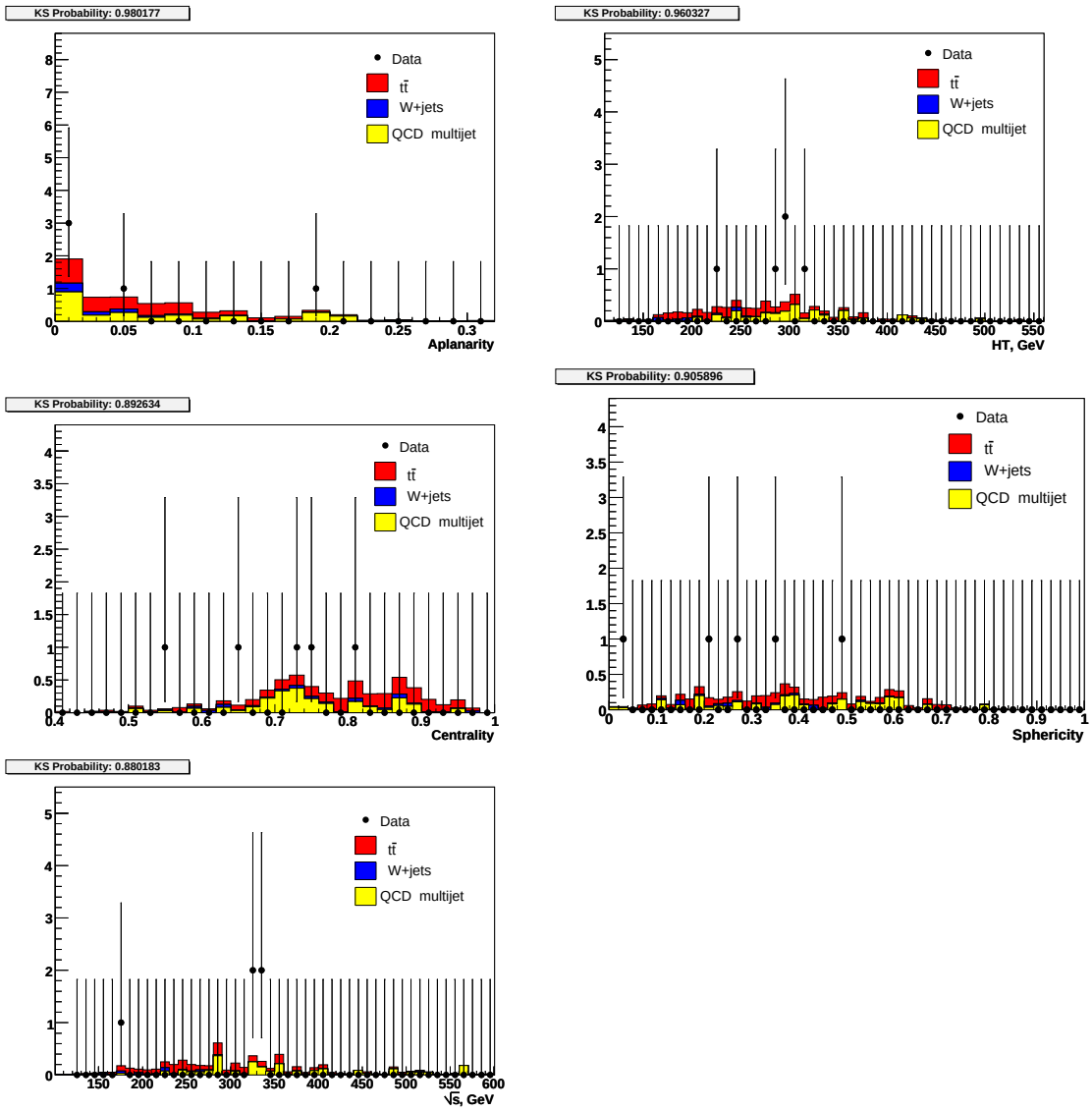

Figure 10.5: The 5 input variables of the first topological NN after the NN cut of 0.9 (τ type 2). The Kolmogorov-Smirnov (KS) probabilities are shown, indicating how good the agreement is.

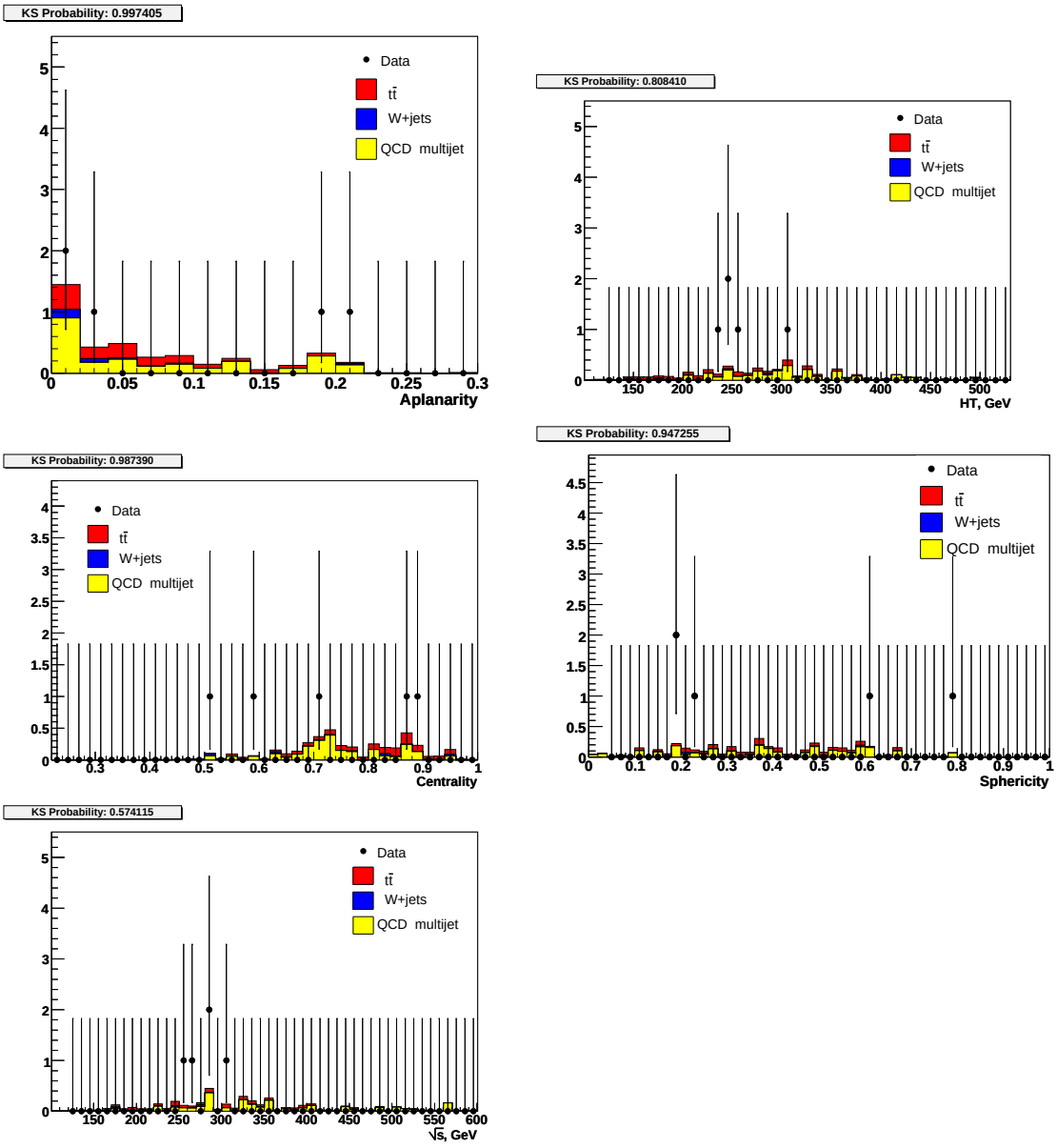

Figure 10.6: The 5 input variables of the first topological NN after the NN cut of 0.9 (τ type 3). The Kolmogorov-Smirnov (KS) probabilities are shown, indicating how good the agreement is.

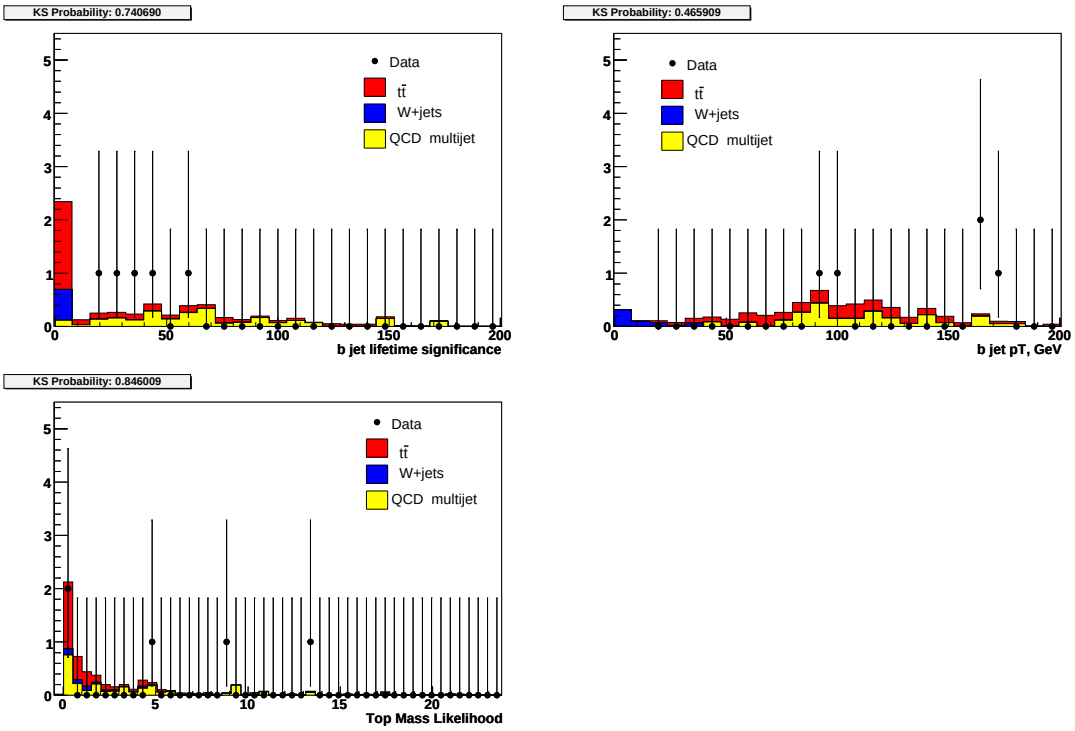

Figure 10.7: The 3 input variables of the second topological NN after the NN cut of 0.9 (τ type 2). The Kolmogorov-Smirnov (KS) probabilities are shown, indicating how good the agreement is.

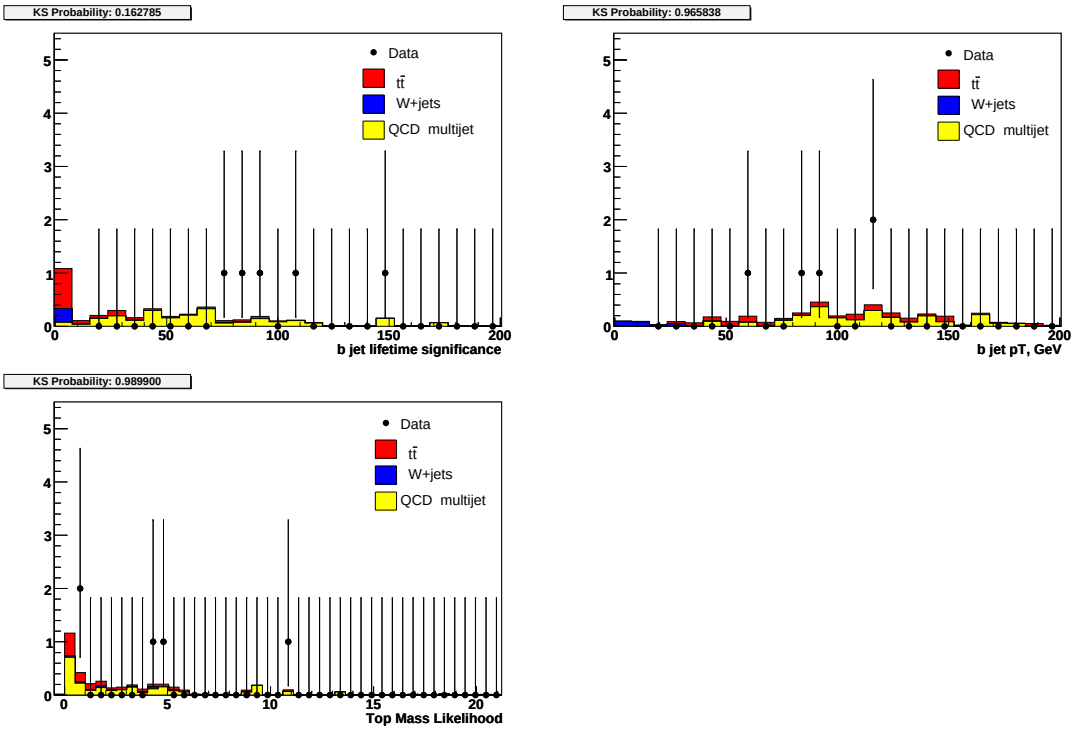

Figure 10.8: The 3 input variables of the second topological NN after the NN cut of 0.9 (τ type 3). The Kolmogorov-Smirnov (KS) probabilities are shown, indicating how good the agreement is.

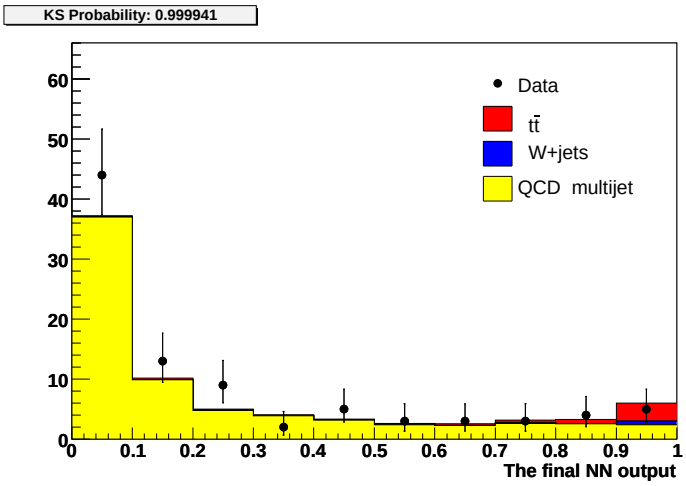

Figure 10.9: The resulting output of the second (final) NN (τ type 2).

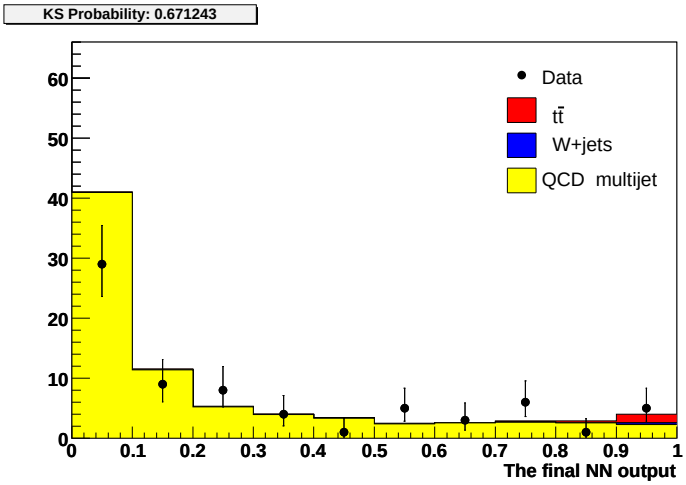

Figure 10.10: The resulting output of the second (final) NN (τ type 3).

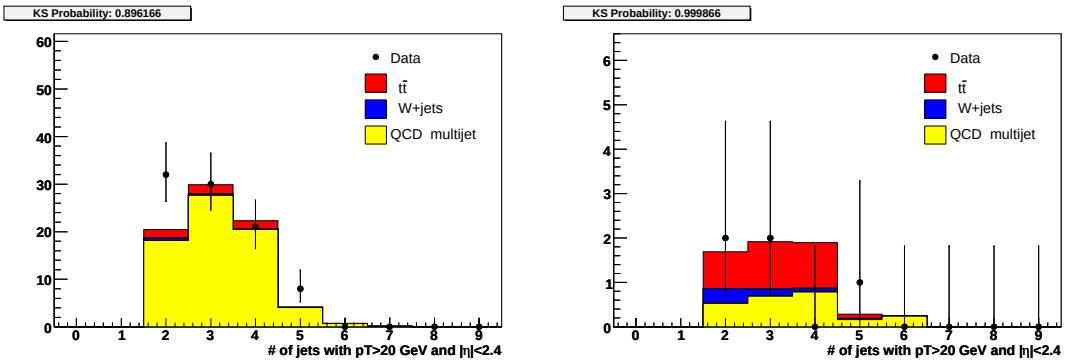

Figure 10.11: Jet multiplicity in the selected events. Left plot is before the NN cut, the right one is after.

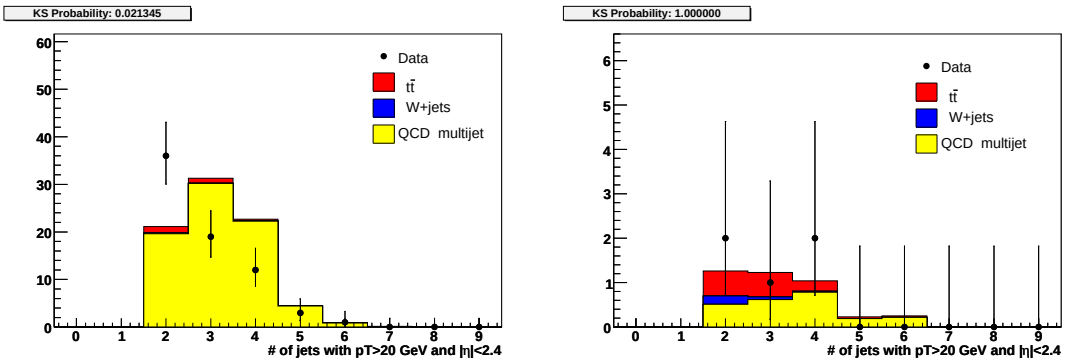

Figure 10.12: Jet multiplicity in the selected events. Left plot is before the NN cut, the right one is after.